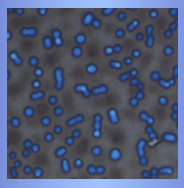

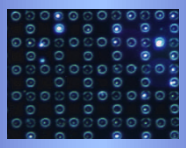

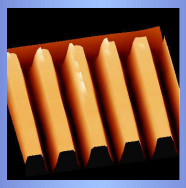

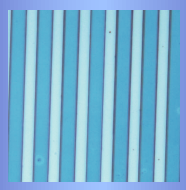

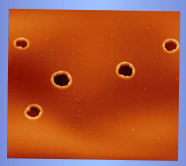

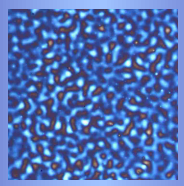

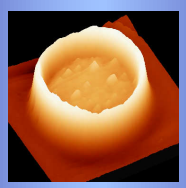

Pattern Formation by Capillary Instabilities in Thin Films

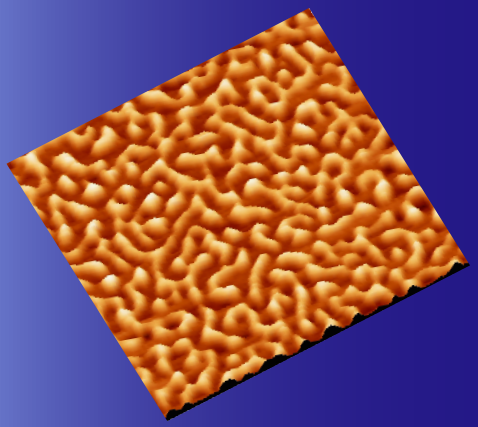

Mihai D. Morariu

Pattern Formation by Capillary Instabilities in Thin Films

Mihai D. Morariu

MSC Ph.D.-thesis series 2004-06
ISSN 1570-1530

"Pattern Formation by Capillary Instabilities in Thin Films"

M. D. Morariu
Ph.D. Thesis
University of Groningen, the Netherlands
9^{th} July, 2004

ISBN: 90–367–2072–9

This research was financially supported by the:
"Dutch Polymer Insitute" (DPI);
"Materials Science Center" (MSC);
"Stichting voor Fundamenteel Onderzoek der Materie" (FOM);

Rijks*universiteit* Groningen

Pattern Formation by Capillary Instabilities in Thin Films

Proefschrift

ter verkrijging van het doctoraat in de
Wiskunde en Natuurwetenschappen
aan de Rijksuniversiteit Groningen
op gezag van de
Rector Magnificus, dr. F. Zwarts
in het openbaar te verdedigen op
maandag 5 July 2004
om 13.15 uur

door

Mihai Dorin Morariu

geboren op 4 Augustus 1973
te Falticeni (Roemenie)

Promotor: Prof. Dr. U. Steiner

Beoordelingscommissie: Prof. Dr. Stefan Herminghaus
Prof. Dr. Thomas P. Russell
Prof. Dr. David Andelman

ISBN: 90–367–2072–9

Never let the future disturb you.
You will meet it, if you have to,
with the same weapons of reason
which today arm you against the present.

Marcus Aurelius Antonius, Meditations, 200 A.D..

To Aurora

Abstract: Polymers, or macromolecules, dominate today's materials industry and play key roles in many areas of science and technology. The behavior of polymers at surfaces and interfaces has proved to be an important factor in understanding wetting issues, because the morphological features of a polymer film on a solid surface depend on the nature of interactions between the polymer and the solid. Ultrathin films are unstable and break spontaneously via a spinodal mechanism or by heterogeneous hole nucleations. In contrast, macroscopic films are stable. With the help of electric fields and temperature gradients, a destabilizing interfacial pressure can be generated at their surface. If the external pressure overcome the stabilizing effect of the surface tension, it drives the film towards dewetting.

The external, either electric or thermic field, can be applied by placing the polymer film between two electrodes in a capacitor geometry, including also an air gap. The developing morphology can be controlled by laterally varying the applied fields with the help of a structured electrode. As a consequence, the instability is driven towards the regions with high field intensity.

However, the interaction of the external fields with the polymer film is undesired when using an electrically active polymeric material. This limitation may be circumvented by making use of film instabilities that are intrinsic to the system. In case of a film made of a polymer blend, its surface can become spontaneously unstable due to surface tension gradients at film–air interface. If confined by a topographically structured surface, the undulatory mode of the film instability is harnessed to induce directionality and functionality to the film.

Polymer blends are also of practical interest as a means of obtaining micro–structured materials. We present a method of obtaining porous materials based on demixing of a polymer blend followed by a subsequent washing of one of the polymers. If the phase morphology has a lateral length scale below 100 nm, the resulting nanoporous films can be used as high performance antireflection coatings.

In conclusion, nanoscale materials and processes have potential applications in many areas such as biological detection, controlled drug delivery, optical devices, sensors, etc. The advancement of new methods to control the pattern formation processes gives us the possibility to develop functional materials that improve the technical inventory of our modern life.

Contents

Chapter 1

Introduction

Thin films are common in everyday life as protective or decorative coatings, ink on a transparent sheet, as a lubricant film on the cornea of our eyes, etc. Their stability plays an important role in a variety of technological processes. Therefore, much experimental and theoretical effort was directed towards understanding the multitude of factors that lead to the rupture of thin films.

If a liquid completely wets a surface, it forms a perfectly homogeneous coating. Also, liquids that do not naturally wet a substrate can be forced to form a continuous, uniform film using different coating techniques, such as spin–coating, dip–coating, etc. However, films produced this way are not generally stable. If allowed to reach their thermodynamic equilibrium by raising the temperature or by annealing in a vapor atmosphere, the films may become unstable and eventually break–up. This rupturing process is usually called "dewetting" and leads to a multitude of patterns, depending on the mechanism involved in the destabilization of the liquid layer.

Due to the immense complexity of the break–up mechanisms, there is no general agreement concerning the physics leading to dewetting and structure formation at interfaces. For polymer films with thicknesses below 10 nm, film instabilities driven by van der Waals forces may occur spontaneously [1, 2, 3].

This destabilization process, which is driven by dispersion forces, is known as spinodal dewetting and has been extensively analyzed both experimentally and theoretically on the basis of the characteristics of the final film morphology.

The understanding of dewetting and the ability to predict the resulting film morphology provides a possibility to control the pattern formation. However, films thicker than 10 nm are stable against van der Waals driven capillary fluctuations. To destabilize thicker films, longer ranged forces have to be used [4, 5]. The application of an external force permits to control the capillary instabilities, because the magnitude of the force can be varied. Based on this principle, several soft lithographic techniques were developed. By suitably coupling surface instabilities to externally applied fields such as electric fields, temperature gradients, etc., the pattern formation process can be controlled on sub–micrometer lateral length scales. This process is of interest especially in the semiconductor industry that requires a continuing decrease in the size of the smallest features of integrated circuits. In this respect, polymers are an ideal material because of their ease of processing and low cost.

Polymer blends are also of practical interest as micro–structured materials. Two different polymers usually don't mix. Repulsive interactions combined with a low entropy of mixing drive polymer blends to demix. The control of the phase separation process of binary mixtures gives the possibility to adjust the resulting phase morphology. Composite materials obtained by the demixing of blends can have enhanced or poorer physical properties that differ from the initial components, such as mechanical stability, optical or electrical properties, etc. These composites are often employed in modern technological applications, such as antireflection coatings, light emitting diodes, solar cells, gas separating membranes, reinforced materials, etc.

This thesis mainly focuses on exploring various causes that lead a liquid polymer film to break–up. Understanding how instabilities develop, we were able to harness some of these mechanisms in lithographic processes to produce structures with sub–100 nm size features. Furthermore, we fine–tuned the demixing process of polymer blends to produce composite coatings that can be used as high–quality antireflection coatings. In the following paragraphs a short introduction of the investigated subjects is given.

Antireflection (AR) Coatings

Optical surfaces coated with a thin layer to improve light transmission are indispensable for virtually all optical systems. Discovered by Fraunhofer in 1817, the coating of lenses or any other optical components to reduce the intensity of light reflection became standard practice in 1930s. The first antireflection coatings ever made were produced by a chemical etch/leach process of a glass surface. During the past decades, various processes were employed to produce different types of AR coatings on glass or plastic substrates. However, in spite of intensive research, broad–band antireflection coatings are still limited by the lack of materials with low refractive indices. New methods of tailoring the refractive index of film materials were developed and proved beneficial for optical coatings, because transparent solid materials with very low refractive indices do not naturally exist. In addition, the control of the refractive index makes it possible to fabricate coatings with optical properties that vary with their thickness.

Three types of AR coatings are distinguished: homogeneous coatings, porous layers and sub–wavelength structured surfaces.

Conventional homogeneous AR coatings consist of a thin layer of dielectric material. The layer properties are tuned such that the light reflected from the outer surface of the film and from the film–substrate interface cancel by destructive interference [6]. Two requirements are needed for an exact cancellation of the reflected beams: the waves reflected from the two interfaces must be out of phase by 180 degrees (π radians), and they must have the same amplitude. If the substrate is white glass with a refractive index of 1.5, the second condition requires a refractive index of the coating of less than 1.3. A typically used material with a low refractive index is MgF_2, with a value of 1.38. However, the performance of a single homogeneous MgF_2 coating is reduced. To further increase the substrate transmission and reduce surface reflection, multiple layer AR coatings were designed.

Another approach to produce AR coatings, is to pattern the substrate with a periodic structure [7] consisting of a dense array of microscopic topographic features (pyramids or columns). The periodicity must be smaller than the shortest wavelength of the incident light in the visible range. The structure introduces a smooth transition between the optical properties of the environment and the substrate, thereby avoiding the abrupt change in the refractive index that give rise to reflection. However, to produce large, defect–free

textured surfaces is not simple. Once produced, the structures are fragile and their wear resistance is reduced in comparison to homogeneous coatings.

A third approach is to use thin porous films as AR coatings. The optical properties of such composite films depend on their porosity, which can usually be tuned by adjusting the processing conditions. If the pore size is much smaller than the wavelength of visible light, the coating refractive index is given by the average of the refractive index of the solid matrix and air. This type of layer has an attractive spectral performance, compared to the optical properties of homogeneous coatings. Porous layers can be produced by electrochemical etching techniques [8, 9], the demixing of blends [10], sol–gel processes [11, 12, 13], etc. By adjusting the processing conditions, the morphology and the porosity of the porous layer can be controlled.

The procedure described in Section 4.3, involves a novel method of producing thin porous films with enhanced mechanical stability. The challenge was to maximize the volume ratio of the pores in order to achieve low enough refractive indices that are needed for a broad–band antireflection coating. The coatings were manufactured using a method based on a sol–gel process that allowed us to produce high–quality antireflection coatings with improved mechanical properties. We developed techniques to deposit these films on glass and plastic substrates.

Capillary Instabilities in Thin Films

The stability of antireflection coatings on glass and plastic substrates is of great technological importance. Therefore, we pursued further experiments to investigate the different causes that affect the wetting behavior of thin polymer films. Industrially, the wetting of coatings is important. The wetting behavior of a film is also relevant for the study of pattern formation processes and various aspects of soft–lithography. To determine the stability of non–wetting films, the opposite phenomenon, dewetting, must be understood. This destabilization process poses a serious limitation for many industrial applications, since it causes the rupture of the initially homogeneous film. Several possible pathways have been proposed and demonstrated for the transition from the initially flat and smooth film to the final state of droplets on a surface.

The first attempts to describe the spreading and stability of a liquid on solid surfaces were made at the beginning of the 19^{th} century by Young (1805) [14, 15], Laplace (1806, 1807) [16], Gibbs (1875–1878) [17] and Plateau (1869)

[18]. They successfully explained a large number of experimental phenomena such as capillary rise, the shape of sessile or pendant drops, etc. using simple thermodynamic and mechanical descriptions. However, in spite of the simplicity of these models, many fundamental processes regarding the stability of thin liquid films on solid substrates are not fully understood [19]. The physicochemical parameters controlling the thermodynamic wettability of a solid surface were studied by Zisman (1964) [20], Fowkes (1964), Padday (1978) [21, 22] and others.

The experimental and theoretical work on film stability was recently resumed, with many authors trying to explain the process of dewetting in thin polymer films [23, 24], liquid metals [25], etc. This renewed interest was not only caused by the technological importance of film stability in the coating industry, lubrication layers, etc., but also because liquid dewetting leads to a rich pattern formation process. Most of the authors focused their attention on the destabilization of polymer films by van der Waals forces [26, 27, 28], the nature of the substrate and the environment [29, 30], the presence of electric charges [31], applied electric fields [4, 32], temperature gradients [33, 34], stresses induced by the substrate [35] or stabilizing capping layers [36], etc. Although the theories describing these phenomena are generally not limited to polymers, polymer films are often used in dewetting studies.

To explain the experimental results of dewetting studies, a theoretical model based on van der Waals forces was often used. However, because of the very small temperature dependence of electromagnetic forces, the effect of temperature on the stability of thin polymer films was usually neglected. van der Waals forces arise from the confinement of the fluctuating electromagnetic spectrum in thin polymer films [37]. Inside the film, fluctuations with wavelengths bigger than twice the film thickness are suppressed. Differences in the density of states outside and inside the film, lead to an imbalance in radiation pressures exerted onto its boundaries. This results in a force that destabilizes the thin polymer film. The same explanation can be applied to any other fluctuating field. Larraza et al. [38] measured the attractive force between two plates in an external sound field. Bschorr [39] calculated the attractive force between two plates in air, based on the confinement of thermal fluctuations. Following a formalism introduced by Dzyaloshinskii [40], Schäffer et al. [41] estimated the interfacial pressure in a thin liquid polymer film arising from the confinement of phonons. In Chapter 5, we present model calculations indi-

cating the route to quantify this force, together with several experiments that demonstrated the presence of the thermo–acoustic pressure.

Harnessing Film Instabilities in Lithographic Processes.

Understanding the causes of dewetting in liquid films opens new routes to improve the stability of such films [42]. However, in some cases the patterns formed by unstable films can be harnessed to produce technologically interesting structures. Because the standard patterning techniques, such as X–Ray, electron or ion beam lithography, and photolithography are either to expensive or with their resolution close to their fundamental limits, new complementary lithographic approaches [43, 44, 45, 46, 47] were developed, and a new field called soft lithography was born. These new emerging techniques include micro–contact printing [48, 49], nanoimprinting [50, 51], microtransfer moulding [52, 53], pattern replication induced by electric fields [4], self–organization [54], self–assembly [63], microcutting [56] and growth on ultraoriented substrates [57]. Several of these techniques uses a soft mould (or stamp) that allow the easy and reliable patterning in the nanometer range.

A somewhat less established approach makes use of surface instabilities in thin polymer films, triggered by electric fields or temperature gradients [5]. An external electric field applied perpendicular to the interface between two liquids confined in a capacitor geometry, gives rise to two effects: (1) the generation of free charges at the interface in the case of finite conductivity of one of the liquids, and (2) the formation of polarization charges [58, 59, 60]. In the experiments performed by Schäffer et al. [4] the first effect is negligible. Using a dielectric film of polystyrene or polymethylmethacrylate sandwiched between two electrodes, the eventual free charges are due to impurities in the polymer layer. However, the effect is very small and the instability is considered as caused purely by polarization charges. The uncompensated polarization charges induced at the dielectric interface by a perpendicular electric field increases the free energy of the system. Therefore, the liquid tends to minimize the amount of surface perpendicular on the electric field by destabilizing its interface.

In thin films, the electrohydrodynamic (EHD) instability is opposed by the surface tension and by the viscous flow in the liquid [61, 62]. Similar to van der Waals forces, the strong destabilizing pressures generated by electric fields amplify the initial capillary waves, leading to the rupture of the film. The

competition of the stabilizing surface tension and the destabilizing pressure selects a wavelength, which is amplified most, thereby generating a surface pattern [63, 64].

By the imposition of a lateral variation in the force field, the intrinsic instability of the system can be controlled. Such inhomogeneous fields are easily realized by using a topographically structured electrode. The instability is drawn towards the electrode protrusions where the electric field is higher, forming a positive replica of the imposed structure. However, these techniques structure a single layer of material. For many applications it is desirable to control the spatial arrangement of more than one component. We have developed a replication process, in which multiple materials are processed simultaneously, as described in Chapter 6. Instead of a single dielectric layer we used a bilayer formed by two different polymers. A sequence of EHD instabilities produced a hierarchic lateral structure. Using a laterally modulated electric field we directed both instabilities into patterns with a lateral size as low as 100 nanometers.

Instabilities in Thin Polymer Blend Films

Both van der Waals driven and EHD instabilities are generated by the amplification of capillary waves by external forces. In some cases, thick polymer films can become spontaneously unstable. The spontaneous destabilization of films poses considerably technological challenges, especially for paint industry, where virtually all manufactured products require stable coatings, both for decorative and protective reasons. Two important effects that cause the flow of material in liquid coatings are convection driven by gravity (Rayleigh–Bénard convection) and thermocapillarity (Marangoni effect). Recently, much experimental and theoretical effort was directed to the understanding of thermocapillarity [65, 66, 67, 68]. Flows driven by temperature gradients arise in several important technological processes and have been subject of considerable research [69, 70, 71]. Industrially, convection phenomena proved to be important important in the dynamics of paint drying [72] or in laser welding [73].

For most liquids, the surface tension is a decreasing function of temperature. Thermocapillary instabilities arise due to the variation of the interfacial temperature along the film interface, leading to nonuniformities in the surface tension, thereby generating an interfacial shear stress [74]. Such stresses set

the liquid into motion. As even hotter liquid reaches the film surface, the fluid flow is accelerated. However, if the liquid layer is sufficiently thin, it is possible to assume that the temperature is virtually constant across the thickness of the layer. In this case, surface tension gradients at the fluid–air interface may be induced by concentration gradients in the bulk and at the surface of the fluid. This phenomenon is for example encountered in polymer blends. Recently, it was shown that lateral concentration gradients in demixed films of polymer blends result in composition dependent surface morphologies [75, 10]. However, experimental results showing the spontaneous destabilization of mixed polymer blends by surface tension gradients are scarce.

In Chapter 7 we demonstrate that a compatible blend of polystyrene (PS) and poly(vinyl methyl ether) (PVME) exhibit a surface tension induced instability when heated to temperatures below the demixing temperature of the blend. We explain the experimental results in terms of the film hydrodynamics in the presence of concentration gradients.

The outline of the thesis

Chapter 2 introduces the thermodynamics of the phase separation in polymer blends, and explains how external factors influence the stability of polymer films. In **Chapter 3**, the experimental details of the sample preparation together with the physical properties of some of the materials used in the experiments are presented. Also, the sample characterization by means of optical microscopy, atomic force microscopy (AFM) and ellipsometry is explained.

In **Chapter 4** a new technique of producing antireflection coatings is described. This chapter also provides some background information about how porous AR coatings work. **Chapter 5** describes the theoretical model and the experimental results of a thermo–acoustic film instability. Experimental results using several polymers and substrates are shown and the results of these experiments are discussed.

The technological application of electrohydrodynamic instabilities is shown in **Chapter 6**. A lithographic method that harnesses this instability is described. This method allowed us to replicate structures down to a lateral size of approximatively 100 nm.

Chapter 7 deals with an instability that occurs spontaneously in films of polymer blends. The lateral perturbation of concentration gradients at the surface induce lateral surface tension variations at the polymer–air interface

that produce stresses at the film surface. The polymer layer reduces its stresses by buckling at a well defined wavelength. This wavelength was investigated in terms of the blend composition and film thickness.

Finally, **Chapter 8** summarizes the experimental results and theoretical predictions. The concluding chapter outlines the importance of the present work and highlights open and unanswered questions.

Bibliography

[1] A. Vrij; *Discuss. Faraday Soc.* **42**, 1966

[2] A. Scheludko; *Adv. Colloid Interface Sci.* **1**, 1967

[3] E. Ruckenstein, R.K. Jain; *J. Chem. Soc. Faraday Trans.II* **70**, 1974

[4] E. Schäffer, T. Thurn–Albrecht, T.P. Russell, U. Steiner; *Nature* **403**, 2000

[5] E. Schäffer, S. Harkema, M. Roerdink, R. Blossey, U. Steiner; *Adv. Mater.* **15**, 2003

[6] O.S. Heavens; *Optical Properties of Thin Solid Films* Dover Publications Inc., New York 1991.

[7] V. Boerner, B. Bläsi, A. Gombert, A. Heinzel, V. Kübler, P. Popp, V. Wittwer, *Large Area Surface-Relief Microstructures for Optical Applications*, Proceedings Micro Materials Conference *MicroMat 2000*, Berlin, 17–19.04.2000

[8] V. Lehmann, U. Gösele; *Appl. Phys. Lett.* **58**, 1991.

[9] L.T. Canham; *Appl. Phys. Lett.* **57**, 1990.

[10] S. Walheim, E. Schäffer, J. Mlynek, U. Steiner; *Science* **283**, 1999.

[11] N. Hüsing, U. Schubert; *Angew. Chem. Int. Ed.* **37**, 1998.

[12] G. Pajonk, E. Elaloui, P. Achard, B. Chevalier, J.L. Chevalier, M. Durant; *J. Non–Cryst. Sol.* **186**, 1995.

[13] B.E. Yoldas, T.W. O'Keeffe; *Appl. Opt.* **18**, 1979.

[14] T. Young; *Miscellaneous Works*; I. J. Murray, London, 1855

[15] T. Young; *Phys. Trans. Roy. Soc.* **95**, 1805

[16] P.S. Laplace; *Suppléement à la théorie de l'action capillaire /de Laplace.* Paris, 1807

[17] J.W. Gibbs; *Trans. Conn. Acad.* **3**, 1878.

[18] J. Plateau; *Statique expérimentale et théorique des liquides*, Gauthier-Villars et Cie. 1873.

[19] L. Leger, J.F. Joanny; *Rep. Prog. Phys.* 431–486, 1992

[20] W.A. Zisman, *Advan. Chem. Ser.* **43**, 1964.

[21] F.M. Fowkes; *Advances in Chemistry*, Amer. Chem. Soc., Washington, D.C., 1964

[22] J.F. Padday, *Wetting, Spreading and Adhesion* Academic Press, New York, 1978.

[23] C. Redon, F. Brochard-Wyart, F. Rondelez; *Phys. Rev. Lett.* **66**, 1991; G. Reiter, *Phys. Rev. Lett.* **68**, 1992; A. Sharma, G. Reiter, *J. Colloid Interf. Sci.* **178**, 1996; K. Jacobs, S. Herminghaus, K.R. Mecke, *Langmuir* **17** 1998; U. Thiele, M. Mertig, W. Pompe, *Phys. Rev. Lett.* **80**, 1998; G. Reiter, *Phys. Rev. Lett.* **87**, 2001

[24] R. Xie, A. Karim, J.F. Douglas, C.C. Han, R.A. Weiss, *Phys. Rev. Lett.* **81**, 1998; A. Sharma, R. Khanna, *Phys. Rev. Lett.* **81**, 1998; G. Reiter, R. Khanna, A. Sharma, *Phys. Rev. Lett.* **85**, 2000; L.M. Pismen, Y. Pomeau, *Phys. Rev. E* **62**, 2000; R. Khanna, A. Sharma, G. Reiter, *EPJdirect E* **2**, 2000; U. Thiele, M.G. Velarde, K. Neuffer, *Phys. Rev. Lett.* **87**, 2001; U. Thiele, M.G. Velarde, K. Neuffer, Y. Pomeau, *Phys. Rev. E* **64**, 2001; K.D.F. Wensink, B. Jerome, *Langmuir* **18**, 2002; A. Sharma, J. Mittal, *Phys. Rev. Lett.*, **89**, 2002; A. Sharma, J. Mittal, R. Verma, *Langmuir* **18**, 2002

[25] J. Bischof, D. Scherer, S. Herminghaus, P. Leiderer; *Phys. Rev. Lett.* **77**, 1996

[26] F. Brochard–Wyart, J. Daillant; *Can. J. Phys.* **68**, 1990

[27] G. Reiter; *Phys. Rev. Lett.***68**, 1992

[28] R. Seemann, S. Herminghaus, K. Jacobs; *J. Phys.: Condens. Matter.* **13**, 2001

[29] G. Reiter, A. Sharma, R. Khanna, A. Casoli, M.-O. David; *J. Colloid Interface Sci.* **214**, 1999

[30] G. Reiter, A. Sharma, A. Casoli, M.-O. David, R. Khanna, P. Auroi; *Langmuir* **15**, 1999; G. Reiter, R. Khanna, A. Sharma; *Phys. Rev. Lett.* **85**, 2000

[31] S. Herminghaus; *Phys. Rev. Lett.* **83**, 1999

[32] E. Schäffer, T. Thurn–Albrecht, T.P. Russell, U. Steiner; *Europhys. Lett.* **53**, 2002

[33] E. Schäffer, S. Harkema, R. Blossey, U. Steiner; *Europhys. Lett* **60**, 2002

[34] E. Schäffer, S. Harkema, R. Blossey, U. Steiner; *Macromolecules* **36**, 2003

[35] K.Y. Suh, H.H. Lee; *Phys. Rev. Lett.* **87**, 2001

[36] K. Dalnoki-Veress, B.G. Nickel, J.R. Dutcher; *Phys. Rev. Lett.* **82**, 1999

[37] H.B.G. Casimir; *Proc. Kon. Ned. Akad. Wetensch.* **51**, 1948

[38] A. Larraza, C.D. Holmes, R.T. Susbilla, B. Denardo;*J. Acoust. Soc. Am.* **103(5)**, 1998

[39] O. Bschorr; *J. Acoust. Soc. Am.* **106(6)**, 1999

[40] I.E. Dzyaloshinskii, E.M. Lifshitz, L.P. Piaevskii; *Adv. Phys.* **10** 1961

[41] E. Schäffer, U. Steiner; *Eur. Phys. J. E* **8**, 2002

[42] R. Yerushalmi-Rosen, J. Klein, L. Fetters; *Science* **263** 1994.

[43] J.P. Spatz, P. Eibeck, S. Mößmer, M. Möller, T. Herzog, P. Zieman; *Adv. Mater.* **10**, 1998

[44] P.G. Collins, A. Zettl, H. Brando, A. Thess, R.E. Smalley; *Science* **8**, 1997

[45] D.H. Pearson, R.J. Tonucci; *Adv. Mater.* **8**, 1996

[46] C.A. Mirkin, R.L. Letsinger, R.C. Mucic, J.J. Storhoff; *Nature* **382**, 1996

[47] J.P. Spatz, S. Mößmer, M. Möller; *Chem. Eur. J.* **2**, 1996

[48] A. Kumar, G.M. Whitesides; *Appl. Phys. Lett.* **63**, 1993

[49] H. Li, D.J. Kang, M.G. Blamire, W.T.S. Huck; *NanoLett.* **2**, 2002

[50] J. Wang, X. Sun, L. Chen, S. Chou; *Appl. Phys. Lett.* **75**, 1999

[51] C.C. Cedeño, J. Seekamp, A.P. Kam, T. Hoffmann, J. Ahopelto; *J. Microelectron. Eng.* **61–62**, 2002

[52] X.M. Zhao, Y. Xia, G.M. Whitesides; *Adv. Mater.* **8**, 837

[53] M. Cavallini, M. Murgia, F. Biscarini; *NanoLett.* **1**, 2001

[54] M. Cavallini, F. Biscarini, A. Farran–Morales, M. Massi, D.A. Leigh, F. Zerbetto; *NanoLett.* **2**, 2002

[55] S.Y. Chou, L. Zhuang; *J. Vac. Sci. Technol. B* **17**, 1999

[56] N. Stutzmann, T. Tervoort, D.J. Broer, H. Sirringhaus, R.H. Friend, P. Smith; *Adv. Func. Mater.* **12**, 2002

[57] J.F. Moulin, M. Brinkmann, A. Thierry, J.C. Whitmann; *Adv. Mater.* **14**, 2002

[58] J.W. Swan; *Proc. Roy. Soc.* **62**, 1897

[59] L. Tonks; *Phys. Rev.* **48**, 1935

[60] J. Frenkel; *Phys. Z. Sowjetunion* **8**, 1935

[61] G. N. de Surgy, J.P. Chabrerie, O. Denoux, J.E. Wesfreid; *J. Phys. II France* **3**, 1993

[62] W.E. Glen; *J. Appl. Phys.* **30**, 1959

[63] S. Chou, L. Zhuang, L. Guo; *Appl. Phys. Lett.* **75** 1999.

[64] S. Chou, L. Zhuang; *J. Vac. Technol. B* **17** 1999.

[65] H. Bénard; *Rev. Gen. Sci. Pure Appl.* **11** 1900.

[66] S. Chandraseckhar; *Hydrodynamic and Hydromagnetic Stability*, Oxford, Clarendon, 1961

[67] P.G. Drazin, W.H. Reid; *Hydrodynamic Stability* Cambridge, Cambridge Univ. Press 1981

[68] G. Lebon, C. Perez–Garcia; *Bull. Classe Sci. Acad. R. Belg.* **64** 1980.

[69] S.H. Davis; *Annu. Rev. Fluid Mech.* **19** 1987.

[70] A. Thess, S.A. Orszag; *J. Fluid Mech.* **283** 1995.

[71] A.M. Mancho, H. Herrero; *Phys. of Fluids* **12** 2000.

[72] S.B.G.M. O'Brien; *J. Fluid Mech.* **254** 1993.

[73] N. Postacioglu, P. Kapadia, J. Dowen; *J. Phys. D: Apll. Phys.* **24** 1991.

[74] A. Oron; *Phys. of Fluids* **12** 2000.

[75] B.D. Ermi, A. Karim, J.F. Douglas; *J. Polym. Sci. Polym. Phys. Ed.* **36** 1998.

Chapter 2

Theoretical Background

2.1 Fundamental Notions of Polymer Physics

Unmatched in the diversity of their properties, polymers such as cotton, wool, rubber, Teflon®, and other plastics are used in nearly every industry. Natural and synthetic polymers can be produced with a wide range of stiffness, strength, heat resistance, density, and also price.

A polymer is a chain molecule that is made up of many small, chemical repeating units [1]. The total number of structural units (or monomeric units) N, represents the *degree of polymerization*. These macromolecules are generally obtained by a polymerization process starting from reactive low molar mass compounds. Rather than leading to polymers with a unique N, the chemical polymerization reactions result in a mixture of macromolecules with various molecular weights [2]. Therefore, for a full characterization of a polymeric sample, the *molecular weight distribution function* has to be determined.

Polymer architectures can vary [3, 4, 5]. A *linear* polymer consists of a long chain of monomers. A *branched* polymer has branches covalently attached to the main chain. *Cross–linked* polymers have monomers of one chain covalently bonded with monomers of another chain. Cross–linking results in

a three–dimensional network, that is, the whole polymer sample is one giant macromolecule. We distinguish two situations: loosely cross-linked networks, also known as elastomers, and thermosets, which are densely cross-linked networks.

One classification of polymers is based on the chemical type of the monomers: *Homopolymers* consist of monomers of the same type, while *copolymers* have different repeating units. Furthermore, depending on the arrangement of the different types of monomers, there are *random* copolymers with repeating units that are distributed randomly, *alternating* copolymers which are made of alternating sequences of different monomers, *block* copolymers with a long sequences of a monomer that is followed by a long sequences of the other monomer and *graft* copolymers which are chains made from one type of monomer with branches of another type.

Many properties of polymeric materials depend on the microscopic arrangement of their molecules. Polymers can have an *amorphous* or *semicrystalline* (partially crystalline) structure. Amorphous polymers lack order and are arranged in a random manner, while semicrystalline polymers are partially organized in ordered crystalline structures.

The polymers used in this study are common technical polymers which are known from every day life, such as polystyrene (PS) or poly(methyl methacrylate) (PMMA) which is also known as Plexiglass®. These so called *polymer standards* feature a narrow molecular weight distribution, but they are far from *monodisperse*. The usual polydispersity lies between 1.02 and 1.3.

Either in solution or in the solid state, a polymer chain is not completely stretched out [5, 6]. The bonds connecting the repeating units are generally flexible enough to permit a degree of rotational freedom around the bonds. This freedom of rotation allows the molecule to assume a number of *conformations*. The term "conformation" describes the physical outline of the molecule as opposed to "configuration", which describes the internal structure of a chain. Therefore, a molecule can have many possible spatial conformations. The limits are the completely stretched chain and the random coil. The first conformation is the most improbable one, corresponding to the lowest entropy of the chain. The entropy increase results from the large number of possible conformations. The most probable conformation is that of a Gaussian coil.

The large size of these molecules affects their rheological behavior, which

influences the processability of the polymeric material. Therefore, most properties of polymers depend on their molecular weight. A polymeric sample can be described by two numbers:

- The number average molecular weight $\bar{M}_n$

$$\bar{M}_n = \frac{w}{\sum_{i=1}^{\infty} N_i} = \frac{\sum_{i=1}^{\infty} M_i N_i}{\sum_{i=1}^{\infty} N_i}$$

  which is the total weight of the material divided by the number of molecules in the material.

- The weight average molecular weight $\bar{M}_w$

$$\bar{M}_w = \frac{\sum_{i=1}^{\infty} w_i M_i}{w} = \frac{\sum_{i=1}^{\infty} N_i M_i^2}{\sum_{i=1}^{\infty} M_i N_i}$$

Another important measure of the spatial extent of the molecule is its *radius of gyration* (the average distance of the monomers from the center of mass of the molecule) $R_{\mathrm{g}} = \sqrt{CL^2N}$ where C is an empiric constant and L is an effective binding distance (usually $\sim 5\,\mathring{A}$). An important aspect is the $\sqrt{N}$ dependence of the radius of gyration. For most of the polymers used in this work ($M_w \sim 2.000\,\mathrm{g/mol}$, $N \sim 25$ and $M_w \sim 100.000\,\mathrm{g/mol}$, $N \sim 2500$), the radius of gyration varies between $\sim 0.6\,\mathrm{nm}$ and $\sim 8\,\mathrm{nm}$.

Two further important parameters that define a polymer sample are the *melting temperature* T_{m} and the *glass transition temperature* T_{g}. The melting temperature is characteristic only for those polymers that can crystalize and defines the transition from the liquid to crystalline phase. It is a first order phase transition characterized by discontinuities in the heat capacity and specific volume.

On the other hand, polymers with random stereochemistry (atactic polymers) posses some intrinsic disorder that prevents crystallization. For this type of polymers T_{m} can not be defined. However, these materials upon cooling form an amorphous phase, similar to a glass. The temperature that defines this transition is called the glass transition temperature of the polymer T_{g}. At very low temperatures, no chains or parts of the molecule can move: the polymer is frozen into a rigid glassy state. On heating above T_{g}, the polymer

undergoes a glass to rubber transition. The elastic modulus drops by several orders of magnitude because blocks or segments of the chains become free to move. Nevertheless, segmental motion is possible also below T_g. Even though experimentally T_g is similar to a second phase order transition, it is not a true phase transition. One cannot assign only one value to T_g, because it strongly depends on the experimental conditions (cooling rate, thermal history of the sample, etc.) at which the glass transition is measured.

2.2 Phase Separation of Polymer Blends.

In the case of a polymer blend consisting of chains of type A and B, the main characteristic of the mixture is the thermodynamic compatibility or incompatibility of the components. Compatibility depends, however, on many factors, of which the most important are the temperature **T** and composition φ. Heating or cooling the sample shifts the blend from the mixed state to a completely demixed one. Therefore, we can define a critical temperature and a critical composition that define the boundary between the mixed state and the demixed state. The *phase diagram* is a representation of the critical volume fraction of one component (for example φ_A) as a function of T. Two polymers are usually incompatible. Therefore, they don't mix. Depending on the chemical constitution of the components, the window of miscibility may be very broad, or in contrary, very narrow.

The aim of many experimental investigations on the thermodynamic properties of binary blends, is to determine their miscibility as a function of the chemical structure of the polymers, their molecular mass, temperature and blend composition. To estimate the thermodynamic compatibility of two polymers it is necessary to study the entire concentration range. Whether the system remains homogeneous or separates into two phases can be predicted from the Gibbs free energy of mixing. Flory and Huggins [2] developed a general theory that provides a basic understanding of the occurrence of different types of phases as a function of temperature and molecular weights. Their *mean–field theory* mainly concerned with the positional or combinatorial entropy of mixing of the blend components, proven to be very useful in describing the coexistence curve of a blend.

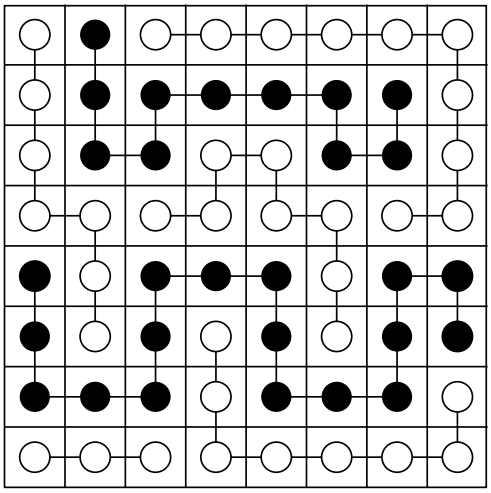

Figure 2.1: Two dimensional lattice model of a mixture of polymer chains. Units of equal size corresponding to monomers of the two polymers occupy the lattice sites.

2.2.1 Flory–Huggins Theory.

This model, developed independently by Flory and Huggins [2, 7, 8, 9], assumes a mixture of n_{A} polymer chains of type A, each consisting of N_{A} segments and n_{B} polymer chains of type B with N_{B} segments. Each of the N_i segments of identical size v, occupy only one site on a lattice consisting of a total number of N sites. This simple situation is depicted in Fig.(2.1). The Flory–Huggins theory considers the change in the so–called "Gibbs free energy of mixing" given by:

$$\Delta\mathcal{G}_{\mathrm{mix}} = \mathcal{G}_{\mathrm{A+B}} - (\mathcal{G}_{\mathrm{A}} + \mathcal{G}_{\mathrm{B}}) \tag{2.1}$$

where $\mathcal{G}_{\mathrm{A+B}}, \mathcal{G}_{\mathrm{A}}$ and $\mathcal{G}_{\mathrm{B}}$ denote the Gibbs free energies for the mixture (A+B) and for the free compounds A and B, respectively. From the first and second law of thermodynamics an alternative expression for $\Delta\mathcal{G}_{mix}$ is derived:

$$\Delta\mathcal{G}_{\mathrm{mix}} = \Delta\mathcal{H} - T \cdot \Delta\mathcal{S} \tag{2.2}$$

where $\Delta\mathcal{H}$ and $T \cdot \Delta\mathcal{S}$ are the enthalpic and entropic contributions to the Gibbs free energy, respectively.

The second term in Eqn.(2.2) represents the increase in the translational entropy associated with the motion of the center of mass of all the molecules. In the pure state, the configurational space available to the center of mass of a molecule of type i is V_i and the associated entropy for its translational degrees of freedom is $k_\mathrm{B} \ln V_i$. In the mixture, a larger volume V is accessible to mixed chains compared to $V/2$ for the chains in the phase separated phase (Fig. 2.2c). The associated entropy increase is $k_\mathrm{B} \ln(V_i/V) = k_\mathrm{B} \ln \varphi_i$, where φ_i is the volume fraction of component i. Specifically, for the two components A and B, φ_A and φ_B are given by:

$$\varphi_\mathrm{A} = \frac{V_\mathrm{A}}{V} = \frac{n_\mathrm{A}}{n_\mathrm{A} + n_\mathrm{B}} \qquad \text{and} \qquad \varphi_\mathrm{B} = \frac{V_\mathrm{B}}{V} = \frac{n_\mathrm{B}}{n_\mathrm{A} + n_\mathrm{B}}$$

where $V_\mathrm{A} = n_\mathrm{A} \cdot v$ and $V_\mathrm{B} = n_\mathrm{B} \cdot v$.

Considering the total number of conformations available for the system:

$$\Omega = \frac{(n_\mathrm{A} + n_\mathrm{B})!}{n_\mathrm{A}! \cdot n_\mathrm{B}!} \tag{2.3}$$

the change in the entropy of mixing is computed using the Boltzmann relation $S = k_\mathrm{B} \ln \Omega$:

$$\frac{\Delta \mathcal{S}}{n k_\mathrm{B}} = -\frac{\varphi_\mathrm{A}}{N_\mathrm{A}} \ln \varphi_\mathrm{A} + \frac{\varphi_\mathrm{B}}{N_\mathrm{B}} \ln \varphi_\mathrm{B} \tag{2.4}$$

The factor $1/N_i$ shows the strong influence of the length of the macromolecules on the mixing behavior of a polymer blend. With increasing molecular mass of the components, the miscibility of the two polymers decreases. Therefore, small molecules are better miscible than polymers.

On the other hand, the first term in Eqn.(2.2) can favor or inhibit the mixing depending on the monomer–monomer pair interaction. Flory and Huggins assumed that this energy stems from purely enthalpic nearest–neighbor interactions. Because the reference chain is in contact with a large number of other chains, the interactions are effectively integrated over the different monomer–monomer interactions. Therefore, the chain can be considered in a mean–field created by the surrounding polymers chains. For simple van der Waals interactions, the attraction between equal monomers is stronger compared to unlike pairs. This selectivity implies that $\Delta \mathcal{H} > 0$ opposes mixing. The change in enthalpy is given by:

$$\Delta \mathcal{H} = n k_\mathrm{B} T \chi \varphi_\mathrm{A} \varphi_\mathrm{B} \tag{2.5}$$

where $n = n_{\mathrm{A}} + n_{\mathrm{B}}$ is the total number of monomers. χ is the so–called interaction parameter or 'Flory–Hugins parameter'. It determines in an empirical manner the change in the local free energy per reference unit. It is dimensionless and is the decisive factor that determines whether the blend stays in the mixed state or it phase separates.

Using Eqn.(2.5) and Eqn.(2.4) together with the expression of the Gibbs free energy of mixing Eqn.(2.2) the so–called Flory–Huggins relation for polymer mixtures and solutions is obtained:

$$\Delta\mathcal{G}_{\mathrm{mix}}\Big|_{\mathrm{site}} = -nk_{\mathrm{B}}T\left\{\frac{\varphi_{\mathrm{A}}}{N_{\mathrm{A}}}\ln\varphi_{\mathrm{A}} + \frac{\varphi_{\mathrm{B}}}{N_{\mathrm{B}}}\ln\varphi_{\mathrm{B}} + \chi(\varphi_{\mathrm{A}},\varphi_{\mathrm{B}},T)\varphi_{\mathrm{A}}\varphi_{\mathrm{B}}\right\} \qquad (2.6)$$

This equation can be used to interpret the bimodal shape of spinodal[1] and cloud point curves[2] (CPC) of polymer mixtures and to theoretically predict the *coexistence curve* of a binary mixture. This curve is a temperature vs. composition diagram given by the locus of points that separate the two phase region from the one phase region. Therefore, it defines the equilibrium composition of the coexisting phases. The points on the coexistence curve where the two phases become identical are the *critical points*, while the temperature at which the phase boundary between the two phases disappears it is called *the critical temperature*. In a binary mixture this temperature defines the extremum of the coexistence curve. If the extremum is a maximum it is called the *upper critical solution temperature* (UCST) and if is a minimum it is called the *lower critical solution temperature* (LCST).

In a multi–phase system, the condition of equilibrium (i.e. the condition that minimizes the free energy of the system) requires that the chemical potential[3] of component i must be the same in all phases. The locus of the points that satisfy this condition gives the coexistence curve, graphically represented in Fig.(2.2b).

On the basis of the equilibrium criteria, stability limits and criticality, the

[1]The spinodal curve defines the limit of metastability. For a polymer blend is the locus of points where the second composition derivative $\partial_{\varphi\varphi}\Delta\mathcal{G}_{mix}$ of the free energy vanishes.

[2]Cloud Point measurements are performed by passing a single beam of monochromatic light from a fiber optic light source through the sample, measuring the amount of light reaching the detector and calculating the change in scattering intensity from a baseline measurement as the sample is cooled [10].

[3]The chemical potential μ_i is defined as $\Delta\mu_i = (\partial\Delta\mathcal{G}_{\mathrm{mix}}/\partial n_i)_{\mathrm{T,n}}$

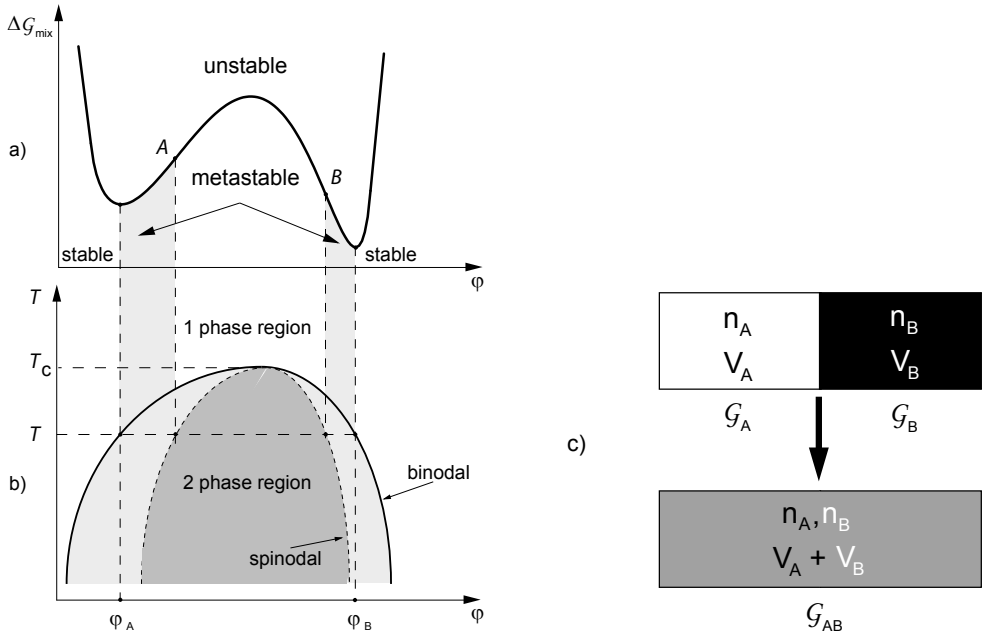

Figure 2.2: a) Dependence of the Gibbs free energy of mixing $\Delta\mathcal{G}_{\mathrm{mix}}$ on the composition φ at constant temperature. At the two inflection points (A and B) in the graph, the second derivative $\partial_{\varphi\varphi}\Delta\mathcal{G}_{\mathrm{mix}}$ vanishes. The inflection points define the spinodal. b) The two phase region is enclosed by the binodal. In the region under the spinodal the mixture is unstable while between the curves the blend is metastable (heterogeneous nucleation and growth of phase separated domains). Above the critical temperature T_c the blend is stable in the mixed phase. A temperature quench from the one–phase to the two–phase region induces phase separation. c) Variables used in the description of the mixing process of two polymers A and B.

coexistence curve (binodal), spinodal line and critical point can be predicted using Eqn.(2.6).

- binodal:

$$\frac{\Delta\mathcal{G}_{\mathrm{mix}}(\varphi_{\mathrm{A}}) - \Delta\mathcal{G}_{\mathrm{mix}}(\varphi_{\mathrm{B}})}{\varphi_{\mathrm{A}} - \varphi_{\mathrm{B}}} = \left.\frac{\partial\Delta\mathcal{G}_{\mathrm{mix}}}{\partial\varphi}\right|_{\varphi_{\mathrm{A}}} = \left.\frac{\partial\Delta\mathcal{G}_{\mathrm{mix}}}{\partial\varphi}\right|_{\varphi_{\mathrm{B}}} \tag{2.7}$$

- spinodal:

$$\frac{\partial^2 \Delta \mathcal{G}_{\text{mix}}}{\partial \varphi^2} = 0 \tag{2.8}$$

- critical point:

$$\frac{\partial^3 \Delta \mathcal{G}_{\text{mix}}}{\partial \varphi^3} = 0$$

For a given temperature the double tangent construction expressed by the binodal equation in Eqn.(2.8) gives the volume fractions φ_{A} and φ_{B} of the two coexistent phases (Fig. 2.2b). The homogeneous mixture is stable outside the coexistence curve, metastable between binodal and spinodal lines (the nucleation and growth region) and unstable inside the spinodal line.

2.3 Stability of Thin Homogeneous Polymer Films

Considerable experimental and the theoretical effort was dedicated to understand the stability of thin polymer films supported by solid substrates. These topics were addressed by several authors [11] who tried to explain the different rupture mechanisms, as well as the large number of factors that influence these processes. A strong motivation for this type of experiment was the large number of different patterns that are generated by the break–up mechanism. Therefore, it is first necessary to understand the processes governing the dynamics of a thin film at a fundamental level.

Thin polymer films have proven to be ideal model systems in these studies due to their low vapor pressure and to their high viscosity that facilitates the study of their dynamic behavior. The generic experimental system is depicted in Fig.(2.3).

A thin polymer film is deposited onto a substrate and liquified by heating above its glass transition temperature T_g. The molecular motion of the liquid at finite temperatures causes a spectrum of capillary waves at the liquid surface. Capillary waves are perturbations of the free interface and generate flow in the film which can be described using a hydrodynamic approach. The theoretical model involves the Navier–Stokes equation, which balances the macroscopic forces at the interface. If an external force is coupled to the free interface, it can dampen or amplify the initial capillary fluctuations. The

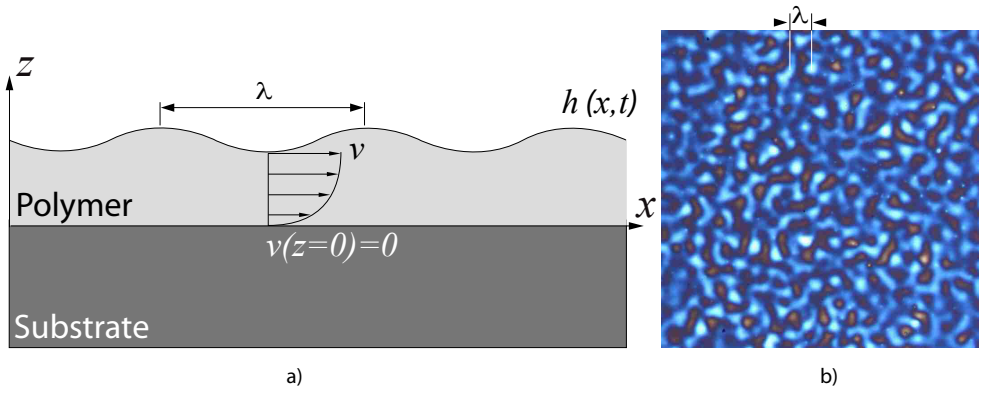

Figure 2.3: a) *The generic experiment used to study the influence of external factors on the stability of thin liquid polymer films. The polymer layer was deposited onto a solid substrate and liquified by heating. The wavelength of the instability was measured and plotted vs. the film thickness.* b) *Optical micrograph (30×30 μm^2) showing surface undulations of a 100 nm thick polystyrene film with a characteristic wavelength λ*

basic strategy in computing the evolution of the capillary waves is to model the free interface with a sinusoidal function

$$h(x,t) = h_0 + \zeta \exp(iqx + t/\tau) \tag{2.9}$$

The amplitude ζ is considered to be much smaller than the initial film thickness h_0 ($\zeta \ll h_0$). The aim is to determine the *dispersion relation* characteristic to the liquid film, relating the time constant τ to the wave vector q of each wave mode and to establish whether a fluctuation with a certain wavelength $\lambda = 2\pi/q$ is amplified or damped.

2.3.1 Navier–Stokes Equation

The classical hydrodynamic theory [12, 13] describes the motion of an incompressible Newtonian fluid. The motion of a fluid can be completely described if its average velocity $\bar{v}$ and the external pressure p that acts at the free interface are known. The equation of motion is the *Navier–Stokes equation* that is

basically Newton's law written for an infinitesimal element of fluid: the product of mass and acceleration is equal to the sum of the forces acting on the volume element:

$$\rho \left[\frac{\partial v}{\partial t} + (v \cdot \nabla) \cdot v \right] = -\nabla p + \eta \nabla^2 v + f \tag{2.10}$$

The right hand side* of Eqn.(2.10) gives the total force that acts on the fluid element as a sum of three contributions: (1) the external pressure that acts at the free interface, (2) a viscous force due to the transferred momentum from faster moving layers to slower moving layers throughout the liquid and (3) the influence of external volume forces, such as gravity.

The left hand side of Eqn.(2.10) is the product of fluid density ρ and acceleration. This term contains the acceleration $\partial v/\partial t$ in a fixed coordinate system and a quadratic $(v \cdot \nabla) \cdot v$ or *"convective"* term that makes the hydrodynamic equation non–linear. Because we use fluids with very large viscosities, the velocity gradients are very small and the convective term can be neglected. Furthermore, because the dynamics of the viscous liquid film is very slow, the velocity profile can be always considered in quasi–steady–state (i.e $\partial v/\partial t = 0$). With the above considerations and neglecting gravity ($f = 0$), Eqn.(2.10) becomes:

$$0 = -\nabla p + \eta \nabla^2 v \tag{2.11}$$

To compute the average velocity from Eqn.(2.11), the boundary conditions must be known. For the thermally excited capillary waves the most important boundary conditions are those related to the values of stresses at the substrate–liquid and liquid–air interfaces.

At the free interface (i.e. air–liquid interface) the stress that acts from within the liquid must be counterbalanced by stresses due to surface forces. In terms of the continuity relation this condition can be expressed as

$$\eta_{\text{liquid}} \cdot \partial_z v_{\text{liquid}}(z) = \eta_{\text{air}} \cdot \partial_z v_{\text{air}}(z) \tag{2.12}$$

Because no stresses can exist in the gas phase (air), the stress at the surface must vanish. This is accomplished when the sum of the viscous stress and the surface stress is zero. Therefore, Eqn.(2.12) becomes:

$$\sigma_{xz} = \eta \partial_z v_{\text{liquid}}(z) = 0 \tag{2.13}$$

* $\nabla^2 = \frac{\partial^2}{\partial x^2} + \frac{\partial^2}{\partial y^2} + \frac{\partial^2}{\partial z^2}$

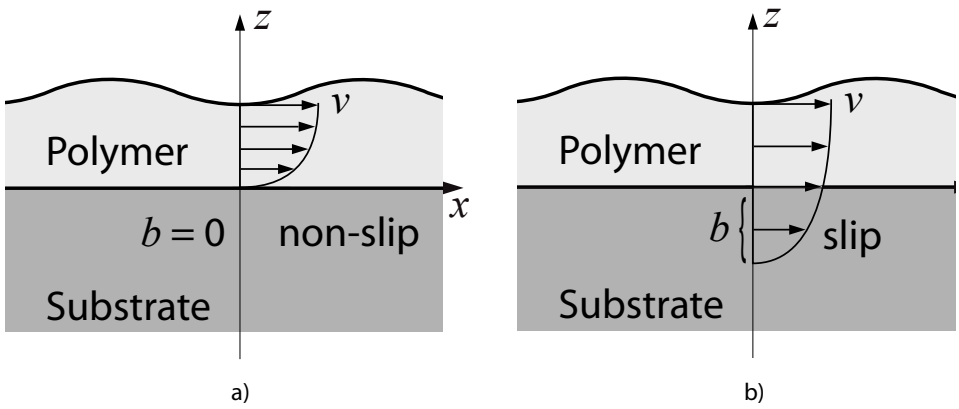

Figure 2.4: The two situations defining the behavior of a liquid near the substrate's surface. a) No–slip behavior ($b = 0$) implies that the velocity vanishes at the substrate. b) Definition of the extrapolation length b that determines the slip behavior.

Considering the non–zero component of the velocity vector only in the Ox direction as a function of the z coordinate (Poiseuille type of flow)

$$\partial_{zz} v(z) = \frac{1}{\eta}(\partial_x p) \tag{2.14}$$

Integrating Eqn.(2.14) we obtain:

$$v(z) = \frac{1}{2\eta}(\partial_x p) \cdot z^2 + c_1 \cdot z + c_2 \tag{2.15}$$

When computing the constants c_i from the initial conditions we distinguish two situations (Fig. 2.4).

Non–slip boundary condition for the liquid flow

A non–slip boundary condition at the substrate implies that at $z = 0$, the liquid velocity $v = 0$. Assuming that the fluid is at rest at the wall, implies that the substrate hinders the flow along its surface.

Using the no stress condition at the free surface ($z = h$), the velocity profile is obtained:

$$v(z) = \frac{1}{2\eta}(\partial_x p)(z - 2h)z \tag{2.16}$$

and the mean velocity in the film is

$$\bar{v} = \frac{1}{h}\int_0^h v(z)dz = \frac{h^2}{3\eta}(-\partial_x p) \tag{2.17}$$

Slip boundary condition for the liquid flow

The amount of slip of the fluid at liquid–substrate interface is usually characterized by the *extrapolation length*. This parameter is related to the friction forces that act between the liquid and the surface. Assuming a finite velocity at the substrate v_s, the shear stress at the solid–liquid interface σ induced by the flow is:

$$\sigma = k \cdot v_s \tag{2.18}$$

where k is the surface friction coefficient. This stress must be compensated by the viscous shear stress inside the fluid:

$$\sigma = k \cdot v_s = \eta \left| \frac{\partial v(z)}{\partial z} \right| \tag{2.19}$$

where $v(z)$ is the fluid velocity that increases with z. From Eqn.(2.18) and Eqn.(2.19), the slip velocity is calculated

$$v_s = \frac{\eta}{k} \left| \frac{\partial v(z)}{\partial z} \right| = b \cdot \left| \frac{\partial v(z)}{\partial z} \right| \tag{2.20}$$

where

$$b = \frac{\eta}{k} \tag{2.21}$$

The extrapolation length b in Eqn.(2.21) determines the dynamic behavior of the liquid film. The initial conditions when considering a slip motion at the solid–liquid interface are:

- at the substrate ($z = 0$) the velocity $v(z = 0) = v_s$
- at the free interface ($z = h$), $\eta \cdot \partial_z v = 0$

Using these initial conditions, the constants c_1 and c_2 in Eqn.(2.15) are easily computed and the velocity of a fluid volume at distance z from the substrate becomes:

$$v_{\text{slip}}(z) = \frac{1}{\eta}\left[\frac{z^2}{\eta} - (z-b)h\right](\partial_x p) \tag{2.22}$$

and the mean velocity in the film when slippage is considered is

$$\bar{v}_{\text{slip}} = \frac{1}{h}\int_0^h v_{slip}(z)dz = \frac{h(h+3b)}{3\eta}(-\partial_x p) \tag{2.23}$$

Once the mean velocity in the film is known, the next step is to use the continuity equation to calculate the flux that passes through an area of cross–section $\mathcal{A}$. In the 1–dimensional case ($\mathcal{A} = h$) and considering the non–slip conditions, the flux j is:

$$j = \mathcal{A}\cdot\bar{v} = \frac{h^3}{3\eta}(-\partial_x p) \tag{2.24}$$

When taking slip into account Eqn.(2.24) becomes:

$$j = \mathcal{A}\cdot\bar{v}_{\text{slip}} = \frac{h^2(h+3b)}{3\eta}(-\partial_x p) \tag{2.25}$$

Eqn.(2.24) or Eqn.(2.25) are needed to compute the dispersion relation of the film instability. A second required equation is the well–known *continuity equation*, which is determined by the conservation of mass of a small *stationary* volume element within a fluid that flows

$$(\partial_t \mathcal{A})\mathrm{d}x = (\mathcal{A}\cdot\bar{v})_{x+\mathrm{d}x} - (\mathcal{A}\cdot\bar{v})_x \tag{2.26}$$

On the other hand

$$(\mathcal{A}\cdot\bar{v})_{x+\mathrm{d}x} - (\mathcal{A}\cdot\bar{v})_x = \partial_x(\mathcal{A}\cdot\bar{v})\mathrm{d}x$$

so that for the 1–dimensional case ($\mathcal{A} = h$ and $\mathcal{A}\cdot\bar{v} = j$):

$$\partial_t h + \partial_x j = 0 \tag{2.27}$$

The final form (Eqn. 2.27) of the continuity equation implies that any change in the height of the film results in a flow in lateral direction, thereby

redistributing the material from the valleys to the peaks of the undulations. Combined with Eqn.(2.24) or Eqn.(2.25), this yields the equation of motion for the film surface:

- for the non–slip situation:

$$\partial_t h = \partial_x \left[\frac{h^3}{3\eta} (\partial_x p) \right] \tag{2.28}$$

- and for slip

$$\partial_t h = \partial_x \left[\frac{h^2(h+3b)}{3\eta} (\partial_x p) \right] \tag{2.29}$$

2.3.2 Interfacial Pressure

To compute the dynamics of the air–liquid interface, the overall pressure p that acts at the surface of the liquid film has to be determined. The pressure p is given by the sum of several contributions, such as surface tension, van der Waals forces, temperature fluctuations induced forces and forces that arise from externally applied electric fields, temperature gradients, magnetic fields, etc. One of the most important contributions to the interfacial pressure comes from the surface tension. In the absence of any other external pressure, all the fluctuations are damped due to surface tension because the system minimizes its surface. Therefore, it is useful to express the generalized pressure p using three contributions:

$$p(h) = p_0 + p_{\mathrm{L}}(h) + p_{\mathrm{ex}}(h) \tag{2.30}$$

where p_0 is the atmospheric pressure, which is independent of the film thickness, $p_{\mathrm{L}}(h)$ is the Laplace pressure due to surface tension and $p_{\mathrm{ex}}(h)$ is a term that includes any excess surface pressure, usually called the *conjoining* or *disjoining*[1] pressure, depending on its sign. In the following paragraphs, the most important pressures are considered, which were used to explain the experimental results of this thesis.

[1] The disjoining pressure was first introduced by Derjaguin [14] and is usually only used for repulsive interactions in the context of wetting films. It is the pressure that the film exerts on its boundaries pushing them apart (disjoining them), therefore stabilizing the film.

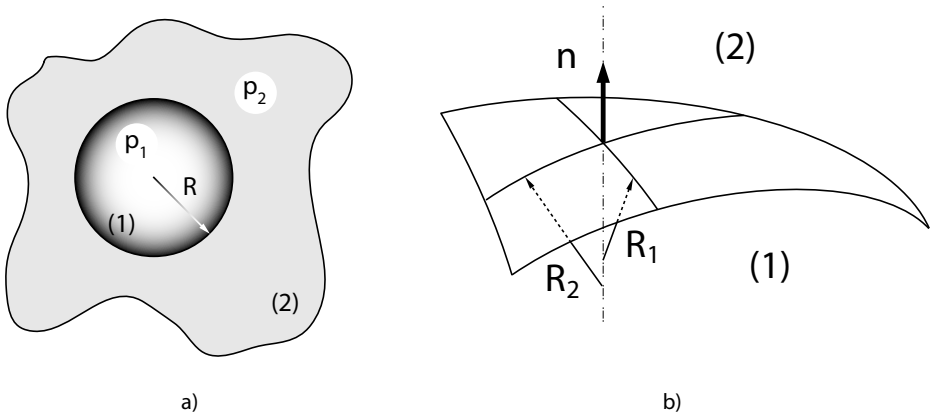

Figure 2.5: a) The capillary pressure difference $p_1 - p_2$ between the inner (1) and outer (2) region of a spherical fluid drop immersed in an external fluid. b) The geometry of an arbitrary boundary surface between two fluids (1) and (2), illustrating the definition of the principal radii of curvature $\boldsymbol{R}_1$ and $\boldsymbol{R}_2$.

Laplace pressure

The cohesive forces between liquid molecules are responsible for the surface tension. The molecules at the liquid's surface are not surrounded by other molecules and consequently they cohere more strongly to their neighbors. Any liquid behaves as if its free surface is a flexible membrane having a constant tension γ per unit length. It is important to note that γ is a force per unit length. Its value depends on the following factors:

1. The nature of the liquid.
2. The nature of the substance (solid, liquid or gas) in contact with the liquid.
3. The temperature and pressure.

One way of thinking of the surface tension is in terms of the surface free energy $\mathcal{F}$. The larger the surface, the more the free energy increases. To minimize $\mathcal{F}$, liquids assume the shape with the smallest surface area. This is

why small drops of water are round – a sphere is the shape with the minimum surface area for a given volume. Another example are soap bubbles which also tend to form into shapes with a minimal surface area.

When stretching a thin film of fluid, the film resists. Thus, in order to increase the surface by an amount $\mathrm{d}S = L\mathrm{d}\ell$, the change in the energy $\mathrm{d}W$ has to equal to the work done by the force F

$$\mathrm{d}W = F\mathrm{d}\ell = 2\gamma L\mathrm{d}\ell = 2\gamma\mathrm{d}S$$

Considering a spherical drop (1) immersed into a liquid (2) (Fig. 2.5), its equilibrium is reached when the pressure inside the drop p_1 exceeds the pressure outside p_2 by an amount:

$$p_1 - p_2 = \frac{2\gamma}{R} \tag{2.31}$$

For the 1–dimensional case, the radius of curvature is given by $1/R = -\partial_{xx}\ell$ and Eqn.(2.31) becomes

$$p_L = -\gamma\partial_{xx}\ell \tag{2.32}$$

van der Waals Pressure

van der Waals forces [15] are attractive or repulsive forces that exist between any kind of molecules. They are responsible for the cohesion of molecular crystals and liquids. These forces are different from those due to bond formation or electrostatic interactions of ions or ionic groups with one another. van der Waals forces arise from dipole–dipole or dipole–induced dipole interactions and London (instantaneous induced dipole-–induced dipole) interactions.

The nature of the attractive forces between neutral molecules was first recognized (1930) by the Polish–born physicist Fritz London [16]. Using a quantum mechanical approach, he explained the forces in terms of the electron motion within molecules. London pointed out that at any instant of time, the center of the negative charge of the electrons and the center of the positive charge of the atomic nuclei are not likely to coincide. Thus, the fluctuation of electrons give rise to time–varying dipoles, even though the average of this instantaneous polarization is zero. The instantaneous dipoles polarize adjacent molecules, resulting in an attractive force.

Long–range van der Waals forces account for a wide range of physical phenomena, such as friction, surface tension, adhesion and cohesion of liquids

and solids, viscosity and the discrepancies between the behavior of gases from the predictions of the ideal gas law. In the classic approach, van der Waals forces can be calculated by summing over binary potentials that decay with distance as $1/r^n$ of all atoms in the bodies. A more complete theory based on the dielectric properties of the material was developed by Lifshitz [17]. The van der Waals force between two media (1 and 2) interacting through a medium (3) of a thickness h varies as:

$$P_{\mathrm{vdW}} = -\frac{A_{132}}{6\pi h^3}$$

where A_{132} is the non–retarded *Hamaker constant* defining the magnitude of the force. Depending on its sign, the force can be attractive ($A_{132} < 0$) or repulsive ($A_{132} > 0$).

If two dipoles are at an appreciable distance, the time needed for the electric field to travel from one to the other and back becomes comparable to the period of the fluctuating dipole itself. This means that the original dipole has already changed its orientation and the interaction becomes smaller. With distance, this retardation effect changes the strength of the van der Waals interaction and its scaling behavior.

$$P_{\mathrm{vdW}} = \frac{B_{132}}{h^4}$$

where B_{132} is the retarded Hamaker constant. The cross–over between the non–retarded and the retarded regime occurs over distances of the order of 10 nm.

Acoustic Casimir Disjoining Pressure

In 1948 Casimir [18] predicted the attractive force between two perfectly conducting plates brought in close proximity. Casimir explained this force as arising from the confinement of zero–point vacuum electromagnetic fluctuations. Later, the new concept of *radiation pressure* helped to explain the attractive nature of the Casimir force in simpler terms. The radiation pressure is associated with the quantum electrodynamic (QED) vacuum field fluctuations that cover the entire frequency spectrum. Because the modes in the space outside the plates form a continuum whereas those inside are restricted to discrete values, there are “more” modes outside to push the plates together.

This force, due to exclusion of electromagnetic modes between the plates has the magnitude:

$$P_{\text{Casimir}} = \frac{\pi\hbar c}{240h^4}$$

where h is the plate distance.

Experimental determinations of the Casimir force were recently performed by Lamoreaux [19] for a system consisting of two conductors in the form of a flat plate and a sphere. Analogous to the electromagnetic effect, Larraza et al. [20] introduced the notion of an acoustic Casimir effect by measuring the force between two plates in an external sound field. In the absence of an external source, Bschorr [21] calculated the force between two bodies, considering the thermal–pressure of air fluctuations.

Schäffer et al. [22] assumed an ideal elastic liquid medium. According to Debye [23], longitudinal waves in liquids can exist only up to the Debye frequency $\nu_D = u_i[9N_A/4\pi\mathcal{V}]^{1/3}$ where u_i is the sound velocity, N_A is Avogadro's number and $\mathcal{V}$ is the molar volume. The radiation pressure exerted by longitudinal waves that propagate normal to a surface was estimated by Schäffer et al. [22]. The phonon pressure in one of the six orthogonal directions is:

$$P_{\text{ac}} = \frac{1}{3} \cdot e \tag{2.33}$$

where e is the the phonon energy density. The net acoustic radiation pressure is readily calculated as:

$$\begin{aligned} P_{\text{ac}} &= \frac{1}{3}\left[\int_0^{\nu_D^{(1)}} kT\mathrm{dn}_1 - \int_{\nu_c}^{\nu_D^{(2)}} \mathrm{kTdn}_2\right] \\ &= \frac{\pi kT}{18h^3} + \frac{4\pi kT}{9}\left[\left(\frac{\nu_D^{(1)}}{u_1}\right)^3 - \left(\frac{\nu_D^{(2)}}{u_2}\right)^3\right] \\ &= \frac{\pi kT}{18h^3} + p_0 \end{aligned} \tag{2.34}$$

where $dn_i = 4\pi\nu^2/u_i^3 \mathrm{d}\nu$ is the density of states for medium i and the integration is performed over all relevant phonon frequencies. ν_D^i are the Debye frequencies in the media up to which phonons can exist and ν_c is the cut–off frequency ($\nu_c = u_i/\lambda_c = u_i/2h$) for the wavelengths inside of a film of thickness h. p_0 is a pressure term that does not depend on the film thickness.

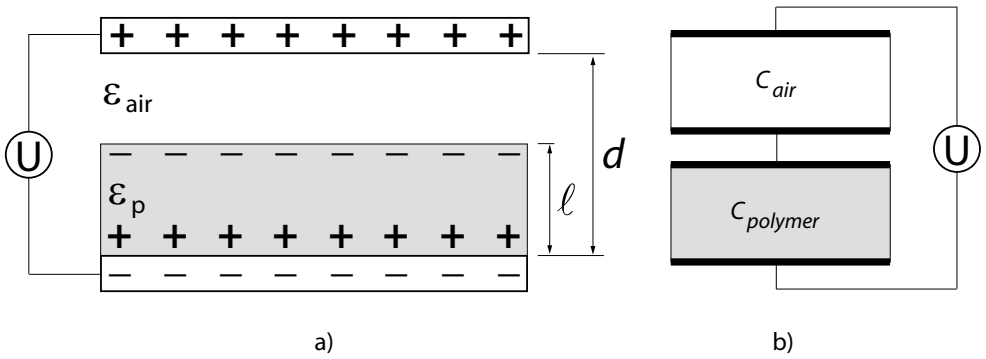

Figure 2.6: The dielectric material is polarized in the presence of the electric field, resulting in an effective attraction between the opposing charges. The layered system is equivalent to a series of capacitors.

Electrostatic Pressure

When an electric field is applied across a polymer liquid–air interface, it polarizes the polymer, resulting in an effective surface charge density [24, 25, 26]. If the polymer is in a capacitor geometry (Fig. 2.6a) the charges at the polymer–air interface experience an attractive interaction with the charges from the upper electrode. The electrostatic pressure at the liquid–air interface for a given electric field in the polymer is:

$$p_{\text{el}} = -\frac{1}{2}\epsilon_0\epsilon_p(\epsilon_p - 1)E_p^2 \tag{2.35}$$

where ϵ_0 and ϵ_p are the dielectric constants for vacuum and for the polymer, respectively and E_p is the magnitude of the electric field in the polymer. E_p can be easily calculated by considering the total capacitance as a sum of two capacitors in series (Fig. 2.6b). Thus

$$\frac{1}{C} = \frac{1}{C_{\text{air}}} + \frac{1}{C_p} = \frac{\ell}{\epsilon_0\epsilon_p\mathcal{A}} + \frac{d-\ell}{\epsilon_0\epsilon_p\mathcal{A}} = \frac{\epsilon_p d - (\epsilon_p - 1)\ell}{\epsilon_0\epsilon_p\mathcal{A}} \tag{2.36}$$

where d is the distance between the capacitor electrodes and ℓ is the polymer film thickness. The corresponding free energy stored in a capacitor is

$$\mathcal{F} = \mathcal{F}_0 - \frac{1}{2}CU^2 \tag{2.37}$$

where U is the voltage applied on the capacitor electrodes. The variation of the free energy $\mathcal{F}$ with the polymer film thickness ℓ per unit area gives the electrostatic pressure in the polymer.

$$p_{\mathrm{el}} = \frac{1}{\mathcal{A}} \frac{\partial \mathcal{F}}{\partial \ell} = \frac{U^2}{2\mathcal{A}} \partial_\ell C \tag{2.38}$$

Inserting Eqn.(2.36) into Eqn.(2.38) results

$$p_{\mathrm{el}} = -\frac{\epsilon_0 \epsilon_p (\epsilon_p - 1) U^2}{2[\epsilon_p d - (\epsilon_p - 1)\ell]^2} \tag{2.39}$$

Comparing Eqn.(2.35) with Eqn.(2.39), the electric field in the polymer can be extracted:

$$E_{\mathrm{p}} = \frac{U^2}{\epsilon_p d - (\epsilon_p - 1)\ell} \tag{2.40}$$

2.3.3 Linear Stability Analysis and Dispersion Relation

The theoretical task is to find an analytical solution for the response of a system to a perturbation, to test whether it lowers its energy. For a liquid surface we make a sinusoidal ansatz:

$$h(x,t) = h_0 + \zeta e^{iqx + \frac{t}{\tau}} \tag{2.41}$$

where a film with a initial thickness h_0 undergoes a deformation (i.e. a fluctuation) with an amplitude ζ much smaller than the initial film thickness $\zeta << h_0$. Keeping only the terms linear in ζ (*linear stability analysis*) and taking the derivatives in Eqn.(2.28) we obtain:

$$\begin{aligned}
\partial_t h &= \frac{h^2}{\eta} (\partial_x h) \left[\partial_x p\right] + \frac{h^3}{3\eta} \left[\partial_{xx} p\right] \\
&= \frac{h^2}{\eta} (\partial_x h) \left[-\gamma (\partial_{xxx} h) + (\partial_h p_{ex})(\partial_x h)\right] \\
&\quad + \frac{h^3}{3\eta} \left[-\gamma (\partial_{xxxx} h) + (\partial_{hh} p_{ex})(\partial_x h)^2 + (\partial_h p_{ex})(\partial_{xx} h)\right].
\end{aligned} \tag{2.42}$$

where we used Eqn.(2.30) for the external pressure and Eqn.(2.32) for the Laplace pressure. Eqn.(2.42) simplifies to:

$$\partial_t h = \frac{h_0^3}{3\eta} \left[-\gamma (\partial_{xxxx} h) + (\partial_h p_{ex})(\partial_{xx} h)\right] + O(\zeta^2). \tag{2.43}$$

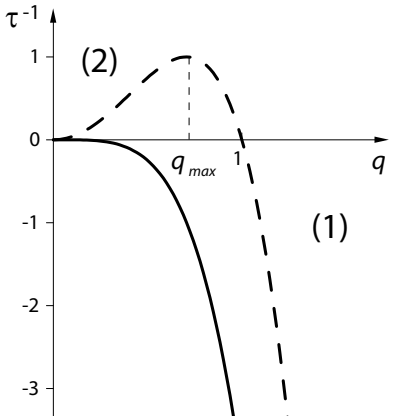

Figure 2.7: Dispersion relation. In the absence of any external pressure $p_{\text{ext}} = 0$ *all the fluctuations are damped (continuous line). For a finite external pressure (dotted line) the film develops a characteristic wavelength* $\lambda_{\max} = 2\pi/q_{\max}$.

After taking the partial derivatives in Eqn.(2.43) and dividing by $\zeta \exp(iqx + t/\tau)$, in the case of non–slip boundary conditions:

$$\frac{1}{\tau} = -\frac{h_0^3}{3\eta}\left[\gamma q^4 + \Delta\Phi q^2\right]. \tag{2.44}$$

and for slip:

$$\frac{1}{\tau} = -\frac{h_0^2(h_0 + 3b)}{3\eta}\left[\gamma q^4 + \Delta\Phi q^2\right]. \tag{2.45}$$

These equations are the *dispersion relations* of the liquid film, relating the time constant τ to the wave vector q of a sinusoidal film perturbation. $\Delta\Phi$ is the curvature of the free energy of interaction, or equivalently, the gradient of the excess surface pressure with respect to the film thickness h, $\partial_h p_{\text{ex}} = \Delta\Phi$. The dispersion relation determines whether a wave with a wavevector q is amplified or damped. Representing the inverse of the time needed for each fluctuation to develop $1/\tau$ vs. the wave vector q (Fig. 2.7), two curves are distinguished

In the absence of any externally applied pressure (p_{ext}=0) all fluctuations are damped because of the surface tension. The film minimizes its surface, all perturbations are exponentially damped and the film is intrinsically stable.

When coupling an external pressure to the surface, the dynamics of the film is represented by the dotted curve in Fig.(2.7). There are two regimes.

- (1) the region of small wavelength fluctuations (i.e. large values of q). To sustain these fluctuations, the liquid film has to increase its surface, which is energetically unfavorable. Therefore, all the small wavelength fluctuations are damped.
- (2) the region of large wavelength fluctuations (i.e. small values of q). In this region, the waves are exponentially amplified but a large amount of material has to be moved.

The film selects the best compromise between (1) and (2) and develops a characteristic wavelength $\lambda_{\max}$. The fastest growing mode $q_{\max} = 2\pi/\lambda_{\max}$ is given by the maximum of Eqn.(2.44) or Eqn.(2.45)

$$q_{\max}^2 = -\frac{\Delta\Phi}{2\gamma} = -\frac{\partial_h p_{\text{ext}}}{2\gamma} \tag{2.46}$$

and the characteristic wavelength is:

$$\lambda_{\max} = \sqrt{\frac{-2\gamma}{\partial_h p_{\text{ext}}}} \tag{2.47}$$

Because Eqn.(2.47) does not depend on the viscosity, η influences only the associated maximal growth rate.

$$\frac{1}{\tau_m} = \begin{cases} \gamma \frac{h_0^3}{3\eta} q_{\max}^4 & \text{no} - \text{slip} \\ \gamma \frac{h_0^2(h_0+3b)}{3\eta} q_{\max}^4 & \text{slip} \end{cases} \tag{2.48}$$

The two characteristic quantities $\lambda_{\max}$ and $\tau_{\max}$ describe the static and dynamic behavior of the film. Although the characteristic wavelength is easy to predict and to measure, the dynamics of the film is more problematic. The complications in predicting and measuring the time constant $\tau_{\max}$, arise from the fact that the final film morphology does not give any information on the dewetting kinetics.

Bibliography

[1] A.Y. Grosberg, A.R. Khokhlov; *Giant molecules*. Academic Press, San Diego, 1997.

[2] P. Flory; *Principles of Polymer Chemistry*; Cornell Univ. Press, Ithaca, New York, 1971

[3] F.W. Billmayer; *Textbook on Polymer Science*; John Wiley & Sons, 1984

[4] J.M.G. Cowie; *Polymers: Chemistry and Physics of Modern Materials*; Internatioal Textbook Co, 1973

[5] G. Strobl; *The Physics of Polymers*; Springer–Verlag, Berlin, 1997

[6] P.G. de Gennes; *Scalling Concepts in Polymer Physics*, Cornell Uni. Press, Ithaca and London, 1996

[7] M. Huggins; *J. Phys. Chem.* **46**, 1942

[8] M. Huggins; *Ann. N. Y. Acad. Sci.* **41**, 1942

[9] M. Huggins; *J. Am. Chem. Soc.* **64**, 1942

[10] A. Vrij; *J. Colloid Sci.* **19**, 1964

[11] see the references in the introductory chapter regarding "Capillary Instabilities in Thin Films"

[12] E. Guyon, J.-P. Hulin, L. Petit, C. Mitescu; *Physical Hydrodynamics*, Oxford Univ. Press, 2001

[13] L.D. Landau, E.M. Lifshit; *Fluid mechanics*, Pergamon Press, London, 1959

[14] B. Derjaguin, N. Churaev; *Kolloidn Zh.* **38**, 1976

[15] J.N. Israelachvili; *Intermolecular and surface forces.*, Academic Press, London, 1991

[16] R. Eisenschitz, F. London; *Z. Physik* **60**, 1930; F. London; *Trans. Faraday Soc.* **33**, 1937

[17] E.M. Lifshitz; *Soviet Physics* **2**, 1956

[18] H.B.G. Casimir; *Proc. Kon. Ned. Akad. Wetensch.* **51**, 1948.

[19] S.K. Lamoreaux; *Phys. Rev. Lett.* **78(1)**, 1997

[20] A. Larraza, C.D. Holmes, R.T. Susbilla, B. Denardo; *J. Acoust. Soc. Am.* **103(5)**, 1998

[21] O. Bschorr; *J. Acoust. Soc. Am.* **106(6)**, 1999.

[22] E. Schäffer, U. Steiner; *Eur. Phys. J. E* **8**, 2002

[23] P. Debye; *Ann. Phys.* **39**, 1912

[24] E. Schäffer, T. Thurn–Albrecht, T.P. Russell, U. Steiner; *Nature* **403**, 2000

[25] E. Schäffer, T. Thurn–Albrecht, T.P. Russell, U. Steiner; *Europhys. Lett.* **53**, 2002

[26] Z. Lin, T. Kerle, S.M. Baker, D.A. Hoagland, E.K. Schäffer, U. Steiner, T.P. Russell, *J. Chem. Phys.* **114(5)**, 2001

Chapter 3

Materials & Experimental Techniques

3.1 Sample preparation

3.1.1 Polymers

Standard polymers were used for the studies performed in this thesis. They have a glass transition temperature T_g around 100°C and a narrow molecular weight distribution characterized by low polydispersity indices M_w/M_n . We used polystyrene (PS)[1], poly(methyl methacrylate) (PMMA)[2], polyacrylamide (PAAM)[3], poly(vinyl methyl ether) (PVME)[4] and poly(dimethyl siloxane) (PDMS)[5], utilized as obtained without further purification. Their physical properties provided by the producer are summarized in Table 3.1. The values of their dielectric constants and refractive indices corresponds to room temperature. The air–polymer surface tension γ is of practical importance and plays

[1] purchased from PSS Mainz, Fluka
[2] purchased from Fluka
[3] purchased from Sigma–Aldrich
[4] purchased from Scientific Polymer Products, Polymer Source
[5] purchased from Dow Corning, ABCR

Table 3.1: *Physical properties of the polymers.*

Polymer	$M_{\mathrm{w}}^{(\mathrm{a})}$ (kg/mol)	$PD^{(\mathrm{b})}$	$T_{\mathrm{g}}^{(\mathrm{c})}$ (°C)	$\epsilon^{(\mathrm{e})}$	$n^{(\mathrm{f})}$
PS	1.2	1.05	100	2.5	1.59
PS	10.3	1.06	100	2.5	1.59
PS	108	1.03	100	2.5	1.59
PMMA	98.5	1.08	105	3.6	1.492
PAAM	2.1	1.21	170	2.5	1.4
PVME	50.3	1.1	-30	2.5	1.52
PDMS	100	1.2	-30	4.7	1.38

(a) Weight-averaged molecular weight.
(b) Polydispersity $PD = M_w/M_{\mathrm{n}}$, with M_{n} the number-averaged molecular weight.
(c) Glass transition temperature.
(e) Dielectric constant.
(f) Refractive index at room temperature in visible.

an important role in polymer blending, wetting, coating, adhesion, and foaming. Accurate surface tension data provided by [1, 2, 3, 4, 5, 6], for the molten polymers are given in Fig.(3.1). To coat the polymers on various substrates, we usually prepared 3% (by weight) solutions. However, to obtain ultrathin polymer films (1 – 10 nm range), very dilute solutions were made (0.02% by weight). The solvents used to dissolve the polymers are given in Table 3.2.

3.1.2 Substrates

The substrates used are tabulated in Table 3.3 together with some of their physical properties. All substrates were used as received. The (boron doped) silicon substrates with a conductivity of 6–12 Ω cm, were cut parallel to the (100) lattice plane. The wafers were covered with a 1.62 nm thick native silicon

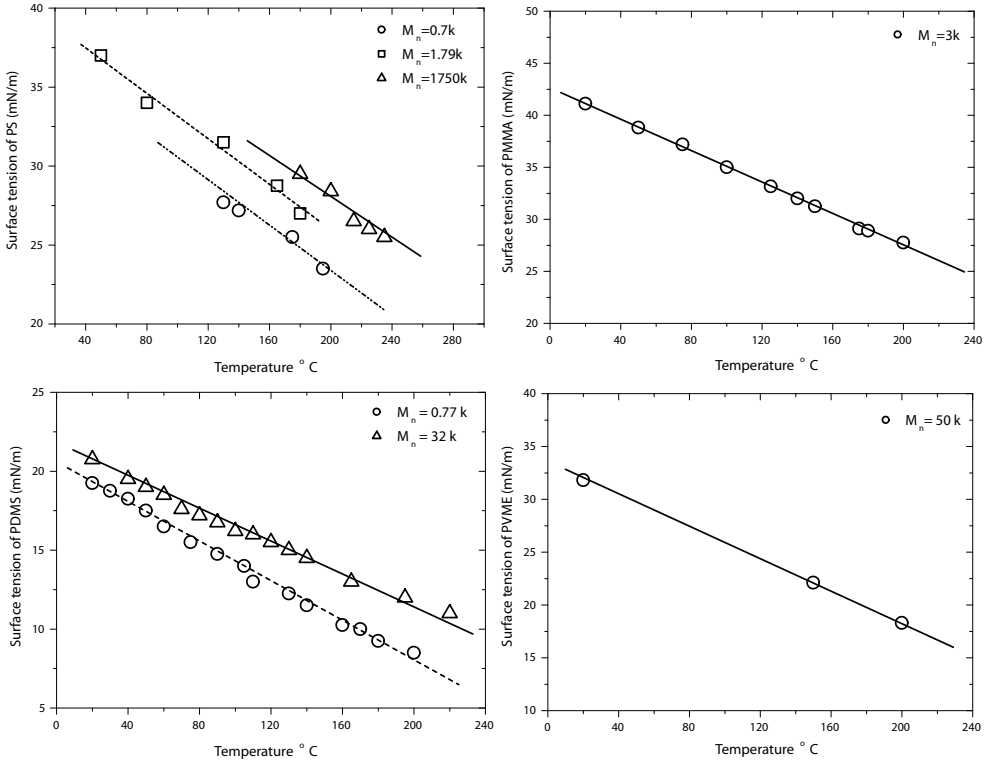

Figure 3.1: The dependence of surface tension on the temperature and molecular weight for the polymers used in this study. The data was taken from [1, 2, 3, 4, 5, 6].

Table 3.2: Solvents and non–solvents for the polymers used in this study.

Solvent / Polymer	PS	PMMA	PVME	PAAM	PDMS
cyclohexane	x	o	o	o	o
THF	x	x	x	x	x
acetic acid	o	x	o	o	o
ethanol	o	ox	o	x	o
water	o	o	x	x	o
toluene	x	x	x	o	x

x – good solvent
o – bad or non–solvent

oxide layer. For some experiments the oxide layer thickness was increased by thermal growth at 900° C for 3 hours in air, using a high temperature oven. The resulting thickness of the oxide layer was 80 nm. The roughness of all substrates was measured by tapping–mode atomic force microscopy and their optical properties were determined by ellipsometry ($\lambda = 532$ nm).

3.1.3 Substrate preparation

To study the influence of substrates on the stability of thin polymer films, it is imperative to provide homogeneous substrates free of impurities or chemical contaminations. To remove macroscopic particles and organic contaminations, a jet of carbon dioxide crystals was used. This cleaning technique is also known as "snow–jet" [7]. Subsequently, the substrate was immersed in hot "piranha"[6] solution. The substrate was then thoroughly washed in deionized water. A simple way of verifying whether the substrate is clean, is to measure the contact angle of a sessile water drop on the surface. The proof that the

[6]Piranha Solution consists of 1/2 w/w sulfuric acid and hydrogen peroxide. It is a strongly oxidizing liquid. When applied hot (80°C) for at least 0.5 hours, it removes all organic contaminations from a substrate such as silicon wafers or glass. Note: polished glass surfaces such as prisms or lenses may show an increased roughness after this treatment.

Table 3.3: Physical properties of the substrates.

Substrate	n	ϵ	RMS	Source
Glass	1.50	3.8	< 1.5 nm	Menzel–Gläser
Glass	1.52	3.8	< 1.8 nm	Menzel–Gläser
Glass	1.60	3.8	< 0.8 nm	Hellma Optik GmbH
Glass	1.70	3.8	< 1.5 nm	Nanofilm GmbH
Si Wafer	4.7	16.2	< 0.1 nm	WaferNet GmbH
SiO_x	1.46	3.8	< 0.1 nm	–
$SiO_x{}^{\text{thermic}}$	1.49	3.8	< 0.5 nm	–
MgF_2	1.38	5.45	< 1.2 nm	Edmund Optics Ltd.

substrate was free of impurities was obtained when the water droplet spread to form a continuous film. All substrates were used immediately after the cleaning process. If kept a single day at ambient conditions the water contact angle increased from 0° to 7° due to the adsorption of hydrocarbon contaminations and dust particles.

As a further efficient cleaning method, etching in an ozone plasma was used. The substrate was kept for approximatively 1/2 hours inside a radio frequency plasma discharge in air. The water contact angle dropped from an initial value of 15° to 0° (complete wetting).

In some experiments the back side of the silicon wafer was coated with a thin layer of gold. To provide sufficient adhesion between the metal and the SiO_x surface of the wafer, a 2 nm thick chromium or titanium layer was deposited. The deposition of this "anchoring" layer was followed by the deposition of a 100 nm thick gold layer.

3.1.4 Spin–Coating Method

One of the most commonly used techniques in the semiconductor industry to coat substrates with thin polymer layers is the spin–coating technique. A

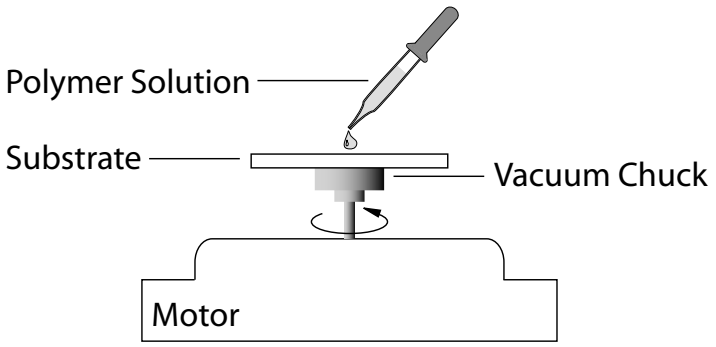

Figure 3.2: Representation of the spin–coating process, used to produce smooth, homogeneous polymer films.

droplet of a polymer solution is placed on the substrate, which is then set in rotation (Fig. 3.2). The spin–coating process can be divided in four stages [8].

- **Stage one:** the deposition of the coating fluid onto the substrate. One potentially important issue is, whether the solution wets the substrate during this dispense stage. If not, incomplete coverage may result.
- **Stage two:** the substrate is accelerated up to its final rotation speed and the fluid spreads over the surface. The liquid film thins until the viscous shear drag balances the rotational acceleration. Ultimately, the wafer reaches its final speed and the fluid co–rotates with the substrate.
- **Stage three:** the substrate is spinning at a constant rate and fluid viscous forces dominate the thinning behavior. The film gradually thins and it is often is possible to see interference colors that change with time.
- **Stage four:** the substrate is spinning at a constant rate and the solvent evaporation rate dominates the thinning behavior. At a sufficiently low solvent content in the film, the polymer solidifies and forms a smooth film. The thickness h of the resulting film depends on the viscosity, the polymer concentration, and the spin-frequency f : $(h \propto \sqrt{1/f})$

The nature of the solvent is very important in determining the quality of the coating. The solvent has to evaporate slowly enough for the polymer

to release its stresses. For well chosen parameters, spin–coating results in extremely homogeneous polymer films.

When using rotation speeds between 800 rotations per minutes (RPM) and 10000 RPM and solution concentrations between 0.02% and 5%, we were able to produce polymer films with thicknesses ranging from a few Angstroms to several micrometers.

The spin–coating process is sensitive to a number of factors. Common defects are:

- **Comets**, which usually occur when large solid impurities impede the flow of the fluid across the surface
- **Striations**, which are radially oriented waves of thickness variation. These variations are thought to be driven by surface tension gradients that appear during solvent evaporation [9].
- **Environmental sensitivity**, which is a problem especially during summer season. During the spin–coating process, the evaporation of the solvent cools the film. By lowering its temperature, water condensates onto the sample surface. The water forms drops on the film surface, resulting in a characteristic drop imprint pattern.

These unwanted effects can be prevented or minimized by suitable choosing the solvent, solution concentration, rotation speed and humidity in the spin–coating chamber.

3.2 Microscopy

3.2.1 Optical Microscopy

In most of the cases, thin polymer films show beautiful interference colors if the substrate has a refractive index significantly different from the polymer. Even thickness variations on the order of a few nanometers can be easily visualized due to a slight color change. To observe thin polymer films, optical microscopy was used. Optical microscopes can be used to image samples:

- in **reflection**, where the light coming from the light source is reflected by the sample into the microscope objective. The observed contrast is due

to the ability of features on the sample to affect differently the reflected light intensity.

- in **transmission**, where the light shines through the sample into the objective.

In general, sample properties that produce changes in brightness or color arise from light absorption, reflection, spatial variation in refractive index, scattering, diffraction, birefringence, fluorescence, etc [10, 11, 12]. Common imaging techniques using these optical phenomena are:

- **Brightfield imaging** is the most common technique, widely used in optical microscopy for the past 300 years. In transmission, this method relies on the absorption of light to produce the contrast. In the case of reflection, reflections from the sample features give rise to the contrast.

- **Darkfield imaging** is the technique where the illuminated specimen does not emit light directly into the objective. The directly reflected light is blocked, while the light passing through the specimen from oblique angles is diffracted, refracted, and reflected into the microscope objective. This "residual" light forms a bright image of the specimen features on a dark background.

- **Differential interference contrast** is a technique where optical path gradients are converted into amplitude differences that improve the contrast of the resulting image. Those regions of the specimen where the optical path increases along a reference direction appear brighter (or darker), while regions where the path differences decrease appear with a reversed contrast.

- **Polarized light microscopy** is a technique that exploits the optical anisotropy of the sample to reveal detailed information about the structure and composition of materials. Polarized light is used in a contrast-enhancing technique to improve the quality of the image when imaging birefringent materials.

Other imaging techniques are phase contrast, Hoffman modulation contrast, and fluorescence. These useful techniques were designed to aid in contrast enhancement and to provide better observation and photomicrography

of specimens. Because the microscope is an instrument designed to make fine details visible, the better its resolution, the clearer are the images. The microscope resolution is the smallest separation between two object points that a given lens can still show as two distinct entities. High resolution refers to small values of the minimum resolvable distance, however, the maximal lateral resolution of optical microscopes is limited by the wavelength of imaging light to about 200 nm.

To characterize our samples, we used brightfield and darkfield microscopy (Olympus BX60 upright microscope and Olympus GX51 inverted microscope). The lateral topographic features investigated by optical microscopy ranged from 5 mm to 500 nm.

3.2.2 Atomic Force Microscopy

Scanning Tunnelling Microscopy (STM) was invented in 1986 by Binnig and Rohrer. The first instrument used a conductive tip, which when scanned over the sample surface, the small tip senses the substrate conductivity. The tunnelling current that flows through the tip is strongly dependent on the distance between tip and surface. STM was subsequently extended by Binnig, Quate and Gerber [13] to image also non–conducting samples. The new scanning method, called Atomic Force Microscopy (AFM), evolved rapidly as an imaging tool with high spatial resolution for soft materials. In comparison to traditional microscopes, which use electron or photon beams to create images, atomic force microscopy uses a hard sharp tip to probe the surface, combining an ease of use with the unparalleled ability to image surface features.

AFM uses various surface properties (e.g. topography, friction, hardness, etc.) to generate an image. It works in the same way as our fingers touch and probe the environment when we cannot see it. By using a finger to "visualize" an object by touching it, our brain is able to deduce its topography. The resolution of the method is determined by the radius of the fingertip. To achieve atomic scale resolution, a sharp stylus tip attached to a cantilever is used to scan an object point by point, thereby imaging its contour. The tips and the cantilevers come with a wide range of properties. The ones used in our experiments had a typical curvature radius of ≈ 10 nm and a height between 10 and 15 μm. Their oscillation frequency was between 150 and 300 kHz.

The scanning movement of the stylus is accomplished by a piezoelectric tube. However, a typical AFM image often presents artefacts. These are

elements of the image which do not belong to the sample, but rather are a product of the way in which the image has been acquired. Artefacts are ranged over probe artefacts, scanner and piezoelectric ceramic artefacts, artefacts resulting from instrument mechanical and electronic design, artefacts resulting from data manipulation and artefacts created by SPM samples [14].

The obtained AFM images are always a combination of the tip and sample geometry. The imperfect geometry and finite size of the tip contribute significantly to distortion of images. Thus, convolution is unavoidable but there are good chances to eliminate the artefacts and reconstruct a rather true image by using special mathematical methods. The scanner and piezoelectric ceramic artefacts can come from the scanner material characters and the mechanical construction of SPM scanners, such as non–linearity, creep, drift, hysteresis, etc. Other artefacts may result from instrument mechanical and electronic design such as, vibration between the SPM probe and sample, thermal stability, feedback control loop optimisation as well as electronic noise from a not properly grounded power supply.

To detect the movement of the cantilever, most AFMs employ an optical pointer technique. While the sample is scanned with respect to the tip, the topography of the specimen and lateral changes in the sample–tip interactions lead to a deflection of the cantilever. The magnitude of the deflection is measured with high precision by the reflection of a laser beam focused onto the back side of the cantilever. The typical setup of an AFM is shown in Fig.(3.3). It is either possible to directly record the signal representing the probe–sample interaction at each position, or to use a feedback electronics. In the latter case, a voltage is applied to the electrodes of a piezo ceramic that varies the tip–sample distance in such a way that the probe–sample interaction is kept constant. Such piezoelectric scan units can achieve picometer resolution in all three dimensions. The AFM feedback electronics is the heart of an AFM control unit. If the electronic feedback is switched on, the positioning piezo translator moves the sample (or tip) up and down, responding to changes in the force and alters the tip–sample separation to restore the force to a fixed set–point value. This mode of operation is known as constant force mode and it usually yields fairly faithful topographical images.

Lateral force microscopy (LFM) [15, 16], uses a 4–segment photodiode to enable the measurement of the torsion of the cantilever. As the cantilever is moved over the specimen surface, a variation in friction between the tip and

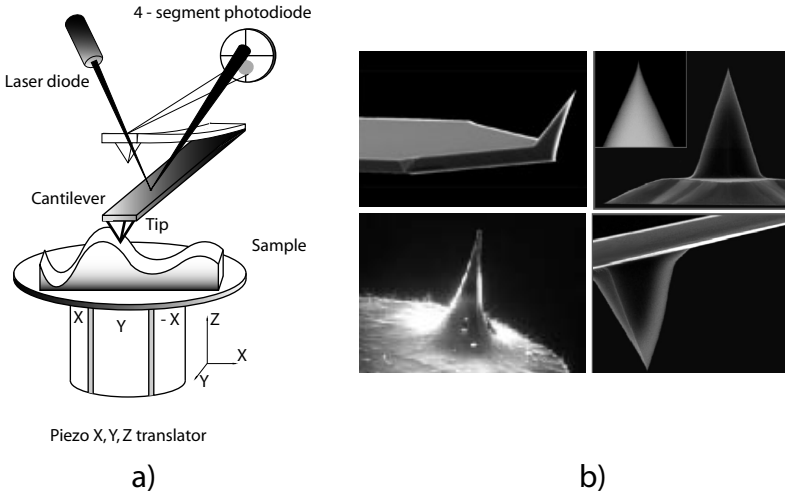

Figure 3.3: Principle of the AFM. (a) A fine tip is mounted on a cantilever spring and scanned over the surface. At sufficiently small forces the corrugations of the scanning lines represent the surface topography of the sample. The vertical deflection of the cantilever is detected by reflecting a laser beam onto a 4–segment photodiode. The photodiode signal is used to drive a servo system which controls the movement of the piezo xyz–translator. In this manner, the applied force between the tip and the sample can be kept constant within some tens of a piconewtons. (b) Scanning electron micrographs of different types of AFM tips.

sample gives rise to a variation in the cantilever torsion. This way, information about lateral chemical heterogeneities, such as different polymer phases with different friction coefficients can be measured at the same time as the sample topography.

An AFM can be operated in different modes depending on the tip–sample distance. These modes can be static or dynamic. In the static mode known as *contact mode*, the cantilever is scanned relative to the sample. Attractive and repulsive tip-sample forces bend the cantilever towards or away from the sample. According to Hooke's law, the magnitude of the tip–sample force is proportional to the cantilever deflection.

In the dynamic *tapping mode* [17, 18], the cantilever oscillates near its resonance frequency. Tip–sample interactions influence the amplitude, the phase, or the frequency of the cantilever oscillation. During the oscillations, the tip may (tapping) or may not (non–contact) touch the surface at its lower turnaround point. In the tapping mode, the contact of the tip with the sample is very short. Therefore, lateral forces are strongly reduced as the tip scans over the surface. When imaging poorly immobilized or soft samples, tapping mode is the better choice in comparison with the contact mode. In the case of long–range interactions, the frequency shift is proportional to the force gradient. More recently [19, 20], the phase imaging technique gain interest. To obtain this type of micrographs, the AFM measures the phase difference between the driving piezo and the cantilever oscillations. The precise origin of the image contrast is unknown, however it was demonstrated that it depends on sample properties such as stiffness and viscoelasticiy.

The magnification achieved by atomic force microscopes rivals to that of transmission and scanning electron microscopes (TEM and SEM, respectively). In general, AFM permits measurements down to the atomic scale, being therefore a very powerful and cost–efficient tool to employ in various research fields.

3.3 Ellipsometry

Ellipsometry was known for almost a century as a non–destructive optical method for measuring thicknesses and optical properties [21, 22, 23, 24] of thin films. Imaging Ellipsometry combines the power of ellipsometry with microscopy and has today many standard applications. It is mainly used in semiconductor research and fabrication to determine properties of layered stacks of thin films and the interfaces between the layers. Ellipsometry is also of increasing interest to researchers in other disciplines, such as biology and medicine. These areas pose new challenges, such as measurements of unstable liquid surfaces and microscopic imaging with ellipsometric contrast.

Ellipsometry measures the change in polarization and intensity of a light beam, upon reflection from a substrate, determining the thickness of the material and its complex refractive index. Linearly polarized light that is reflected from a surface has an elliptical polarization, as is shown in Fig.(3.4).

The *plane of incidence* (Fig. 3.5) is defined as the plane that includes

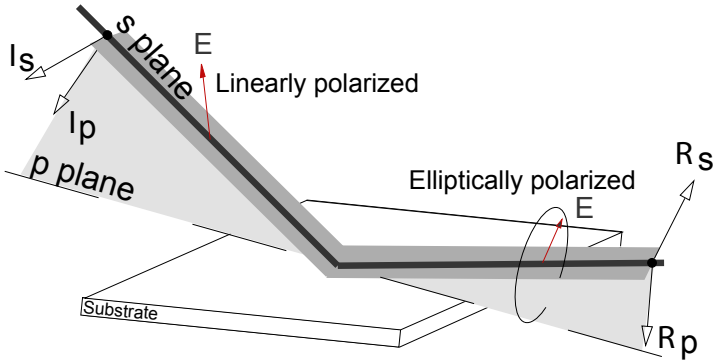

Figure 3.4: Geometry of an ellipsometric measurement: the incident light interacts with the sample and is partially reflected. The interaction of the light with the sample causes a change in polarization, from linear to elliptical polarization.

the incident and the reflected waves. It is common to define the x and y directions in such a way that x is parallel to the plane of incidence and y is perpendicular to it. These directions are referred to as p (for parallel) and s (for perpendicular). Thus, the electric field $\overrightarrow{E}$ can be resolved into its p and s components.

The Fresnel reflection coefficient R is the ratio of the amplitude of the reflected wave to the amplitude of the incident wave for a single interface. For the p and s waves, the reflection coefficients are given by

$$R_{1,2}^{\mathrm{p}} = \frac{\tilde{N}_2 \cos\phi_1 - \tilde{N}_1 \cos\phi_2}{\tilde{N}_2 \cos\phi_1 + \tilde{N}_1 \cos\phi_2}$$
$$R_{1,2}^{\mathrm{s}} = \frac{\tilde{N}_1 \cos\phi_1 - \tilde{N}_2 \cos\phi_2}{\tilde{N}_1 \cos\phi_1 + \tilde{N}_2 \cos\phi_2} \tag{3.1}$$

where the subscripts refer to medium (1) and (2) with complex refraction coefficients $\tilde{N}_1$ and $\tilde{N}_2$. The reflection coefficients are determined by the optical properties and the composition of the investigated system, consisting of a substrate with or without adsorbed or deposited layers.

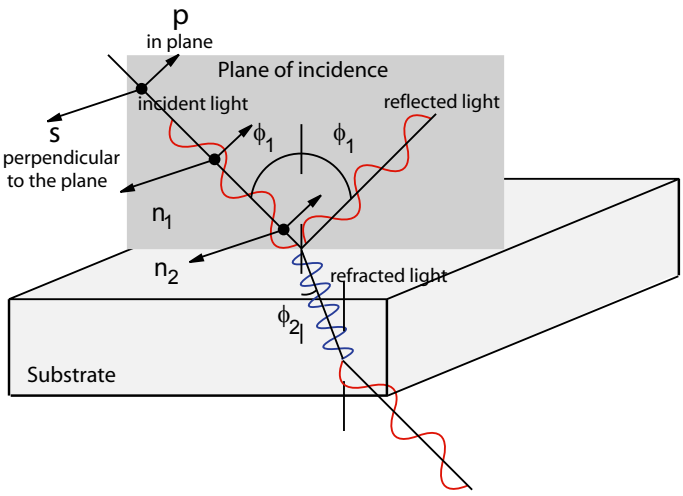

Figure 3.5: Definition of the basic terms of ellipsometry: ***the plane of incidence*** *is defined as the plane perpendicular to the surface of the sample.* ***The polarization state of the light*** *is defined by two components, parallel and perpendicular to the plane of incidence. These components are called s and p polarizations. "p" stands for parallel and "s" stands for senkrecht, the German word for perpendicular.*

The quantities measured by an ellipsometer are the ellipsometric angles Ψ and Δ. These angles are related to the complex ratio of the Fresnel reflection coefficients R^{p} and R^{s} for p and s polarized light with respect to the plane of incidence

$$\rho = \frac{R^{\mathrm{p}}}{R^{\mathrm{s}}} = \tan\Psi \exp i\Delta \tag{3.2}$$

The two complex reflectances R^{p} and R^{s}, describe the influence of the sample on the electric field components. Therefore, the optical properties of the sample can be determined if the properties of both incident and reflected waves are known. The complex reflectance ratio ρ is completely determined by the amplitude ($\tan\Psi$) and phase (Δ). The differential changes in amplitude and phase are related to the transformation of the shape and orientation of the ellipse of polarization.

In many applications, the ellipsometric technique can be used to determine:

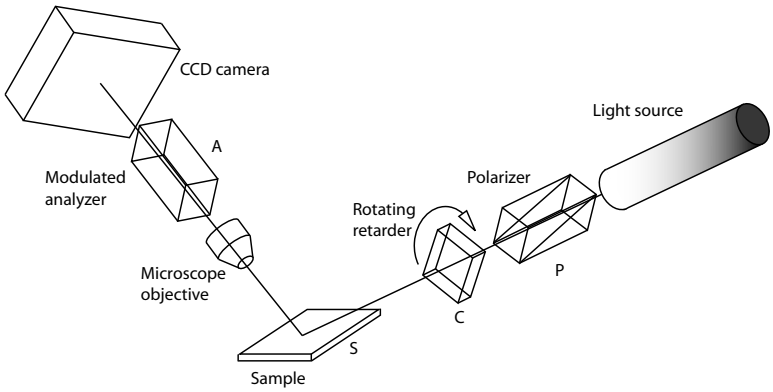

Figure 3.6: The ellipsometric Polariser, Compensator, Sample, Analyser (P,C,S,A) configuration. Images are recorded continuously with a sensitive high–resolution digital CCD camera over one or more revolutions of the retarder, and images with ellipsometric contrast are calculated by a fast computer.

- the optical properties of bulk materials and thin films. The investigated materials may be in the liquid or solid phase, optically isotropic or anisotropic;

- surface phenomena involving the growth of thin films starting from a submonolayer up to their final thickness. Examples are oxidation, deposition, adsorption, etc. Ellipsometry can be also used as a monitoring tool for the removal of coatings such as desorption, plasma etching, sputtering, etc.;

- physical factors that affect the optical properties such as composition, stress or temperature.

In our case, a single wavelength (λ=532 nm) EP^3 imaging ellipsometer from Nanofilm, Germany, was used.

Null and Imaging Ellipsometry

The imaging ellipsometer we used to characterize our samples, was a combination of classical null ellipsometry and real-time microscopy. After passing through a linear polarizer (P) and a quarter–wave plate, also named compensator (C), the laser beam is elliptically polarized. A schematic drawing of the device is represented in Fig.(3.6).

The elliptically polarized light is reflected by the sample (S) into the analyzer (A) and is imaged by a CCD camera through a long working distance objective. In this PCSA configuration, the orientation of the P and C angles is chosen in such a way, that the initially elliptically polarized light becomes linearly polarized upon reflection from the sample. The ellipsometric null condition is obtained when the light at the CCD camera is zero (i.e. for a 90° angle between the plane of polarization of the reflected light and A). The P, C, and A angles at the null condition are related to the optical properties of the sample. A comparison of the measured data with computed models, leads to a deduction of the film thickness and the complex refractive index of the film.

Bibliography

[1] G.T. Dee, B.B. Sauer; *J. Colloid Int. Sci.* **152**, 1992

[2] G.T. Dee, B.B. Sauer; *Polymer* **36**, 1995

[3] B.B. Sauer, N.V. Dipaolo; *J. Colloid Int. Sci.* **144**, 1991

[4] B.B. Sauer, G.T. Dee; *J. Colloid Int. Sci.* **162**, 1994

[5] D.G. LeGrand, G.L. Gaines, Jr.; *J. Colloid Int. Sci.* **42**, 1973

[6] S. Wu; *J. Phys. Chem.* **74**, 1970

[7] R. Sherman, D. Hirt, R.J. Vane; *J. Vac. Sci. Technol.* **12**, 1994

[8] C. Extrand; *Poly. Eng. Sci.* **34**, 1994

[9] B.K. Daniels; Advances in Resist Technology and Processing III, Proc. SPIE **631**, 1986.

[10] E.M. Slayter and H.S. Slayter, *Light and Electron Microscopy*, Cambridge University Press, 1992.

[11] S. Bradbury and B. Bracegirdle, *Introduction to Light Microscopy*, Oxford, UK, New York, Bios Scientific Publishers; Springer, 1998.

[12] Olympus Microscopy Resource Center:
http://www.olympusmicro.com/primer/

[13] G. Binning, C.F. Quate, C. Gerber; *Phys. Ref. Lett.* **56**, 1986

[14] P. H. Osanna; *Meas. Sci. Rev* **1**, Nr. 1, 2001.

[15] R. D. Piner, C.A. Mirkin; *Langmuir* **13**, 1997

[16] H.-U. Krotil; *Interface Analysis* **27**, 1999

[17] X. Chen; *Ultramicroscopy* **75**, 1998

[18] S.N. Magonov, J. Clevelanda, V. Elingsa, D. Denleyb, M.-H. Whangboc; *Surface Science* **389**, 1997

[19] L. Zitzler, S. Herminghaus, F. Mugele; *Phys. Rev. B* **66**, 2002

[20] M. S. Marcus, R. W. Carpick, D. Y. Sasaki, M. A. Eriksson; *Phys. Rev. Lett* **88**, 2002

[21] H. G. Tompkins, *A User's Guide to Ellipsometry*, Academic Press, New York, 1993.

[22] R. M. A. Azzam and N. M. Bashara, *Ellipsometry and Polarized Light*, North Holland, Amsterdam, 1977, 1988.

[23] Beaghole Instruments; http://www.beaglehole.com/elli_intro/elli_intro.html

[24] Nanofilm Surface Analysis; http://www.nanofilm.de

Chapter 4

Antireflection Coatings Made by a Sol–Gel Process

4.1 Introduction

Light reflections from computer monitors, car dashboards and TV screens impair the legibility of the displays by degrading the transmission of optical components. The decrease in transmission of a transparent optical medium is caused by the abrupt change in the refractive index at the interface between a medium and its environment. Antireflection (AR) coatings reduce the reflection considerably improving the quality of optical lens systems.

The first ever AR coating was presumably made by Fraunhofer in 1817. He etched glass in a concentrated atmosphere of sulphuric and nitric acid vapors. As a result of the etching process he noted that the reflection was strongly reduced [1]. In 1896 the optical manufacturer D. Taylor stated in an article [2] "... we are very glad to be able to reassure the owner of such a flint (glass) that this film of tarnish generally looked upon with suspicion, is really a very good friend to the (telescope) observer, inasmuch as it increases the transparency of

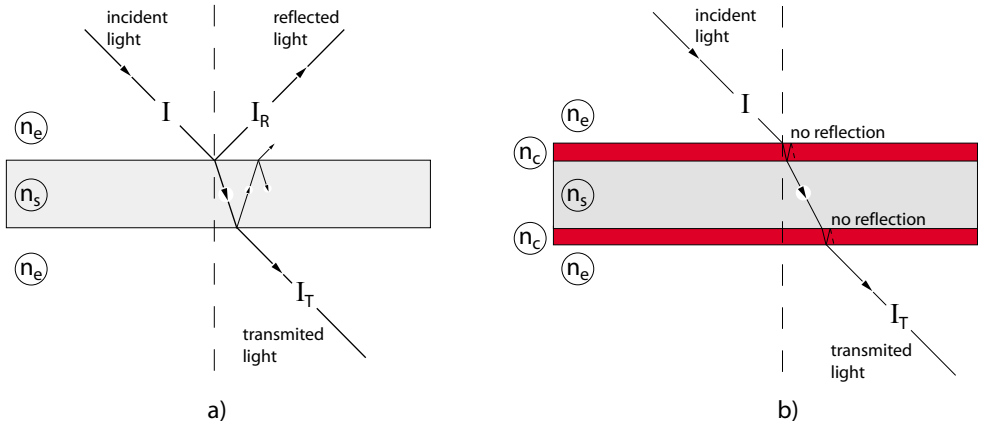

Figure 4.1: Reflection and refraction of a plane wave. a) When a plane wave of intensity I, falls onto a boundary between two homogeneous media of different optical properties, it splits into two waves: a reflected wave I_R and a transmitted one $I_T \approx I\text{-}I_R < I$. b) Propagation of light through an AR coated substrate. The reflected light is minimized when the reflected beams from the air–coating and coating–substrate interfaces interfere destructively. In this case $I_T \approx I$.

his objective". Taylor developed further this chemical etching process to form tarnished films. Today, these are called antireflection coatings. A modern optical system (telescope, microscope or binoculars) would not work without AR coatings. The image would become blurred due to the reflections in the various lenses [3].

In spite of intensive research, the availability of broadband antireflection coatings is still limited by lack of materials with low refractive indices. The work presented in this chapter describes a new method of producing nanoporous hard AR coatings with improved optical transmission.

4.2 Principle of AR Coatings

The reflection loss of an optical surface is related to the difference between the refractive indices of environment and the optical material. The theory explaining the optical behavior of single and multiple homogeneous coatings

is well understood [4, 5]. For good antireflection properties, a coating must satisfy two conditions that lead to complete destructive interference (Fig. 4.1):

1. *The Phase Condition:* For the destructive interference of the reflected beams, the length of the optical path in the layer has to be equal to one half of the light wavelength. This quarter–wave condition gives the ideal thickness of the coating:

$$\lambda_0 = 4n_c \cdot h_c \tag{4.1}$$

   where λ_0 is the wavelength at which destructive interference occurs.

2. *The amplitude condition:* For complete destructive interference, the amplitudes of light reflected from the coating–air and substrate–coating interfaces have to be equal. This condition is satisfied when the refractive indexes of the coating (n_c), the environment (n_e) and the substrate (n_s) are given by the following relation:

$$n_c = \sqrt{n_e n_s} \tag{4.2}$$

   If air is the environment ($n_e = 1$) then $n_c = \sqrt{n_s}$.

The reflection from a coated surface is given by Fresnel's equation

$$R_m = \left(\frac{n_c^2 - n_e n_s}{n_c^2 + n_e n_s} \right)^2 \tag{4.3}$$

When the surface is coated with a film of refractive index (n_c) that varies continuously from n_s to unity and thickness larger than the reference wavelength, zero reflectance is obtained for the reference wavelength. The principle of inhomogeneous AR coatings is depicted in Fig.(4.2). There are two approaches to produce graded refractive index coatings. One is to pattern the substrate surface with a subwavelength periodic structure (Fig. 4.2a) and the second is to use a nanoporous coating (Fig. 4.2b).

The two approaches differ only in the smooth variation of the optical constants throughout the thickness. In the first case (Fig. 4.2a), the refractive index of the inhomogeneous layer decreases gradually from n_s to unity. Therefore, to produce such a coating, a material with the same refractive index as

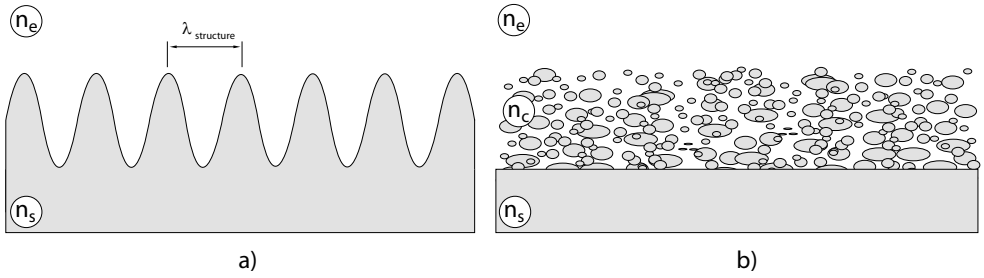

Figure 4.2: Two approaches of using inhomogeneous layers as antireflection coatings. a) The "moth–eye" type of AR coating introduces a smooth transition between the optical properties of environment and substrate. b) The nanoporous type of AR coating. The refractive index of the coating depends by its porosity and is the average between the refractive index of the pores and the matrix.

the substrate has to be used. The optical properties of such a sub–wavelength structured surface are explained by considering that the surface structure acts as a periodic diffraction grating. If the period of the grating ($\lambda_{\text{structure}}$) is small compared to the wavelength of light, only the zero–order diffracted wave propagates and higher diffraction orders are suppressed [6, 7]. However, with increasing the angle of incidence, it is more difficult to avoid higher–order diffracted waves propagating into the substrate.

The optical properties of the nanoporous layer (Fig. 4.2b) can be described using a different model [8, 9, 10]. The refractive index of a material is related to its density. By introducing porosity, the material density decreases, resulting in a smaller refractive index. To prevent scattering two conditions have to be met: the pore sizes have to be much smaller than the wavelength of light and the pore distribution has to be homogeneous. The relation between the density and the refractive index of such porous materials is [8]

$$\frac{n_p^2 - 1}{n_c^2 - 1} = \frac{d_p}{d_c} \tag{4.4}$$

where n_p and d_p are the refractive index and the density of the porous material and n_c and d_c are the refractive index and the density of the solid material.

Eqn.(4.4) is written in terms of porosity as

$$\frac{n_p^2 - 1}{n_c^2 - 1} = 1 - \frac{P}{100} \tag{4.5}$$

or

$$n_p^2 = (n_c^2 - 1)\left(1 - \frac{P}{100}\right) + 1 \tag{4.6}$$

where P is the percentage of porosity. When $P = 0\,\%$ (no pores), $n_p = n_c$. When $P = 100\,\%$ (no solid material), $n_p = 1$.

4.3 Experimental method

The refractive indices of glass and transparent plastic substrates are typically $n_s \approx 1.5$. From Eqn.(4.2), the optimal refractive index for a single–layer broad–band AR coating is

$$n_f = \sqrt{n_s} \approx 1.22$$

The lowest refractive indices for dielectrics are on the order of 1.35 (CaF_2, MgF_2). A value of $n_f = 1.22$ is therefore unreachable for conventional single layer AR coatings.

Instead of a homogeneous layer, Walheim et al. [11] used a nanoporous film. When the pore size is much smaller than the visible wavelengths, the effective refractive index of the nanoporous medium is given by Eqn.(4.6). To lower the refractive index to ~ 1.23 using a material with a refractive index of ~ 1.5, a porosity of $\sim 60\,\%$ has to be introduced. The technique used by Walheim et al. was based on the demixing of a binary polymer blend during spin–coating. The process is schematically described in Fig.(4.3). Standard polymers such as polystyrene and poly(methyl methacrylate) and solvents were used.

During the phase separation process, one of the polymer components forms domains in the matrix of the other. The development of the lateral phase morphology depends strongly on several preparation parameters. Immediately after deposition (Fig. 4.3c), the film appeared transparent and featureless due to similar values of the refractive index of polymers and substrates. To create a porous film, one of the two polymers was removed by exposing the film to a selective solvent (Fig. 4.3e). Two cases were distinguished:

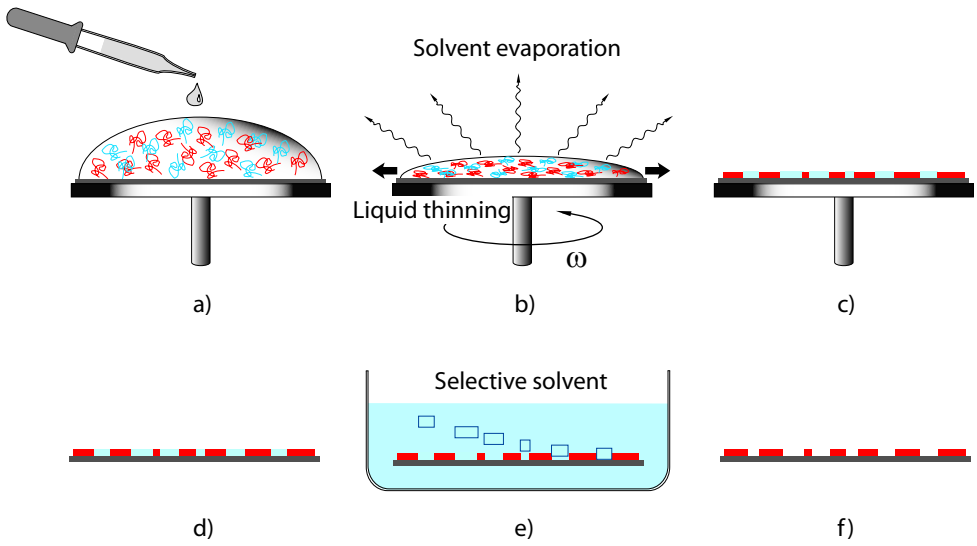

Figure 4.3: Preparation of a nanoporous coating. a) The solution consisting of two polymers in a common solvent is placed onto the substrate. During spin–coating b), phase separation sets in, and after evaporation of the solvent a lateral phase morphology is obtained c). The film is exposed to a solvent e) that is selective for one of the polymers, producing a porous film f).

i) if the pore sizes were comparable to the light wavelength, the coating appeared opaque. The phenomenon is due to light scattering by the pores.

ii) when the pore sizes were much smaller than all optical wavelengths, the film remained transparent.

The obtained nanoporous film had remarkable antireflection properties, strongly reducing the amount of reflected light.

A limitation for the aplicability of this simple and elegant method on industrial scale was the lack of wear resistance of the polymer–based AR layers. To overcome this disadvantage, we developed a new method based on a sol–gel approach. This method allowed us to produce high–quality, broad–band AR coatings with improved mechanical properties. Applying our concept

to organic–inorganic hybrid materials enabled us to replicate the nanoporous polymer films into silica mineralized AR coatings. The new sol–gel derived nanoporous silica films had broad–band antireflective properties.

4.3.1 Novel Routes for the Preparation of Mineralized AR Coatings.

We developed two methods for obtaining porous sol–gel coatings. Both techniques produced broad–band, high–quality AR coatings.

Water Based Process to Manufacture AR Coatings

This experimental procedure is based on water soluble components, therefore being a 100 % environmental friendly technique. We produced a SiO_x solid network starting with the precursor "Natron Water Glass" ($Na_2Si_3O_7$). The structure of the SiO_x network was formed by controlling the condensation of small primary silica particles (polymeric or colloidal) with a diameter of a few nanometers.

These particles are dispersed in a liquid, forming a so–called *sol*. Increasing the particle number and sizes increases the density of the sol. Eventually, the particles start to touch each–other, forming a sponge–like three–dimensional network, called *gel*.

In our approach we stopped the process in the sol state. This way, we were able to spin–coat the solution. To form the sol, acetic acid was added to an aqueous solution of sodium silicate (water glass):

$$Na_2SiO_3 + CH_3COOH \xrightarrow{H_2O} [SiO_2 \times_{(n)} H_2O] + 2Na^{\oplus}COOH^{\ominus} \tag{4.7}$$

The chemical reactions during the sol–gel process are described by three equations [12]:

$$\begin{aligned} &-Si-OR + H_2O \xrightarrow{\text{acid or base}} -Si-OH + ROH \\ &-Si-OH + HO-Si- \longrightarrow -Si-O-Si + H_2O \\ &-Si-OR + HO-Si- \longrightarrow -Si-O-Si + ROH \end{aligned} \tag{4.8}$$

The first equation in Eqns.(4.8) defines the hydrolysis process, while the other two define the condensation process. Both processes are strongly influenced by

the concentration of the components, the nature of solvent, the temperature and the pH of the solution. In our method, due to the acidic conditions (pH: 2–5) hydrolysis was favored. A large number of monomers and small oligomers with reactive Si–OH groups were formed. These molecules reacted with each–other forming the sol solution.

Adding an organic polymer to the sol solution, resulted in a phase separation between the inorganic and the organic phases when evaporating the solvent. The subsequent removal of the organic phase resulted in a porous silica film. We were able to obtain a pore size of $\sim 50\,\text{nm}$ in diameter by varying the amount of the polymer and the sol particles.

Our method consisted of 4 steps:

Step1: Preparing the solution. Solutions of 10 % $Na_2Si_3O_7$ and 10 % polyacrylamide (PAA) (by weight) in water, were made. Subsequently, the solutions were mixed in a weight ratio of 5:1.

Step2: Adding the acid. $40\,\mu\text{l}$ of acetic acid (CH_3COOH) was added to the solution. The mixture was stirred for ~ 20 seconds at room temperature.

Step3: Coating the substrate. White glass slides with a refractive index of ≈ 1.5 were coated on both sides by spin–coating at 5000 RPM.

Step4: Removing the organic component. The PAA polymer was removed by washing the sample in water for ≈ 60 seconds. A longer washing time did not produce samples with different spectral properties. The sample was subsequently dried at room temperature in a nitrogen jet.

AR coatings prepared from TMOS precursors.

A second method to prepare hard AR coatings made use of tetramethoxysilane $Si(OCH_3)_4$ alkoxide as precursor and poly(methyl methacrylate) (PMMA) as organic component. We prepared the sol phase by polymerizing tetramethoxysilane (TMOS) monomers in an acidic environment, using hydrochloric acid (HCl) as catalyst. Hydrolysis and polycondensation reactions occured when water and catalyst were added to the precursor [12, 13, 14, 15, 16, 17, 18]. The hydrolysis reaction is:

$$Si(OCH_3)_4 + H_2O \xrightarrow{HCl} [SiO_2 \cdot H_2O/CH_3OH] \tag{4.9}$$

The condensation reactions are:

(alcoxolation)
$(OCH_3)_3$–Si–OH+HO–Si–$(OCH_3)_3 \longrightarrow (CH_3O)_3$–Si–O–Si–$(OCH_3)_3$+$CH_3OH$

(oxolation)
$(CH_3O)_3$–Si–OH+HO–Si–$(OCH_3)_3 \longrightarrow (CH_3O)_{x-1}$–Si–O–Si–$(OCH_3)_3$+$H_2O$

The two chemical processes take place simultaneously in the sol–gel process. The sol solution was subsequently mixed with a PMMA solution and spin–coated onto the substrate. After removing the PMMA, a porous layer with high–quality AR properties was obtained. The three step method of preparing the coating is:

Step1: Preparing the solution. The TMOS precursor was mixed with a diluted hydrochloric acid solution in a weight ratio of 6 : 2.3. The diluted HCl solution was obtained by mixing 0.02 ml of hydrochloric acid (fuming) with 10 ml deionized water. Tetrahydrofuran (THF) was added to the aqueous TMOS solution in a weight ratio of 3:1. This solution was subsequently mixed in a weight ratio of 1:1 with a 3 % solution of PMMA in THF. The final solution was diluted 1:1 by weight with THF.

Step2: Coating the substrate. White glass slides with a refractive index of ≈ 1.5 were coated both sides by spin–coating at 2000 RPM.

Step3: Removing the organic component. The PMMA was removed by washing the sample in acetone for ≈ 60 seconds. A longer washing time did not produce samples with different spectral properties. The sample was subsequently dried at room temperature in a nitrogen jet.

For both $Na_2Si_3O_7$ and TMOS based preparation methods, the resulting porous silica layers (Fig. 4.3f) increased the optical transmission through the glass substrates in the visible wavelength range to $T \approx 99\%$. For the reference wavelength of $\lambda = 600$ nm, a transmission of $\approx 99.8\%$ was achieved. We adjusted the thickness of the layer by varying the rotation speed in the coating process. The optical transmission spectra of a glass slide coated on both sides with a 120 nm porous silica coating is shown in Fig.(4.3.1) (circles). By increasing or decreasing the thickness, the maximum of the transmission

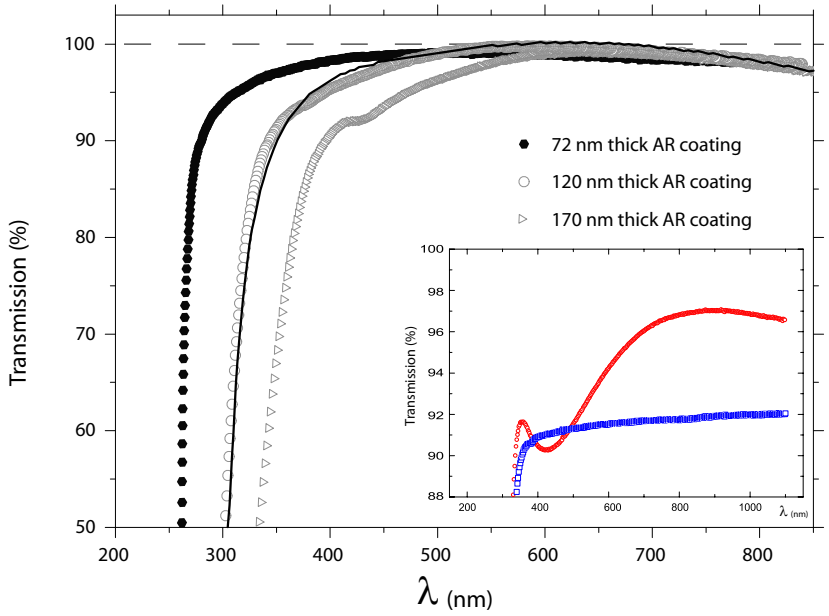

Figure 4.4: Transmission curve of a glass slide coated on both sides with a 72 nm (black hexagons), 120 nm (open circles) and 170 nm triangles thick porous silica layer. The solid curve is the theoretical fit to the experimental data (open circles) yielding a refractive index $n_c = 1.289 \pm 0.05$. *The inset show for comparison the transmission curves of an uncoated (squares) and* MgF_2 *coated (circles) glass slide.*

curve shifts to higher or lower frequencies, respectively. The solid line is a fit to the data yielding an effective value of $n_c = 1.289 \pm 0.05$. The ($\lambda = 532\,\text{nm}$) refraction index of the coating measured by ellipsometry was 1.302 ± 0.02. The calculated porosity was $\sim 57\,\%$. A visual inspection of a AR coated glass slide, showed that the AR properties of the coating doesn't seem to change with the angle of incidence.

The advantage of the TMOS based technique compared to the $Na_2Si_3O_7$ coating is a better applicability on an industrial scale. The $Na_2Si_3O_7$ coating solution in water was very unstable due to the short time needed for gelation process to take place. The sol solution turned into a gel in less than 30

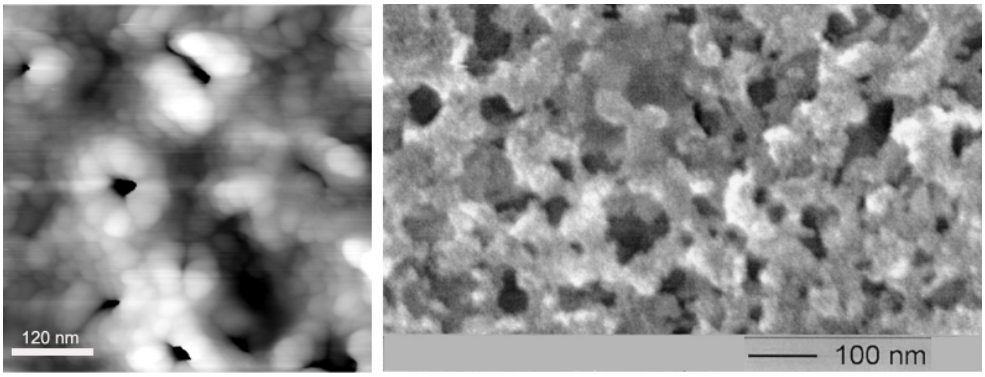

Figure 4.5: a) AFM and b) SEM micrographs of an antireflection coating.

seconds, leaving only little time for spin–coating. However, the reaction could be somewhat stabilized by changing the amount and the nature of the acid. In comparison, the TMOS based coating solution was stable for ~ 3 hours at room temperature. At lower temperatures ($\sim 4^\circ$ C) the stability of the solution increased to 3–4 days.

Porous films were obtained by the subsequent removal of the inorganic phase. In Fig.(4.5), Tapping–AFM and SEM images of the nanoporous layers are shown. In the case of AFM imaging, the resolution is limited by the radius of the tip curvature. The images are therefore a convolution of the surface topography with the tip shape. This tip artefact is visible in Fig.(4.5a). SEM images helped to visualize the unconvoluted pores (Fig. 4.5b) and the cross–sectional SEM micrographs (Fig. 4.6) revealed a homogeneous distribution of the pores inside the coating.

4.3.2 AR Coatings on Plastic Substrates

The substrates used in Section 4.3 were white glass slides with a refractive index of ≈ 1.5 (λ=532 nm). However, plastics have become important materials during the past decades, due to their high processability, light weight and low cost. They are used for ophthalmic lenses, sunglasses, displays, etc. Poly(methyl methacrylate) (PMMA) and poly(carbonate) (PC) are some of

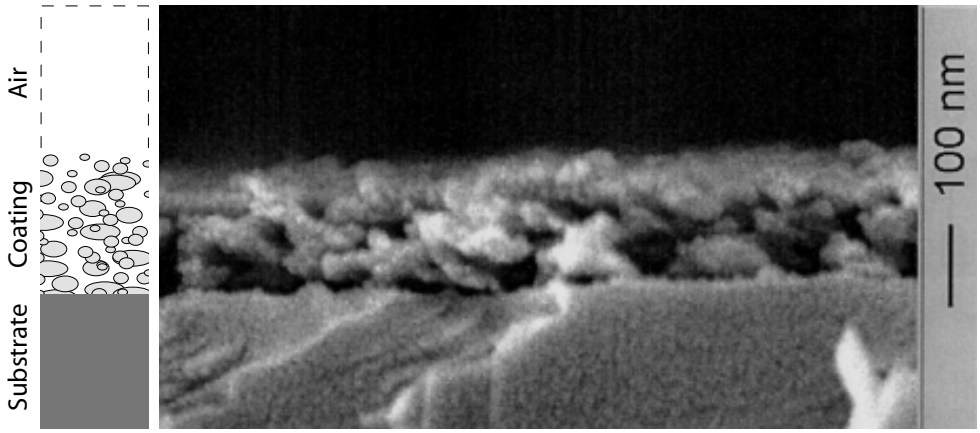

Figure 4.6: Cross section through the AR coating. Notice the homogeneous distribution of the pores inside the coating.

the most common polymers used for optical applications on an industrial scale. The progress in vacuum technology and the development of high yield sputtering systems made it possible to deposit metal and dielectric layers onto plastic substrates [19, 20, 21, 22]. However, sputtering techniques pose a number of physical and engineering problems such as adhesion and reproducibility.

In general, the adhesion of inorganic layers to organic substrates is very poor. The lack of adhesion is due to the big difference in the surface energies and mechanical properties of the organic and inorganic phases. In the absence of chemical bonding, the adhesion is due to van der Waals forces only. Once deposited, the inorganic film is prone to rupture because of the difference in expansion coefficients between the coating and plastic substrates. Depositing an inorganic coating onto untreated PMMA or PC often results in a non–adhering layer that cracks due to thermal expansion, or in a fragile surface that is easily scratched. To qualitatively measure the adhesion between the AR coating and the substrate, we rubbing the sample with a hard cloth. Even after minutes of hard rubbing, the AR coating deposited on glass substrates didn't presented signs of delamination. However, on plastic substrates, the adhesion strength was diminished.

A new method called liquid phase deposition (LPD) was recently developed

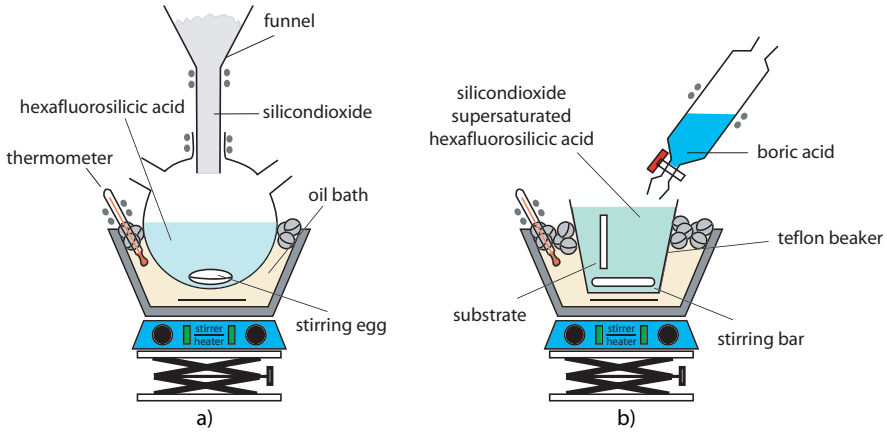

Figure 4.7: The experimental setup used a) to saturate the initial hexafluorosilicic acid and b) to coat the plastic substrates.

to deposit homogeneous SiO_x layers onto plastic substrates [23, 24, 25, 26]. We used this method to improve the adhesion of silica–based nanoporous coatings to PMMA and PC substrates. A homogeneous SiO_x film that is grown on the substrate, acts as an anchoring layer for the porous AR coating. Because the film has a similar refractive index as PMMA and PC ($\cong 1.5$), it has only a small influence on the optical properties of the coated surface.

The LPD method was developed by Nagayama et al. [23]. The advantage of the method is that it does not require expensive equipment and the deposition is performed at room temperature producing dense and homogeneous SiO_x layers. The process involves the deposition and growth of a silica layer by immersing the substrate in an aqueous solution of hexafluorosilicic acid (H_2SiF_6) that is supersaturated with silica.

The silica saturation was obtained by dissolving a large quantity of fumed silica in the aqueous hexafluorosilicic acid solution (Fig. 4.7a). The plastic substrate was than immersed in the saturated solution and boric acid (H_3BO_3) was added to induce the supersaturation of the solution with silicon oxide (Fig. 4.7b). The chemical reactions responsible for the growth of the SiO_x layer are

$$H_2SiF_6 + 2H_2O \rightleftharpoons 6HF + SiO_2 \tag{4.10}$$

$$H_3BO_3 + 4HF \rightleftharpoons 6BF_4^{\ominus} + H_3O^{\oplus} + 2H_2O \tag{4.11}$$

Chou et al. [26] proposed an alternative explanation of the deposition process. Instead of Eqn.(4.10), they stated that the growth of SiO_x film was dictated by the creation of intermediate $SiF_m(OH)_{4-m}$ with $m < 4$. The corresponding reaction is:

$$H_2SiF_6 + (4-m) \cdot H_2O \rightleftharpoons SiF_m(OH)_{4-m} + (6-m) \cdot HF \tag{4.12}$$

When adding the boric acid, the HF is consumed and the intermediate $SiF_m(OH)_{4-m}$ is created. The chemical reaction that describes this process is:

$$SiO_2 : xH_2O + m \cdot HF \rightleftharpoons SiF_m(OH)_{4-m} + (x+m-2) \cdot H_2O \tag{4.13}$$

The intermediate $SiF_m(OH)_{4-m}$ reacts either with the substrate to form silicon dioxide or with other $SiF_m(OH)_{4-m}$ molecules to form a silica powder. The additional reactions of these molecules with the substrate are:

$$Si - F_{substrate} + Si - OH_{solution} \rightleftharpoons Si - O - Si_{substrate} + HF_{solution}$$
$$Si - OH_{substrate} + Si - F_{solution} \rightleftharpoons Si - O - Si_{substrate} + HF_{solution}$$

A schematic diagram illustrating the two routes to deposit SiO_x layers on plastic substrates using the LDP method is depicted in Fig.(4.8)

The concentration of boric acid is much smaller than that of H_2SiF_6. As a consequence, only a small part of H_2SiF_6 is transformed in the intermediate compound. Increasing the concentration of H_3BO_3 leads to a higher concentration of $SiF_m(OH)_{4-m}$ in the solution and a larger deposition rate. However, the disadvantage of increasing the deposition rate is a less dense and less homogeneous SiO_x layer.

In our case, 800 ml pure hexafluorosilicic acid (34 %, 2.47 mol/l) was diluted with 200 ml water. The solution was than heated to 40° C and 30 g of silicon dioxide powder was added to saturate it. The mixture was stirred for 10 hours at 40 ° C and then filtered by centrifugation at 50.000 RPM.

The PMMA/PC substrates, were ultrasonically cleaned in a bath of ethanol and deionized water. Subsequently, the substrates were immersed in the coating solution at a temperature of 30° C. 0.2 mol/l solution of boric acid was

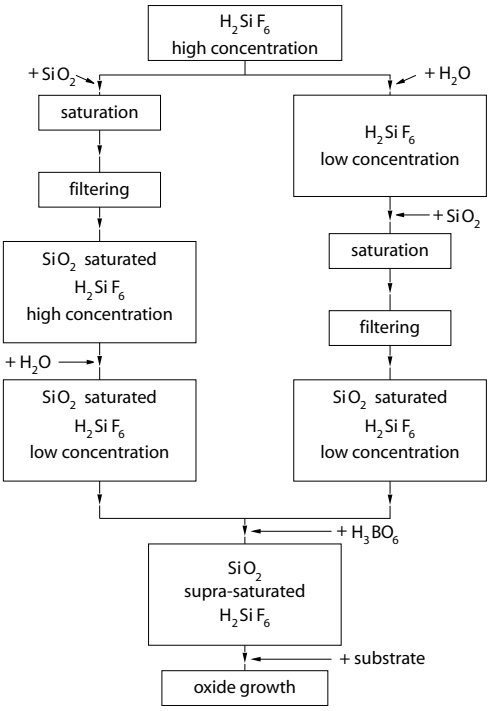

Figure 4.8: The schematic diagram illustrating the two routes to deposit SiO_x layers on plastic substrates using the LDP method.

added in 5 consecutive batches of 1 ml each. After 5 h, the sample was taken out of the coating solution and rinsed with deionized water. The quality of the coating was tested by measuring the water contact angle on the substrate before and after deposition. The uncoated plastic substrate had a contact angle of $\approx 35^\circ$. The contact angle was close to zero for homogeneously coated plastic surfaces. The thickness of the deposited SiO_x layer was $\cong 10$ nm, as measured by ellipsometry.

The SiO_x film produced by LPD increased greatly the adhesion between the AR coating and the plastic substrate. By rubbing the sample with a hard cloth, the layer presented the same stability as the ones deposited on glass substrates. In addition, the film protected the substrates against the chemical

attack of the solvents in the AR coating solution.

In conclusion, the LPD technique proved to be an easy and straightforward method for coating plastic samples with an intermediary SiO_x layer prior to deposition of AR coatings. The oxide homogeneity and thickness was found to depend on several factors such as deposition time, boric acid concentration, and temperature. By adjusting all these parameters, we were able to produce homogeneous 10 nm thick oxide films with a strong anchoring effect for the subsequently deposited antireflection coatings.

4.3.3 Improving the Cleanability of Porous AR Coatings

Adam and Wenzel [27] and Cassie and Baxter [28] showed that the apparent contact angle of a liquid droplet on the surface is correlated with the roughness of the surface. They demonstrated that water is repelled from rough, hydrophobic surfaces and water drops readily roll off. To be self–cleanable a surface has to fulfill two requirements:

- the water contact angle has to be higher than 170°
- the contact angle hysteresis must be small

The average roughness R_a of a surface is defined as the arithmetic average of the absolute values of the surface height deviations measured from a the mean plane. R_a is given by

$$R_a = \frac{1}{N}\sum_{i=1}^{N}|z_i - \bar{Z}| \tag{4.14}$$

with

$$\bar{Z} = \frac{1}{N}\sum_{i=1}^{N} z_i \tag{4.15}$$

where i is the number of measurements and N is the number of data points.

The porous silica AR coatings produced by both methods described in Section 4.3.1, had a roughness of $\approx 1.6\,\text{nm}$, as measured by AFM. Due to their high surface energy, the effect of the roughness is to decrease the water contact angle. To increase the water contact angle,

3-Heptafluoroisopropoxypropyltrimethoxysilane (HFIPP-tMOS)

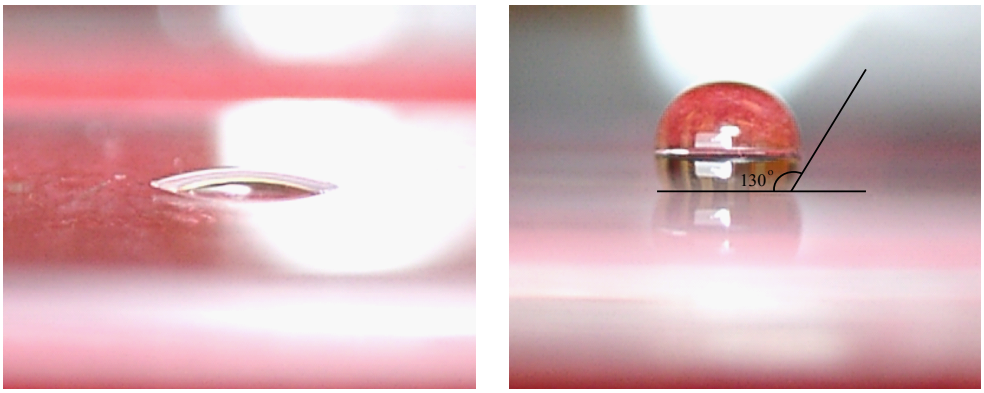

Figure 4.9: Measured contact angle before a) and after b) improving the cleaning properties.

was added to the TMOS precursor in a weight ratio of 1:20, before the acid addition.

Due to the methoxy groups, the new component hydrolyzes and condenses in the same manner as TMOS. After completing the reactions, the sol solution contained particles that were partly fluorinated. The AR coating morphology was dictated by the free energy of the system during the spin–coating process. The fluorinated part with low surface energy preferred the air–film interface while the unfluorinated sols preferred the substrate. This way, by exposing the fluorinated parts to the air surface, the measured contact angle increased from 7° to 130° (Fig. 4.9). The value of the contact angle was still to low for the surface to have self-cleaning properties. The combination of a low energy surface and high roughness led, however, to improved cleaning properties of the AR film. A finger print could easily be washed off by a mixture of water and ethanol (3:1 by weight).

4.4 Conclusions

The work in this chapter describes a new method of producing low cost, broad–band antireflection coatings. Our approach made use of a simple prin-

ciple – the demixing process between an organic phase (PAA/PMMA) and an inorganic phase (silicon dioxide sols). The resulting AR coatings were easily fine–tuned to produce a wide range of refractive indices. The sizes and density of the pores were varied by varying the molecular weight and the amount of the polymeric phase. The thickness of the layer was adjusted by varying the spin–coating speed. In this manner, the light transmission at selected wavelengths was enhanced. The optical properties of the mineral nanoporous AR coating proved to be superior to the standard MgF_2 coatings. The light transmitted through a coated surface varied only little with the incident angle. The coatings had good mechanical stability on glass, strong adhesion to plastic substrates and improved cleanability.

Bibliography

[1] J. Fraunhofer; *Joseph von Fraunhofer Gesannekte Schriften*, Munich, Germany 1888

[2] H.D. Taylor; *The Adjustment and Testing of Telescopes Objectives*, York, England, 1896

[3] P. Nostell; *Ph.D. Thesis at Uppsala University* 2000

[4] M. Born, E. Wolf; *Principles of Optics*, Pergamon Press, 1964

[5] O.S. Heavens; *Optical Properties of Thin Solid Films*, Dover Publications Inc., New York, 1991

[6] A. Gombert, W. Glaubitt, K. Rose, J. Dreibholz, B. Bläsi, A. Heinzel, D. Sporn, W. Döll, V. Wittwer; *Thin Solid Films* **351**, 1999

[7] D. Chen; *Sol. En. Mat. Sol. Cells* **68**, 2001

[8] B.E. Yoldas, T.W. O'Keeffe; *Appl. Opt.* **18**, 1979

[9] P. Menna, G. Di Francia, V. La Ferrara; *Sol. En. Mat. Sol. Cells* **37**, 1995

[10] T.V. Semikina, A.N. Shmyryeva; *Renewwable En.* **15**, 1998

[11] S. Walheim, E. Schäffer, J. Mlynek, U. Steiner; *Science* **283**, 1999

[12] N. Hüsing, U. Schubert; *Angew. Chem. Int. Ed.* **37**, 1998

[13] G.M. Pakonk, E. Elaloui, P. Achard, B. Chevalier, J.L. Chevalier, M. Durant; *J. Non-Crys. Sol.* **186**, 1995

[14] F. Ehrburger–Dolle, J. Dallamano, E. Elaloui, G. Pajonk; *J. Non-Crys. Sol.* **186**, 1995

[15] A. Borne, B. Chevalier, J.L. Chevalier, D. Quenard, E. Elaloui, J. Lambard; *J. Non-Crys. Sol.* **188**, 1995

[16] G. Wu, J. Wang, J. Shen, T. Yang, Q. Zhang, F. Zhang; *Mat. Sci. Eng.* **B78**, 2000

[17] B. Wang, G. Wilkes, J.C. Hendrick, S.C. Liptak, J.E. McGrath; *Macromolecules* **24**, 1991

[18] S. Hæreid, M. Dahle, S. Lima, M. Einarsrud; *J. Non-Crys. Sol.* **186**, 1995

[19] J.S. Chapin; *Vaccum Technol. Jpn.* **37**, 1974

[20] J.S. Chapin; *US Patent 4.166.018 Airco, Inc.* 1979

[21] J.J. Cuomo, F.R. Kaufman, S.M. Stephen; *US Patent 4.588.490 Int. Business Machines Corp.* 1986

[22] S. Hæreid, M. Dahle, S. Lima, M. Einarsrud; *US Patent 5.346.600 Hughes Aircraft Comp.* 1994

[23] H. Kawahara, T. Goda, H. Nagayama, H. Honda, A. Hishinuma; *SPIE* **1128**, 1989

[24] A. Hishinuma, T. Goda, M. Kitaoka, S. Hayashi, H. Kawahara; *Appl. Surf. Sci.* **48/49**, 1991

[25] H. Kawahara, Y. Sakai, T. Goda, A. Hishimura, K. Takemura; *SPIE* **1513**, 1991

[26] J.S. Chou, S.C. Lee; *J. Electrochem. Soc.* **141**, 1994

[27] R.N. Wenzel; *Ind. Eng. Chem.* **28**, 1936; *J. Phys. Colloid Chem.* **53**, 1949

[28] A.B.D. Cassie, S. Baxter; *Trans. Faraday Soc.* **40**, 1944

Chapter 5

Capillary Instabilities by Thermal Fluctuations

5.1 Introduction

The study of capillary instabilities and their causes goes back more than one century [1]. Several [2, 3, 4] authors explained the spontaneous destabilization of thin films on the basis of a disjoining pressure caused by dispersive van der Waals forces. Due to the formal similarity between capillary surface instabilities and the model developed by Cahn [5] to describe the phase separation by spinodal decomposition of binary mixtures, the spontaneous destabilization of thin films was called "spinodal dewetting" [6]. On the other hand, films thicker than 10 nm are stable against capillary fluctuations and require an externally applied potential such as electric [7, 8, 9] or magnetic fields to be destabilized.

Recently, the dewetting of thin polymer films was rediscovered. The renewed interest was partly caused by the technological importance of film stability (e.g. for coatings, lubrication layers. etc.), partly because liquid dewetting leads to a rich pattern formation process. From a fundamental point of view,

the patterns created by a capillary instability can be used to quantify the force driving the instability. However, there are several experimental complications. Because of the high viscosity of polymer melts, the dynamics of the spinodal deweting process is slow and the film often breaks–up by heterogeneous nucleation of holes [10]. A second reason for the lack of systematic dewetting studies is the seemingly obvious nature of their outcome: capillary instabilities should reflect the destabilizing nature of dispersive vdW forces predicted more than 50 years ago [2, 3, 4].

Because of these difficulties, most of the experimental studies of van der Waals driven capillary instabilities found discrepancies of various degrees. The spectrum of capillary waves is very sensitive to the forces acting at the free interface of the polymer film. Therefore, the theoretical model has to include all destabilizing effects. Apart of van der Waals forces, possible additional destabilizing potentials may arise from the presence of electric charges [11], external electric fields [7], temperature gradients [8], stresses induced by the preparation methods or capping layers [12], etc.

We regard van der Waals driven film instabilities from a somewhat unusual angle and propose a generalization that leads to a disjoining pressure caused by the confinement of thermal noise. We start by describing the relevance of the thermo–acoustic disjoining pressure for various experimental approaches. After introducing model calculations indicating the route for the experimental confirmation of this effect, we present three types of experiments that confirmed these predictions.

5.2 Fluctuation Induced Forces

Macroscopically negligible, van der Waals forces manifest themselves in the attraction and repulsion between molecules. They are responsible for the cohesion in molecular crystals, in biological systems, colloidal suspensions, etc. In practical applications, van der Waals forces may cause the collapse of submicrometer sized structures in micromechanical systems [13], or the break–up of thin film coatings [6]. van der Waals forces are rooted in the quantum theory of electrodynamics and stem from dipole–dipole, or dipole–induced dipole interactions. They act over relatively short distances proportional to the inverse of the seventh power of the intermolecular distance. van der Waals

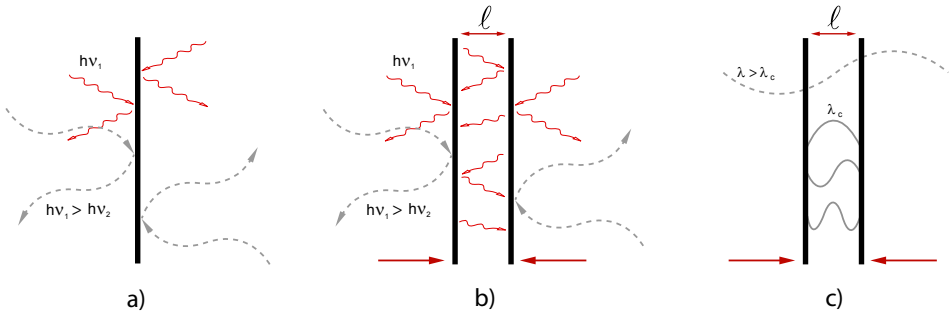

Figure 5.1: Behavior of the electromagnetic field in the presence of a confinement. The confinement is determined by two (metal) plates positioned at a small distance ℓ. a) When only one plate is introduced in the oscillatory electromagnetic field, the net radiation pressure is zero. The plate is not subjected to a net pressure because per unit of time and area, an equal number of photons hit its surface from both sides. b) Introducing a second plate at a small distance ℓ, there is a net attractive force between the two plates. c) Entropic explanation of the "Casimir Effect": the reduction of the space between the two plates and the enlargement of the unconfined external space maximizes the number of allowed electromagnetic modes.

forces can be also considered in terms of the confinement[1] of the electromagnetic fluctuation spectrum. The principle of confinement is more general than the usual argument of interacting dipole fluctuations, because analogous disjoining pressures arise also from the confinement of other fluctuating fields. Forces that arise from the confinement of a fluctuation spectra were observed in experiments involving stacks of membranes, liquid crystals, the demixing of polymer blends, etc. [14]. A particularly striking example is the strong attractive force between two ships side-by-side caused by the surface waves of water [15]. It was also shown that low–frequency acoustic waves (generated by loud–speakers) give rise to an attraction between two plates [16] placed inside the acoustic noise field. We postulate that there should be a similar, but more fundamental effect caused by thermally excited acoustic fluctuations [17].

[1]The confinement is defined by two plates (made of metal of any other material) placed a few (1 to 10) nanometers apart.

The discussion of the confinement induced forces begins with the classical *"Casimir Effect"* – the attractive force between two metal plates (Fig. 5.1) due to the confinement of electromagnetic zero-point fluctuations for small plate spacings [18]. The behavior of the fluctuating electromagnetic field in the presence of a confinement can be interpreted in two ways:

1. The first explanation regards the photons as particles. The zero–point electromagnetic fluctuation field extends over the entire frequency spectrum. Therefore, the photons have all possible energies. Introducing a single plate into the electromagnetic field (Fig. 5.1a), per unit of area and time, the same number of photons are reflected from either side of the plate. Introducing a second plate at a small distance ℓ with respect to the other surface (Fig. 5.1b), photons with energies smaller than hc/λ_c (where $\lambda_c = \ell$) are excluded from the gap. Because of the confinement, there are less photons incident onto the plates from within the gap compared to the external surfaces. The difference gives rise to an uncompensated radiation pressure and the plates experience an attractive force.

2. The second explanation is based on the electromagnetic wave theory. Due to the small distance ℓ between the plates, the modes with wavelengths larger than $\lambda_c = 2\ell$ are excluded from the gap (Fig. 5.1c). Between two conducting plates, only modes with wavelengths smaller than the plate spacing are allowed. Decreasing the gap and thereby enlarging the unconfined space lowers the overall free energy of the system and accounts for an attractive force.

To define the force that acts between two metal plates positioned at a small distance ℓ, Casimir [18] considered the difference in electromagnetic quantum fluctuations of vacuum inside and outside the plates. In the case of confinement there is a finite energy difference ΔE per plate unit area S, while for the unconfined case [14] the sum of ground state energies is infinite

$$\frac{\Delta E}{S} = -\frac{\pi^2}{720}\frac{\hbar c}{\ell^3} \tag{5.1}$$

Explained by electromagnetic wave theory, the nature of this force is purely entropic: the reduction of the space between the two plates and thereby the

enlargement of the unconfined external space maximizes the number of allowed electromagnetic modes. Generalized for arbitrary materials in the gap and the adjacent media, the above explanation leads to the theory of van der Waals forces [19].

The change in the mode spectrum of two harmonic oscillators with eigenfrequencies ω_1 and ω_2 and complex polarizabilities α_1 and α_2, brought from infinity to a distance ℓ corresponds to an energy change

$$\Delta E = -\frac{3\hbar}{2}\frac{\omega_1\omega_2}{\omega_1+\omega_2}\frac{\alpha_1\alpha_2}{\ell^6} \tag{5.2}$$

This argument assumes that the dipole fluctuation of a neutral atom induce a dipole moment in a second atom at distance ℓ. While the time–averaged dipole moments of both atoms are zero, the mean energy based on the attraction of the two instantaneous dipoles is finite, giving rise to the van der Waals force. If the atoms are an appreciable distance apart, the time needed by the electrostatic field of one instantaneous dipole to reach the neighboring atom and return may be comparable to the period of the fluctuating dipole itself [13]. Therefore, a phase shift appears between the fluctuating dipoles and the scaling of the force with distance changes. In this case, only the static atomic polarizabilities α_{10} and α_{20} are considered and the energy is given by

$$\Delta E = -\frac{23}{4\pi}\hbar c\frac{\alpha_{10}\alpha_{20}}{\ell^7} \tag{5.3}$$

To relate microscopic and macroscopic properties of the interacting media, McLachlan (1963) [20] presented a more general theory of dispersion forces – the *Susceptibility theory*. The dispersion energy between two macroscopic bodies may be computed by pairwise interaction–energy summation. In this approach, van der Waals interaction energies are assumed to be additive (similar to gravitational potentials), ignoring the influence of neighboring atoms on the interaction between any pair of atoms. Even though these effects are small [21], the problem of additivity is not trivial. The macroscopic theories avoid this complication by ignoring the atomic structure of the interacting bodies, focusing only on bulk properties, such as the dielectric constants and refractive indices. Several methods for computing the van der Waals interactions have been developed, such as density–functional theories [22, 23], local–density approximation theories [23, 24] and various generalized–gradient approximations [25, 26]. To model our experiments and determine the van der Waals inter-

action strength, we used the Tabor–Winterton (TWA) approximation based on the optical properties of the materials [27]. We applied the generalized Hamaker theory [28] to a slab of a dielectric medium ③ bounded by semi-infinite media ① and ②. This generalization leads to the well known van der Waals energy for both London and Casimir formalisms [18, 19]. Hamaker introduced the concept of the Hamaker constant, which determines the magnitude of the van der Waals forces. The interaction energy of two planar surfaces can be calculated using Eqn.(5.2). For two infinite surfaces, the result is infinite. Therefore, the energy per unit area has to be considered. For two surfaces

$$\frac{\Delta E_{vdW}}{S} = -\frac{A_{132}}{12\pi\ell^2} \tag{5.4}$$

The Hamaker constant A_{132} represents the magnitude of the non–retarded London force and it is positive for an attractive interaction, corresponding to a negative energy. It depends by the material properties of the three media

$$A_{132} = \frac{-3\hbar\ell^2}{\pi}\sum_{0}^{\infty}\rho\mathrm{d}\rho\int_{0}^{\infty}\ln G(\xi)\mathrm{d}\xi \tag{5.5}$$

where $G(\xi)$ is a function of the optical properties of the materials and depends by the geometry of the system [29].

For a film ② bounded by two identical media ①, $G(\xi)$ is given by

$$G_{121}(\xi) = 1 - \Delta_{12}^2 e^{-2a\rho} \tag{5.6}$$

where a is the film thickness and $\rho = \omega/c$ where ω is the real frequency of the radiation of oscillating dipoles. For a film ③, deposited onto the substrate ① placed in the environment ② the function $G(\xi)$ is given by

$$G_{132}(\xi) = 1 - \Delta_{32}\Delta_{12}e^{-2a\rho} \tag{5.7}$$

where Δ_{kj} is defined as

$$\Delta_{kj} = \frac{\epsilon_k(\xi) - \epsilon_j(\xi)}{\epsilon_k(\xi) + \epsilon_j(\xi)} \tag{5.8}$$

and the London dispersion transform is given by [29]

$$\epsilon(\xi) = 1 + \frac{2}{\pi}\int_{0}^{\infty}\frac{\omega\epsilon(\omega)}{\omega^2 + \xi^2}\mathrm{d}\omega \tag{5.9}$$

To determine $\epsilon(\xi)$, experimental data on the interband optical properties $\epsilon(\omega)$ of all three materials are required. Due to the finite frequency range of the spectral data, the values of $\epsilon(\omega)$ at $\omega \to 0$ and $\omega \to \infty$ were approximated by artificially adding analytical extensions or "wings". These wings were varied in order to produce physically reasonable results for the $\epsilon(\xi)$ [27].

A much simpler approach was developed by Lifshitz [30]. Assuming that the optical spectra for each of the materials arise from a single harmonic Lorentz oscillator, an analytical approximation for A_{123} can be derived (the TWA approximation)

$$\begin{aligned} A_{123} &\approx \frac{3}{4}kT\left(\frac{\epsilon_1-\epsilon_3}{\epsilon_1+\epsilon_3}\right)\left(\frac{\epsilon_2-\epsilon_3}{\epsilon_2+\epsilon_3}\right) \\ &+ \frac{3h\nu_e}{8\sqrt{2}}\cdot\frac{(n_1^2-n_3^2)(n_2^2-n_3^2)}{\sqrt{n_1^2+n_3^2}\sqrt{n_2^2+n_3^2}(\sqrt{n_1^2+n_3^2}+\sqrt{n_2^2+n_3^2})} \end{aligned} \tag{5.10}$$

with the dielectric constants ε_i and refractive indices n_i of the three media, and $h\nu_\mathrm{e}$ the energy corresponding to the main electronic UV absorption frequency $\nu_\mathrm{e} \approx 3{\cdot}10^{15}$ Hz. The indices correspond to air, film, and substrate, respectively. Note that the first term of the equation accounts for $\approx 10\%$ of the value of A. The error margins of A in Eqn.(5.10) are $\approx 10\%$, compared to more accurate calculations (Eqn: 5.5).

The entropy argument in the explanation of the "Casimir Effect" is equally applicable to other fluctuating fields. Generalized for any fluctuating spectrum, we expect a finite energy that is associated to the long–wavelength cut–off imposed by a geometrical confinement. We focus our attention on forces stemming from the confinement of thermal noise [17, 31, 32].

Similar to Eqn.(5.4), which gives the interaction energy per unit area due to the confinement of electromagnetic fluctuations, we expect a contribution to the free energy due to the confinement of acoustic modes

$$\frac{\Delta E_\mathrm{ac}}{S} \approx -\frac{kT}{\ell^2} \tag{5.11}$$

As described in Section 2.3.2 the net interaction energy is

$$\frac{\Delta E_\mathrm{ac}}{S} = -\frac{\pi}{36}\frac{kT}{\ell^2} \tag{5.12}$$

In the case of organic films on common hard substrates, at ambient temperatures $|A_{132}| \approx kT$ [13] and because both van der Waals and acoustic energies have the same scaling with the film thickness, ΔE_{vdW} and ΔE_{ac} should be on the same order of magnitude. The derivative of these energies with respect to the film thickness leads to the electromagnetic and acoustic disjoining pressures p_{vdW} and p_{ac}, respectively. Depending on their sign, p_{vdW} and p_{ac} destabilize the film, resulting in a maximally unstable mode [17]

$$q_{\mathrm{max}}^2 \propto \frac{1}{2\gamma}\frac{\partial}{\partial \ell}(p_{\mathrm{vdW}} + p_{\mathrm{ac}}) \tag{5.13}$$

The most unstable mode can be experimentally determined by measuring the wavelength of the film instability

$$\lambda = 2\pi/q_{max} \tag{5.14}$$

Before we discuss the relative role of the electromagnetic and acoustic disjoining pressures on the polymer film stability, it is important to discuss the limitations of Eqn.(5.12). In the case of van der Waals forces, Eqn.(5.4) applies to any combination of dielectric materials ①, ② and ③. For acoustic disjoining pressures, the validity of Eqn.(5.12) is limited to the case of no coupling of the acoustic modes of the intermediary medium ③ (the film) to the adjacent media ① and ②. This implies a large difference in acoustic impedance between the film and the bounding media, which is the case for polymers on hard substrates, such as glass or silicon wafers. Another requirement concerns the existence of long wavelength modes in liquids. The significance of this prerequisite is somewhat controversial, due to the finite compressibility of liquids at high acoustic frequencies [33]. Polymer melts are, however, highly incompressible. As a consequence, acoustic modes with nanometer wavelengths have a mean free path length of several micrometers [34], greater than than the confinement ℓ. Therefore, this modes give rise to a confinement induced disjoining pressure.

5.3 Comparison to Earlier Experiments

It is instructive to predict the effect of the acoustic disjoining pressure in systems that can be experimentally studied. In this context, we review a number of recent publications on the dewetting of thin polymer films and argue

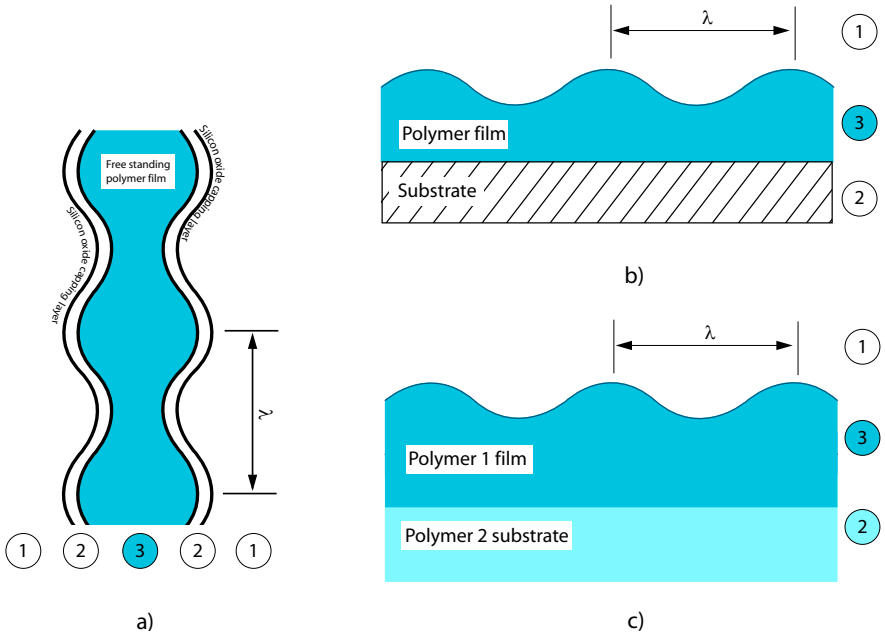

Figure 5.2: Generic experiments for studying the instabilities of thin liquid polymer films. a) Dalnoki et al. [35] used liquid polystyrene films (medium ③) capped between SiOx layers (medium ②). The experiment was performed in air (medium ①). b) Seeman et al. [36] used liquid polymer films (medium ③) between a substrate (medium ②) and air (medium ①). c) Approach used by Jones et al. [38]: the hard substrate was replaced by a liquid polymer.

that the presence of an acoustic disjoining pressure is necessary to adequately describe some of the experimental results. We provide theoretical models of possible experimental setups and indicate the route to prove the acoustic effect.

It is clear from a comparison of Eqns.(5.4) and (5.12) that polymer film stability is governed by the interplay of disjoining pressures of electromagnetic and acoustic origins. While quantitative data on polymer film instabilities are relatively sparse, we reviewed four different published cases. Analyzing the film instability we demonstrated that the magnitude of destabilization could not be explained on the basis of electromagnetic effects alone.

Free standing polymer films

The theoretically most simple case is the stability of a free standing film (Fig. 5.2a). In this case, both p_{vdW} and p_{ac} enhance capillary surface waves and therefore destabilize the film. Experimentally, unstable free standing films are difficult to study. In an elegant approach, Dalnoki et al. [35] have stabilized liquid polystyrene (PS) films by thin solid SiO_2 capping layers. The oxide layers prevents the disintegration of the unstable PS films, thereby facilitating the investigation of the instability. For the parameters of their experiment ($A_{\mathrm{PS}} = 6.5 \times 10^{-21}$ J, T = 210° C), $p_{\mathrm{vdW}} \approx 3p_{\mathrm{ac}}$. This should lead to a rather small contribution ($\approx 10\%$) of the p_{ac} to the measured instability wavelength. The discrepancy between their experimental data and a van der Waals theory is striking. The measured values of λ are too small by a factor of 7, implying a fitted value of the Hamaker constant that deviates from its predicted value by more than three orders of magnitude. The contribution of p_{ac} does not account for the big discrepancy between data and theory reported in [35]. The fitted value of A_{PS}, which is too large by a factor of 2400 possibly originates from stresses in the capping layers.

Polymer films on solid substrates

By far the most common experiments involve liquid polymer films on solid substrates (Fig. 5.2b). Because hard substrates like silicon or glass have much higher acoustic impedances and elastic moduli compared to the polymer coating, we expect only little coupling between the acoustic modes in the film and the substrate. Therefore, in these systems p_{ac} is always present, destabilizing the film. Regarding the van der Waals forces, we distinguish two situations. If the substrate has a refractive index n_1 higher than the polymer film n_3, the Hamaker constant is negative (Eqn. 5.10) and vice versa. For $n_1 > n_3$, this corresponds to a stabilizing effect of the van der Waals forces. For example PS on silicon ($n_1 > n_3$) is stabilized by p_{vdW}, while PS on silicon oxide ($n_1 < n_3$) is unstable. The interplay between stabilizing and destabilizing components of p_{vdW} was demonstrated by Seemann et al. [36]. They used a Si substrate, onto which a PS film is stable. If the substrate is covered with a thin layer of SiO_2, which has a destabilizing effect on the film, a partial compensation of stabilizing and destabilizing vdW disjoining pressures is achieved. On such composite surfaces, thin PS films are unstable, while thicker layers are stable.

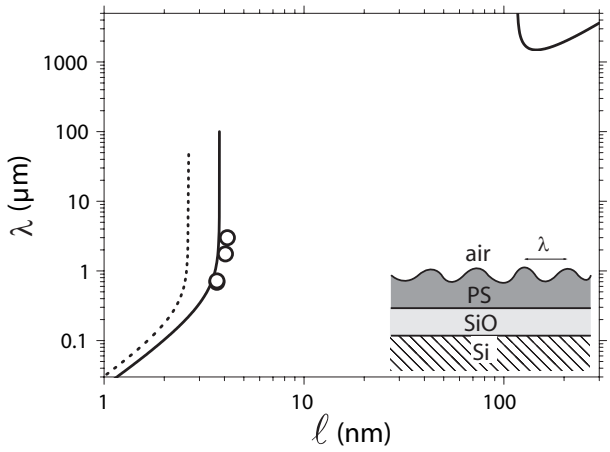

Figure 5.3: Instability wavelength λ vs. film thickness h for PS on a SiO_x covered Si substrate. The experimental data (circles) are better fitted by the theoretical model that includes p_{ac} (solid line) compared to a model based on p_{vdW} alone (dotted line). p_{ac} dominates over the weaker p_{vdW} for larger values of the film thickness ℓ, leading to a predicted reentrant instability (upper right corner).

The measured wavelength λ for three film thicknesses is shown in Fig.(5.3).

For a PS film of a thickness comparable to the dimension of the oxide layer, $p_{vdW} \approx 0$ and the film instability should be dominated by p_{ac}. The dashed line is a prediction based exclusively on van der Waals forces. The data in [36] is quantitatively better explained by the inclusion of p_{ac} (solid line) in the data analysis, compared to the model based on p_{vdW} alone. For values of $h > 100\,\text{nm}$ the acoustic pressure gives rise to a second instability. However, at this large thickness the dynamics of the system is very slow and the estimated time needed for the instability to develop is a few thousands years.

Polymer films on polymer substrates

Capillary instabilities were also observed at polymer–polymer interfaces [37] (Fig. 5.2c). Sferrazza and coworkers [38] quantitatively studied the instability of PMMA films on a PS substrate and PS films on PMMA substrates. Both

systems were annealed at temperatures above T_g of polymers. They interpreted the results of their neutron reflectivity study in terms of a capillary instability of the PMMA–PS interface and determined a Hamaker constant according to Eqn.(5.13). In the case of PMMA on PS, their results were surprising. The negative sign of the experimentally determined and theoretically predicted (Eqn. 5.10) Hamaker constant corresponds to a stable PMMA film. To attribute the PMMA film instability to a dominance of p_{ac} is equally unlikely, because PS and PMMA have very similar acoustic properties. The coupling of the acoustic modes of the PMMA film and the thick PS substrate significantly reduces the confinement of thermo–acoustic modes. For PS on PMMA the authors observed experimentally a stable PS film while the positive value of the theoretically determined Hamaker constant corresponds to an unstable PS film.

Polymer films at the substrate–water interface

Another studied system uses polydimethylsiloxane (PDMS) films, deposited onto silicon wafers covered by water [39, 40]. The experimental setup is similar to the one in Fig.(5.2b), where water was used instead of air as medium ①. The experiments resulted in film instabilities that were modelled by assuming a Si–PDMS–water Hamaker constant that is larger by 2–3 orders of magnitude compared to the predictions of Eqn.(5.10). Similar to the experiments performed by Sferrazza et al., we expect p_{ac} to be negligible, due to a significant acoustic coupling of PDMS and water. A plausible explanation for the large discrepancy between experiments and theory could arise from the polar nature of water. Due to the high dielectric constant of water ($\epsilon_{\mathrm{H_2O}} = 80$), a more detailed model for the calculation of the Si–PDMS–water Hamaker constant [39] is required.

5.4 Predictions

If the coating is stabilized by van der Waals forces, $|p_{\mathrm{ac}}|$ destabilizes the film only if $|A_{132}| < \pi^2/3kT$. This condition computed from Eqns.(5.4) and (5.12), implies $|A_{132}| < 1.3 \times 10^{-20}\,\mathrm{J}$ at room temperature and $|A_{132}| < 2 \times 10^{-20}\,\mathrm{J}$ for T $\approx 170^\circ\,\mathrm{C}$. An unambiguous experimental verification of the presence of an acoustic disjoining pressure necessitates therefore the choice of a system

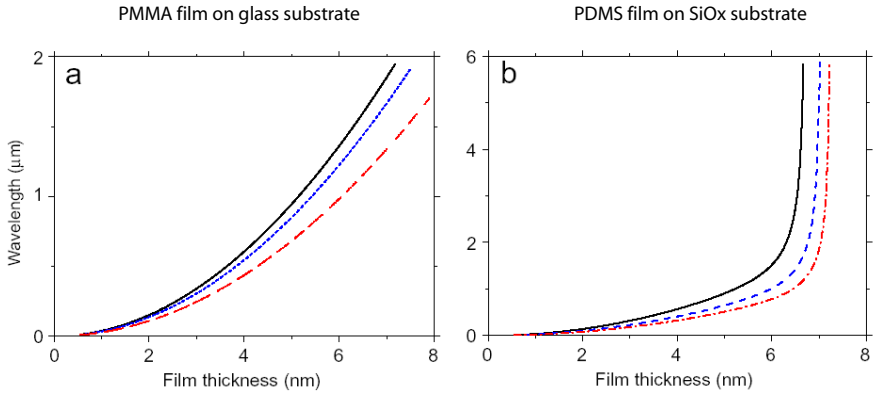

Figure 5.4: Instability wavelength λ vs. film thickness ℓ for a) PMMA ($n = 1.49$) on glass ($n = 1.5$) and b) PDMS ($n = 1.4$) on SiO_2 ($n = 1.46$). The presence of a film instability is a signature of p_{ac}, since vdW forces stabilize the film. The solid, dotted and dashed lines in a) correspond to temperatures of 50° C, 90° C and 170° C, the solid, dashed and dash–dotted lines in b) correspond to temperatures of 50° C, 170° C and 270° C respectively.

with low values of $|A_{132}|$ and suitable mechanical boundary conditions. Before turning to our experiments, possible routes are presented that can be used to verify the presence of a disjoining pressure arising from the confinement of thermally excited acoustic modes.

5.4.1 Marginally van der Waals stabilized polymer films

One way of proving the existence of p_{ac} is to chose an experimental film–substrate system (Fig. 5.2b), in which p_{vdW} stabilizes the film but is overpowered by a destabilizing p_{ac}. To fulfill this condition, the Hamaker constant has to satisfy: $-1.3 \times 10^{-20}\mathrm{J} < A_{132} < 0$. This condition is fulfilled when the refractive index of the substrate is larger than the refractive index of the film ($n_1 \gtrapprox n_3$). Fig.(5.4) shows the results of a linear stability analysis [42] of two polymer–substrate combinations. The polymer films are expected to be marginally stable in terms of their van der Waals energy, but unstable if p_{ac} is taken into account. Fig.(5.4a) shows the maximally unstable mode of PMMA

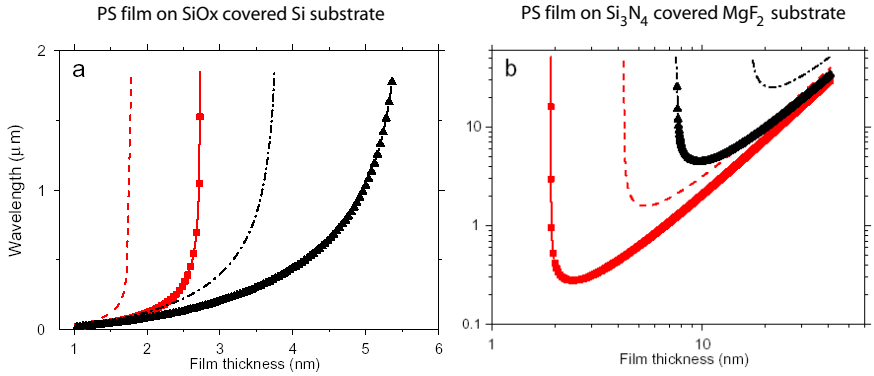

Figure 5.5: Instability wavelength λ vs. film thickness ℓ for PS on composite substrates. a) PS on Si covered with 1.6 nm (■) and 3.5 nm (▲) thick SiOx layers. b) PS on MgF_2 covered by 0.5 nm (■) and 2 nm (▲) thick Si_3N_4 layers. On the stabilizing substrate in a), the curves diverge for $\ell > \ell_c$, while on the destabilizing substrate in b), the stabilizing Si_3N_4 layer introduces a lower cut–off in ℓ, below which the film should be stable. The dashed and dash–dotted lines correspond to the assumption $p_{ac} = 0$.

($n_{PMMA} = 1.49$) on a microscopy glass slide (white glass with $n_{glass} = 1.50$). The predicted value of $A_{132} = -1.48 \times 10^{-21}$ J leads to a stabilizing effect of p_{vdW}, which is one order of magnitude smaller compared to p_{ac}. A complementary system is PDMS ($n_{PDMS} = 1.40$) on SiO_2 ($n_{SiO_2} = 1.46$), shown in Fig.(5.4b) ($A_{132} = -6.22 \times 10^{-21}$ J). According to our predictions, the observation of an unstable film that is expected to be stable if only van der Waals forces, should be observable.

5.4.2 Film instabilities on composite substrates

This approach was already introduced by Seeman et al. [36]. The composite substrate consisted of a silicon wafer covered by a thin silicon oxide layer. On such composite substrates, the film is stabilized by one of the components and destabilized by the other. There is a critical polymer film thickness ℓ_c, at which $p_{vdW} = 0$. This is reflected in the stability diagram of the film (Fig.

5.5). In the first case (Fig. 5.5a), the substrate has a stabilizing effect, while the surface layer destabilizes the film. The film shows a spinodal instability for $\ell < \ell_c$ and metastable films are expected for $\ell > \ell_c$. In Fig.(5.5b), the inverted situation is shown. In this case, the MgF_2 substrate destabilizes the film, while the Si_3N_4 layer stabilizes it. This instability diverges at small film thicknesses due to the stabilizing effect of the Si_3N_4 layer while the divergence at high thicknesses is due to the continuous decrease in the disjoining pressure with increasing film thickness. In both situations, the presence of p_{ac} shifts ℓ_c to larger film thicknesses, in agreement with the data in [36]. This kind of study, encompassing a large number of experimental parameters should reveal, whether there is a systematic shift in ℓ_c with p_{ac}. Such a systematic shift, would be a clear signature of a disjoining pressure stemming from acoustic fluctuations.

5.4.3 Temperature dependence of film instabilities

A third possible approach involving composite substrates, similar to the ones described in Section 5.4.2, attempts to infer information about the presence of p_{ac} from the temperature dependence of ℓ_c. The Hamaker constant is only weakly temperature dependent (the optical properties of most materials change only little with temperature). Therefore, taking both the variation of surface tensions and Hamaker constants into account, only a negligible variation of ℓ_c with temperature is expected. The effect of an inclusion of p_{ac} in the model should result in an experimentally discernible variation of ℓ_c.

5.4.4 Retardation effects

When increasing the film thickness, there is a decrease in correlations of confined electromagnetic modes, or, in the London model, a decrease in correlation in dipole–dipole interactions. The scaling of the van der Waals forces with distance (Eqn. 5.3) is changed. Eqn.(5.12) on the other hand, stays unchanged (assuming that the mean free path length of acoustic modes is still large compared to the film thickness). In terms of Eqn.(5.13), this implies a dominance of p_{ac} over p_{vdW} for $\ell \gtrsim 100\,\text{nm}$. While this leads to interesting predictions for large values of ℓ (e.g. reentrant instabilities [17]), instabilities of thick films are experimentally difficult to study. Because the characteristic time constant associated with capillary instabilities scale with ℓ^5, in thick

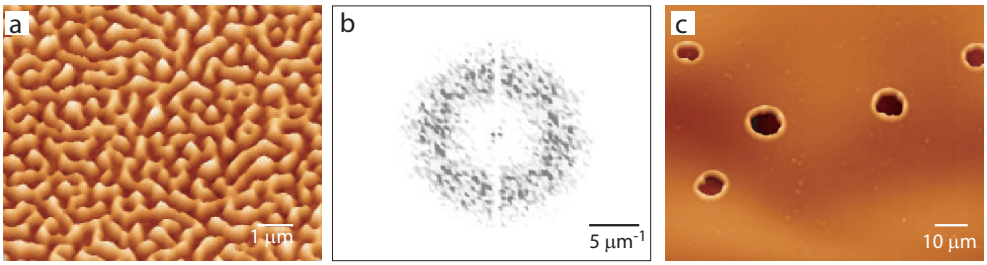

Figure 5.6: AFM images of thin polymer films. (a) The 2.4 nm thick PS film on an oxide covered Si wafer (inset in Fig.(5.7) has developed the characteristic pattern of a capillary instability after annealing for ≈ 15 *min at* $50°C$*. (b) shows the Fourier transform of (a) with* $\lambda = 450 \pm 154$ *nm. A small thickness increase to* $\ell = 3.7$ *nm results in a film that is stable for many hours at* $50°C$*. Raising the temperature to* $170°C$ *gives rise to the drastically changed morphology in (c), where the film broke-up by the nucleation of isolated holes.*

films they are typically preempted by the heterogeneous nucleation of holes [10]. Experiments exploiting the change in the balance of retarded electromagnetic and thermo–acoustic modes require a liquid film with a low surface tension and a low viscosity (e.g. low molecular weight PDMS).

5.5 The Experiments

When discussing the origin of the disjoining pressure from the view–point of the confinement of a fluctuation spectrum, it becomes clear that not only electromagnetic effects (leading to a van der Waals disjoining pressure), but also thermally excited acoustic fluctuations play a role in the destabilization of thin films.

Because the Hamaker constants are on the order kT for typically studied thin film systems and temperatures, an unambiguous experimental discrimination between the acoustic disjoining pressure and the van der Waals one, is not trivial. Since $p_{\rm ac}$ and $p_{\rm vdW}$ have the same dependence on the film thickness ℓ, only quantitative measurements allow to distinguish the two effects. According to our predictions, $p_{\rm ac}$ is expected to be significant in the case of supported films on hard substrates. The experimental systems described in

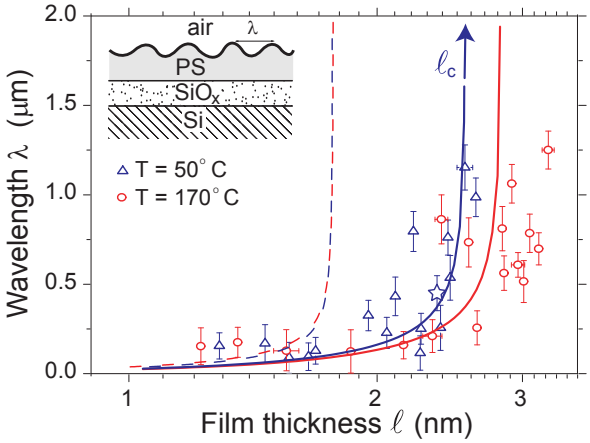

Figure 5.7: Temperature dependence of the capillary instability. PS films on Si wafers covered by a 1.6 nm thick SiO_x layer (inset) show a capillary instability for $\ell < \ell_c$. The plot of λ vs. ℓ shows a temperature increase of the experimentally determined cut-off from $\ell_c = 2.4 \pm 0.2\,nm$ at $T = 50°C$ ($\triangle$) to $\ell_c = 3.0 \pm 0.2\,nm$ at $T = 170°C$ ($\circ$). The lines are predictions of Eqn.(5.14) with $p = p_{vdW} + p_{ac}$, the dashed lines correspond to $p_{ac} = 0$.

the previous sections are conceptually simple, but require high precision measurements. Films and surface layer thicknesses must be determined with a sub–nanometer precision and an accuracy of ~ 100 nm is necessary for the determination of the instability wavelength. This requires carefully conducted experiments, and a combination of ellipsometry and atomic force microscopy as experimental techniques.

We have pursued three independent experimental approaches to unambiguously distinguish between p_{vdW} and p_{ac}: (*i*) the investigation of the differing temperature dependence of Eqns.(5.4) and (5.12), (*ii*) the case of opposing pressures p_{vdW} and p_{ac}, and (*iii*) the dependence of the film instability on the acoustic boundary conditions.

The typical morphology of an unstable polymer film heated above its glass transition temperature is shown in Fig.(5.6). In Fig.(5.6a), the surface pattern of a 2.4 nm thick PS film on an oxide covered Si wafer is shown. The wavelength λ of the instability was obtained by Fourier analysis shown in Fig.(5.6b). The wavelength of the instability is extremely sensitive to variations in the

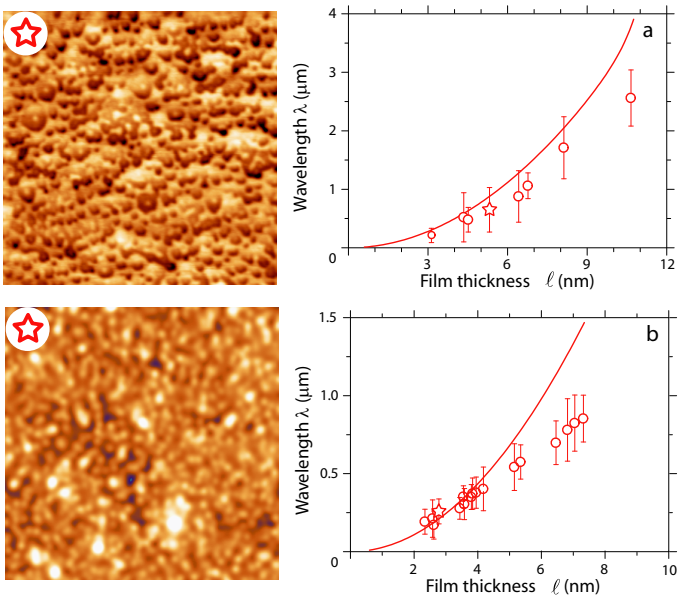

Figure 5.8: Capillary instability of films with stabilizing van der Waals forces. Since $n_f = 1.49 < n_s = 1.52$ *for PMMA on glass (a) and* $n_f = 1.45 < n_f = 1.49$ *for PAAM on* SiO_x *(b), both films are expected to be stable, when only van der Waals forces are considered (*$p_{ac} = 0$*). The annealing temperatures were* $130°C$ *and* $170°C$*, respectively. The lines are predictions from Eqn.(5.14) with* $p = p_{vdW} + p_{ac}$ *(note that for* $p_{ac} = 0$*,* $\lambda = \infty$*). The micrographs show typical* $5 \times 5\,\mu m^2$ *AFM images corresponding to the data points marked by the stars.*

film thickness. An increase in the film thickness by only $\approx 1\,nm$ causes a fundamental change in the film morphology. The 3.7 nm thick film in Fig.(5.6c) is stable against acoustic and van der Waals forces and breaks–up only by the heterogeneous nucleation of individual holes [10]. This process can have a variety of causes, such as impurities in the film or at its surface. Depending on the film thickness and viscosity, this process can preempt a capillary instability. In our experimental setup it is the signature that the film is stable with respect to capillary waves.

From a theoretical point of view, the measured wavelength of the film instability in Fig.(5.6a) was analyzed in terms of Eqn.(5.13). We considered

the competition between the destabilizing overall pressure $p_{\rm vdW} + p_{\rm ac}$ and the restoring surface tension γ.

Because both $p_{\rm vdW}$ and $p_{\rm ac}$ have the same variation with film thickness ℓ, in a first approach we used the temperature T as a control parameter. We utilized that $p_{\rm ac}$ varies linearly with T, while the Hamaker constant A has only a weak temperature dependence determined by the weak variation of n_i and ε_i with T^2.

The experimental system consisted of PS films deposited on silicon wafers covered by a native 1.6 nm thick oxide layer. The substrates were first cleaned in a jet of CO_2 crystals ("snow jet") [41] and subsequently in a "piranha" solution (70% H_2SO_4, 30% H_2O_2) at 80°C. After the chemical cleaning step, the substrates were thoroughly washed in Millipore water. The Si wafers (110, p-type) as received were covered by a 1.6 nm thick SiO_x layer as measured by ellipsometry. The lateral resolution of the imaging ellipsometer ($\approx 2\,\mu$m) assured the homogeneity of the samples. The refractive index of SiO_x and Si were 1.46 and 4.11, respectively. The PS ($M_{\rm w} = 1.92$ kg/mol, $M_{\rm w}/M_{\rm n} = 1.06$, $n_{\rm f} = 1.59$) films were spin–coated at 10.000 RPM from toluene solutions of concentrations ranging from 0.05 to 0.15 % by weight. The films were liquified by heating. After annealing, all samples were imaged by optical microscopy and atomic force microscopy (AFM).

The oxide layer has a destabilizing effect on the PS film, which is otherwise stable on pure Si substrates. It is this particular force balance that makes the set-up sensitive for the detection of p. At a critical thickness $\ell_{\rm c}$ the van der Waals pressures of both the substrate and the oxide layer have the same magnitude and therefore cancel each other. At film thicknesses below this critical value $\ell < \ell_{\rm c}$, the films are unstable (Fig. 5.6a) with a sharp divergence $\lambda \to \infty$ at $\ell_{\rm c}$, where $p = 0$ [36, 17]. The influence of an additional destabilizing disjoining pressure such as $p_{\rm ac}$ shifts the divergence to higher film thicknesses.

The results of these experiments are shown in Fig.(5.7), where the instability wavelength λ extracted from images similar to Fig.(5.6a) is plotted versus ℓ. Despite the scatter in the data, changing the annealing temperature from $T = 50$°C to $T = 170$°C clearly causes a shift in the experimentally determined values of the divergence from $\ell_{\rm c} = 2.4 \pm 0.2$ nm to $\ell_{\rm c} = 3.0 \pm 0.2$ nm.

[2]The reduction of γ with increasing temperature in Eqn.(5.14) changes the shape of the dashed line in Fig.(5.7) but not the value of ℓ_c. The temperature variation of A and γ were taken into account in all calculations

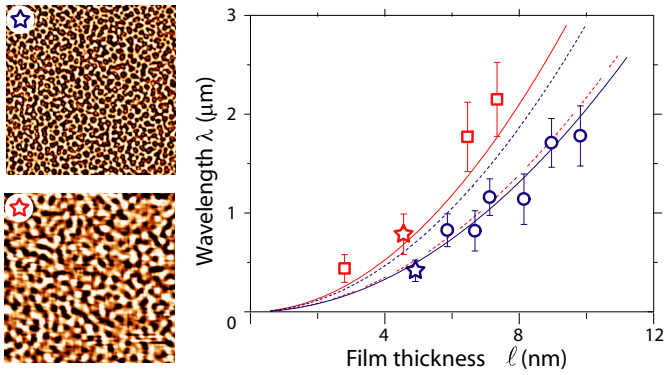

Figure 5.9: Dependence of the film instability on the acoustic boundary condition. Comparison of PS on PMMA (□) and PS on SiO_x (○). The lack of acoustic confinement for PS on PMMA (dashed line: p_{ac} from Eqn.(5.12), solid line: $p_{ac} = 0$) gives rise to larger values of λ compared to PS on SiO_x (solid line: p_{ac} from Eqn.(5.12), dotted line: $p_{ac} = 0$). The micrographs show typical $5 \times 5\,\mu m^2$ AFM images corresponding to the data points marked by the stars.

This enhancement of the film instability caused by the increase in annealing temperature cannot be explained by the (marginal) temperature dependence of A alone – dashed lines in Fig.(5.7. The incorporation of the temperature dependence of p_{ac} is essential to account for the data.

In a second class of experiments, we chose a system in which p_{vdW} has a stabilizing effect on the film, while p_{ac} destabilizes it. The effect of van der Waals forces was adjusted by adequately choosing the optical properties of the substrate and the film.

Films of PMMA ($M_w = 2.50\,kg/mol$, $M_w/M_n = 1.07$, $n_f = 1.49$) were spin–coated from toluene solutions onto glass substrates with refractive index ranging from 1.5 to 1.7. Films of polyacrylamide (PAAM) ($M_w = 1.52\,kg/mol$, $M_w/M_n = 1.12$) were spin–coated from water solutions onto SiO_x substrates. SiO_x substrates were thermally grown by placing Si wafers into an air–filled oven set to 900°C for 3.5 h. This resulted in a 110 nm thick SiO_x layer on Si. The substrates were cleaned in the same manner as for the previous type of experiments. The glass substrates were also cleaned by sonication in ethanol, acetone, and Millipore water for 10 min each previous to the chemical etch in

piranha solution.

While it is difficult to accurately predict the magnitude of A from Eqn.(5.5) due to the lack of accurate absorbtion spectra for the materials used in our study, its sign can be reliably predicted from Eqn.(5.10). A is positive (destabilizing), if the refractive indices of the two media bounding the film (air (n_a) and substrate (n_s)) are lower compared to the film (n_f), and negative (stabilizing), if $n_s > n_f > n_a$. From an electromagnetic point of view, polymer films on high refractive index materials are therefore expected to be stable. To demonstrate the effect of the acoustic Casimir pressure, we chose two experimental systems with $n_s \gtrsim n_f$. According to a model which includes only van der Waals forces, the film is expected to be stable.

For both systems the refractive index of the polymers was smaller compared to the substrates. PMMA had a refractive index of $n_f = 1.49$ and for the glass substrate n_s ranged between 1.5 and 1.7. For the second system the refractive index of PAAM was $n_f = 1.45$ and for the thermally grown SiO_x, $n_s = 1.49$. In both cases, the stabilizing effect of the van der Waals forces is weak, due to the similarity of the optical properties of the substrate and the film. In the case of PMMA on glass $|p_{ac}/p_{vdW}| \approx 3$ and $|p_{ac}/p_{vdW}| \approx 7$ for PMMA and PAAM, respectively.

Both sample series show the distinct signature of a capillary instability for film thicknesses smaller than 12 nm – AFM micrographs in Fig.(5.8. As van der Waals forces alone are stabilizing for both films, the observation of a capillary instability is direct evidence for the presence of a destabilizing force. Fig.(5.8) shows the variation of λ versus ℓ for PMMA and PAAM films, respectively. The data are in reasonable agreement with the predictions from Eqn.(5.14) using $p = p_{vdW} + p_{ac}$.

For PMMA on glass, we found unstable PMMA films for $n_s = 1.51$ and $n_s = 1.61$, while for glass substrates with $n_s = 1.71$ no capillary instabilities were observed. In the latter case, the stabilizing effect of p_{vdW} overpowers the destabilizing influence of p_{ac}

In a third experimental test, we varied the acoustic boundary conditions, which allowed us to switch on and off the acoustic disjoining pressure. A prerequisite for the confinement of long wavelength thermal modes is the acoustic isolation of the film from the surrounding media. This implies a large enough difference in densities and elastic properties of the film and the substrate [17]. By choosing a soft substrate with similar acoustic properties as the film, we

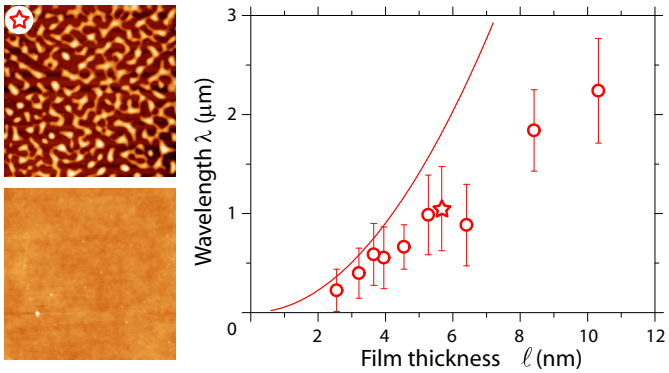

Figure 5.10: Dependence of the film instability on the acoustic boundary condition. Comparison of PMMA on two substrates with $n_s \approx 1.6$. In the absence of acoustic confinement ($p_{ac} \approx 0$) on a PS substrate, the PMMA film is stabilized by $p_{vdW} < 0$ (bottom AFM micrograph). On a glass substrate with $n_s = 1.61$, $p_{ac} > |p_{vdW}|$ the PMMA film is unstable (top AFM micrograph, data points). The images are typical $5 \times 5\,\mu m^2$ AFM micrographs corresponding to the data points marked by the stars.

expect the suppression of p_{ac}.

PS ($M_w = 1.92\,kg/mol$, $M_w/M_n = 1.06$) and polymethylmethacrylate (PMMA) ($M_w = 2.50\,kg/mol$, $M_w/M_n = 1.07$) was used. PS was spin–coated from toluene solutions onto thermally grown SiO_x substrates and from cyclohexane onto PMMA ($M_w = 1080\,kg/mol$, $M_w/M_n = 1.16$) substrates. The PMMA was spin–coated from toluene solutions onto glass substrates and from acetic acid solutions onto PS ($M_w = 2057\,kg/mol$, $M_w/M_n = 1.14$) substrates.

First, we compared the behavior of PS ($n_s = 1.59$) on PMMA ($n_s = 1.49$) to a complementary system where we replaced the PMMA substrate with SiO_x $n_s = 1.49$. Because of the similar optical properties between the two substrates, the destabilizing p_{vdW} is of similar magnitude. Differences in the observed film instability should therefore be due to differing values of p_{ac}. Fig.(5.9) shows the comparison of PS on SiO_x and PMMA substrates. A visual comparison of the instability of $\approx 4.7\,nm$ thick PS films on the two substrates (AFM micrographs) reveals a large difference in λ, which is indicative for a difference in destabilizing pressures. The lower values of λ for PS on SiO_x, compared to PS on PMMA is readily explained by the lack of confinement of

the acoustic modes ($p_{ac} \approx 0$) when using PMMA substrates. For the polymer–polymer system, the only contribution to the film destabilization is due to the p_{vdW} alone. For the polymer on SiO_x, the additional influence of p_{ac} leads to a stronger destabilization force giving rise to lower λ values.

The complementary study compared the behavior of PMMA ($n_s = 1.49$) on glass ($n_s = 1.61$) to PMMA on PS ($n_s = 1.59$) (Fig. 5.10). Similar to the previous case, the optical properties of the two substrate types are comparable, implying similar values of p_{vdW}. In this experimental situation, p_{vdW} has a stabilizing effect on the films. The results reflect therefore the competition of p_{vdW} and p_{ac}, as discussed above (Fig. 5.8). When PS substrates were used (where $p_{ac} \approx 0$) the PMMA films were stable and did not exhibit a capillary instability (bottom–left AFM micrograph). On the glass substrates, on the other hand, the dominating effect of the acoustic disjoining pressure ($p_{ac} > |p_{vdW}|$) caused a spontaneous film instability (top–left AFM micrograph) predicted by Eqn.(5.14).

5.6 Conclusion

When performing these experiments, residual potentials originating from electrostatic [43, 44] and temperature gradients [45, 46] effects, the complex interplay of capillary waves and hole nucleation [47, 48], or stored stresses in the films caused by their preparation [49] have to be taken into account. These sources for non-van der Waals driven instabilities may provide the explanation of the discrepancies between the experiments and the model calculations. We took utmost care to eliminate or minimize such additional effects. However, it is the qualitative nature of the three complementary experimental approaches used here that allows us to identify forces caused by the confinement of thermal noise. Our experiments confirmed all qualitative predictions regarding the temperature dependence, magnitude and relevant boundary conditions predicted for the destabilizing effect of p_{ac}. In addition, we find a reasonable quantitative agreement of the model from Eqn.(5.14) with our data.

Our study demonstrates the high sensitivity of film instabilities to forces acting over small distances. As opposed to pressures caused in the film by external potentials or preparation conditions, the acoustic Casimir effect is a fundamental consequence of thermodynamic fluctuations.

Bibliography

[1] Lord Rayleigh; *Proc. London Math. Soc.* **10**, 1897

[2] A. Vrij; *Discuss. Faraday Soc.* **42**, 1966

[3] A. Scheludko; *Adv. Colloid Interface Sci.* **1**, 1967

[4] E. Ruckenstein, R.K. Jain; *J. Chem. Soc. Faraday Trans.II* **70**, 1974

[5] J. Cahn; *J. Chem. Phys.* **42**, 1965

[6] R. Xie, A. Karim, J.F. Douglas, C.C. Han, R.A. Weiss, *Phys. Rev. Lett.* **81**, 1998; A. Sharma, R. Khanna, *Phys. Rev. Lett.* **81**, 1998; G. Reiter, R. Khanna, A. Sharma, *Phys. Rev. Lett.* **85**, 2000; L.M. Pismen, Y. Pomeau, *Phys. Rev. E* **62**, 2000; R. Khanna, A. Sharma, G. Reiter, *EPJdirect E* **2**, 2000; U. Thiele, M.G. Velarde, K. Neuffer, *Phys. Rev. Lett.* **87**, 2001; U. Thiele, M.G. Velarde, K. Neuffer, Y. Pomeau, *Phys. Rev. E* **64**, 2001; K.D.F. Wensink, B. Jerome, *Langmuir* **18**, 2002; A. Sharma, J. Mittal, *Phys. Rev. Lett.*, **89**, 2002; A. Sharma, J. Mittal, R. Verma, *Langmuir* **18**, 2002

[7] E. Schäffer, T. Thurn–Albrecht, T.P. Russell, U. Steiner; *Nature* **403**, 2000

[8] E. Schäffer, S. Harkema, M. Roerdink, R. Blossey, U. Steiner; *Adv. Mater.* **15**, 2003

[9] E. Schäffer, T. Thurn–Albrecht, T.P. Russell, U. Steiner; *Europhys. Lett.* **53**, 2002

[10] C. Redon, F. Brochard-Wyart, F. Rondelez; *Phys. Rev. Lett.* **66**, 1991; G. Reiter, *Phys. Rev. Lett.* **68**, 1992; A. Sharma, G. Reiter, *J. Colloid Interf. Sci.* **178**, 1996; K. Jacobs, S. Herminghaus, K.R. Mecke, *Langmuir* **17** 1998; U. Thiele, M. Mertig, W. Pompe, *Phys. Rev. Lett.* **80**, 1998; G. Reiter, *Phys. Rev. Lett.* **87**, 2001

[11] S. Herminghaus; *Phys. Rev. Lett.* **83**, 1999

[12] K. Dalnoki-Veress, B.G. Nickel, J.R. Dutcher; *Phys. Rev. Lett.* **82**, 1999

[13] J. N. Israelachvili; *Intermolecular and surface forces*, Academic Press, London, 1991.

[14] M. Kadar, R. Golestanian; *Rev. Mod. Phys.*. **71**, 1999

[15] E. Buks, M. L. Roukes; *Nature* **419**, 2002

[16] A. Larazza, C. D. Holmes, T. Susbilla, B. Denardo; *J. Acoust. Soc. Am.* **103**, 1998

[17] E. Schäffer, U. Steiner; *Eur. Phys. J. E* **8**, 2002

[18] H.B.G. Casimir *Proc. Kon. Ned. Akad. Wetensch.* **51**, 1948; H.B.G. Casimir, D. Polder, *Phys. Rev.* **73**, 1948; H.B.G. Casimir, *J. Chem. Phys.* **46**, 1949;

[19] R. Eisenschitz, F. London; *Z. Physik* **60**, 1930; F. London; *Trans. Faraday Soc.* **33**, 1937

[20] A.D. McLachlan; *Proc. Roy. Soc.* **A274**, 1963

[21] D. Langbein; *Springer Tracts in Modern Physics* **72**, 1974

[22] P. Hohenberg W. Kohn; *Phys. Rev.* **136**, 1964

[23] W. Kohn, L.J. Sham; *Phys. Rev.* **140**, 1965

[24] O. Gunnarsson, B.I. Lundqvist; *Phys. Rev. B* **13**, 1976

[25] D.C. Langreth, M.J. Mehl; *Phys. Rev. B* **28**, 1983

[26] A.D. Becke; *Phys. Rev. A* **38**,1988

[27] R.H. French, R.M. Cannon, L.K. DeNoyer, Y.M. Chiang; *Solid State Ionics* **75**, 1995.

[28] H.C. Hamaker; *Physica* **4**,1937

[29] D.B. Hough, L.R. White; *Adv. Colloid Interface Sci.* **14**, 1980.

[30] E.M. Lifshitz; *Sov. Phys. JETP* **2**, 1956.

[31] I. E. Dzyaloshinskii, E. M. Lifshitz, L. P. Pitaevskii; *Adv. Phys.* **10**, 1961.

[32] O. Bschorr; *J. Acoust. Soc. Am.* **106(6)**, 1999

[33] D.Y.C. Chan, L.R. White; *Physica* **122A**, 1983.

[34] C.J. Morath, H.J. Maris; *Phys. Rev. B* **54**, 1996.

[35] K. Dalnoki-Veress, B.G. Nickel, J.R. Dutcher; *Phys. Rev. Lett.* **82**, 1999

[36] R. Seemann, S. Herminghaus, K. Jacobs; *J. Phys.: Condens. Matter.* **13**, 2001

[37] P. Lambooy, K.C. Phelan, O. Haugg, G. Krausch; *Phys. Rev. Lett*, **76**, 1996; M.O. David, G. Reiter, T. Sitthaï, J. Schultz, *Langmuir* **14**, 1998; R. Segalman, P.F. Green, *Macromolecules* **32**, 1999; C. Wang, G. Krausch, M. Geoghean, *Langmuir* **17**, 2001; A.M. Higgins, M. Sferrazza, R.A.L. Jones, P.C. Jukes, J.S. Sharp, L.E. Dryden, J. Webster, *Eur. Phys. J. E* **8**, 2002.

[38] M. Sferrazza, M. Heppenstall–Butler, R. Cubitt, D. Bucknall, J. Webster, R.A.L. Jones; *Phys. Rev. Lett.* **81**, 1998

[39] G. Reiter, A. Sharma, R. Khanna, A. Casoli, M.-O. David; *J. Colloid Interface Sci.* **214**, 1999

[40] G. Reiter, A. Sharma, A. Casoli, M.-O. David, R. Khanna, P. Auroi; *Langmuir* **15**, 1999; G. Reiter, R. Khanna, A. Sharma; *Phys. Rev. Lett.* **85**, 2000

[41] R. Sherman, D. Hirt, R.J. Vane; *J. Vac. Sci. Technol.* **12**, 1994

[42] F. Brochard–Wyart, F. Daillant; *Can. J. Phys.* **68**, 1990

[43] E. Schäffer, T. Thurn-Albrecht, T. P. Russell, U. Steiner, *Nature* **403**, 2000

[44] E. Schäffer, T. Thurn-Albrecht, T. P. Russell, U. Steiner, *Europhys. Lett.* **53**, 2001

[45] E. Schäffer, S. Harkema, R. Blossey, U. Steiner, *Europhys. Lett.* **60**, 2002

[46] E. Schäffer, S. Harkema, M. Roerdink, R. Blossey, U. Steiner, *Macromolecules* **36**, 2003

[47] U. Thiele, M. G. Velarde, K. Neuffer, *Phys. Rev. Lett.* **87**, 2001

[48] J. Becker *et al.*, *Nature Mater.* **2**, 2003

[49] G. Reiter, Ed., *Eur. Phys. J. E*, in preparation.

Chapter 6

Lithographic Techniques Using External Fields

6.1 Introduction

The stability of thin polymer films is very important in many technological applications. Ranging from photo–lithography to coatings, the ability to deposit stable films with uniform thickness is crucial. In general, thin films are stable against capillary fluctuations at their surfaces. In the absence of heterogeneities, thin non–wetting films may be destabilised by van der Waals (vdW) and other forces [1]. Because these interactions are relatively weak and short ranged, films thicker than $\sim 20\,\mathrm{nm}$ are typically stable. To destabilize thick films, long–range forces such as electrostatic or temperature gradient induced forces must be applied to the polymer–air interface [2, 3].

The application of an external force permits to control the instabilities, if the magnitude of the force can be varied. Our lithographic technique exploited a spontaneous structure formation process and decreased its length scale to technologically interesting features sizes. The ability to fabricate

nanostructures is essential in the development of functional devices that incorporate nanoscale features. Hence, non–photolithographic methods could provide technologically simpler and cheaper nanofabrication routes. In this chapter, an extension of the electrohydrodynamic (EHD) technique is presented that allowed us to produce structures in the range of 100 nm. The influence of several factors such as film thicknesses, field strength, imposed periodicity, etc. on the lithographic technique are presented.

6.2 Classical EHD Lithography

Schäffer et al. developed a new lithographic technique that uses electrostatic forces to control the initial film instabilities [2]. When applying an electric field normal to the interface between two dielectric materials with different polarizabilities, an interfacial electrostatic pressure arises from the uncompensated displacement charges. This pressure couples to the capillary wave spectrum of the liquid interface. A narrow band of wavelengths is amplified, destabilizing the interface. The most unstable wavelength is characteristic of the interfacial force balance, where the Laplace pressure acts as a restoring force. The generic experiment is schematically depicted in Fig.(6.1).

The setup used by Schäffer et al. consisted of a ≈ 100 nm thin polymer film, deposited by spin–coating on a substrate that served as one of the electrodes. Facing the polymer layer, a second electrode was placed at distance d from the first one. The initial film thickness was $h < d$. The film was liquified by heating to a temperature higher than its T_g and a voltage was applied to the electrodes. Due to the small distance between the electrodes the generated electric field was extremely high ($E \sim 10^7\,\mathrm{V{\cdot}m^{-1}}$). The instability was given time to develop and after a period that ranged from several hours to a couple of days, the formed structure was frozen by quenching the entire setup to room temperature. The upper electrode was mechanically removed and the sample was investigated by optical and atomic force microscopy. To facilitate the disassembly of the device, the surface of the upper electrode was covered with a self–assembled alkane monolayer.

Typical experimental results are shown in Fig.(6.1). The initial capillary film undulations (Fig. 6.1a) were amplified by the electrostatic pressure. They grew and eventually touched the upper electrode forming columns (Fig. 6.1b). Changing the system parameters (applied voltage, distance between

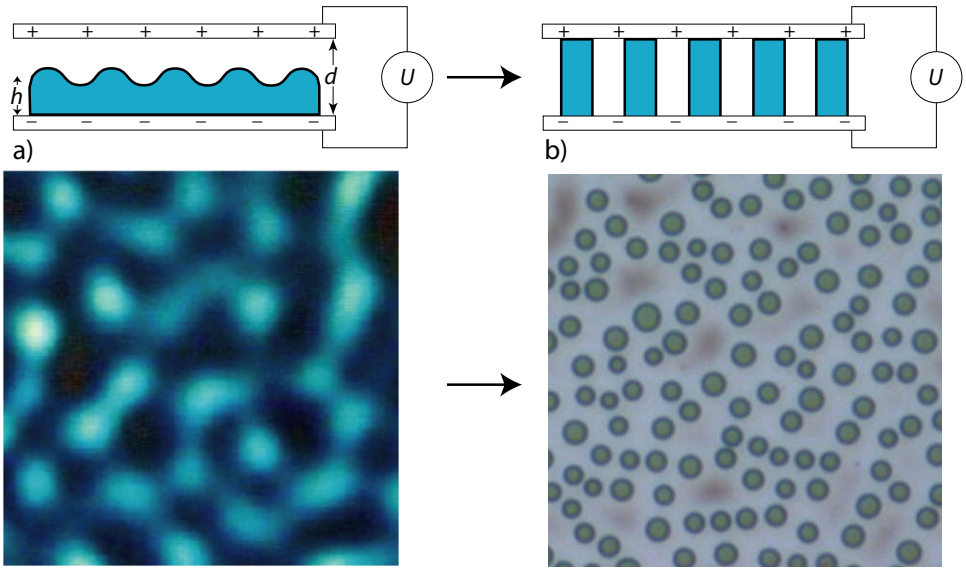

Figure 6.1: Schematic representation of the EHD setup. A liquid polymer film is destabilized by an electrostatic pressure, which is a consequence of the applied electric field. Depending on the voltage U, the electrode spacing d, the initial film thickness ℓ, the dielectric constant ϵ_p, and the surface tension γ, a narrow distribution of wavelengths λ is amplified. The optical micrographs are a) $5 \times 5\,\mu\mathrm{m}^2$ and b) $30 \times 30\,\mu\mathrm{m}^2$.

electrodes, initial film thicknesses) the density and size of the columns could be varied.

To induce the morphological features showed in Fig.(6.1b), a laterally homogeneous electric field was used. By utilizing laterally variable electric fields, Schäffer et al. developed a lithographic technique that harnessed the initial film instability to replicate patterns with extremely high fidelity. The process is schematically depicted in Fig.(6.2)

Instead of planar electrode, a topographically structured upper plate[1] was used (Fig. 6.2a). The variation of the plate spacing d due to the electrode

[1]The master electrode was produced by "writing" the structures with an electron beam.

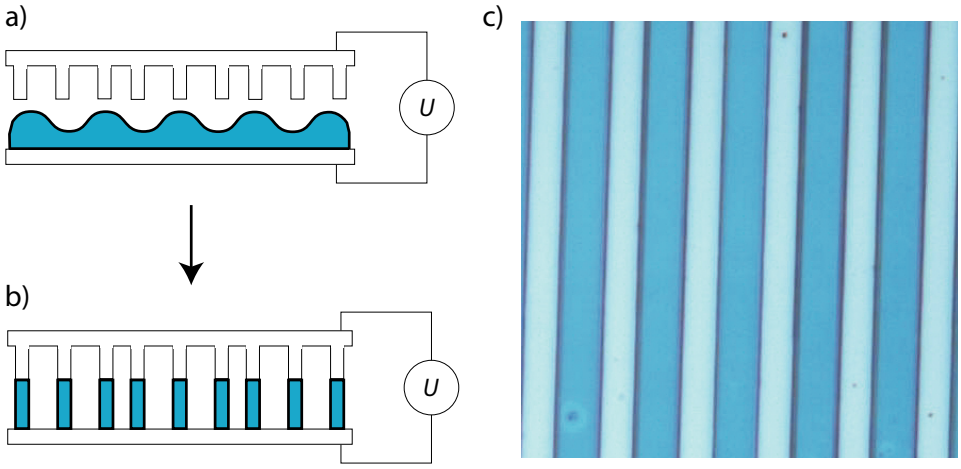

Figure 6.2: A structured upper plate creates a heterogeneous force field, focusing the instability towards the protruding structures. A positive replica of the master pattern is transferred into the polymer. In unstructured regions, the film remains stable on a much longer timer scale. The optical micrograph is $20 \times 20\,\mu\mathrm{m}^2$.

topography results in a variation of the force field. Therefore, the lateral inhomogeneous field focusses the instability towards regions of highest electric field where the electrostatic pressure has a higher magnitude (i.e. underneath the protuberances). Furthermore, the time constant associated with this process is much smaller underneath the structures, so that the polymer is destabilized first at the regions where d is smallest. This leads to the replication of the electrode topography, which is transferred into the polymer film (Fig. 6.2b and c).

6.3 Hierarchical Structure Formation in E–Fields

Similar to most other lithographic methods, the method described in Section 6.2 structures a single layer of polymer. For many applications, however, it is desirable to control the spatial arrangement of more than one component. With traditional methods, this process requires an iterative, multistep pro-

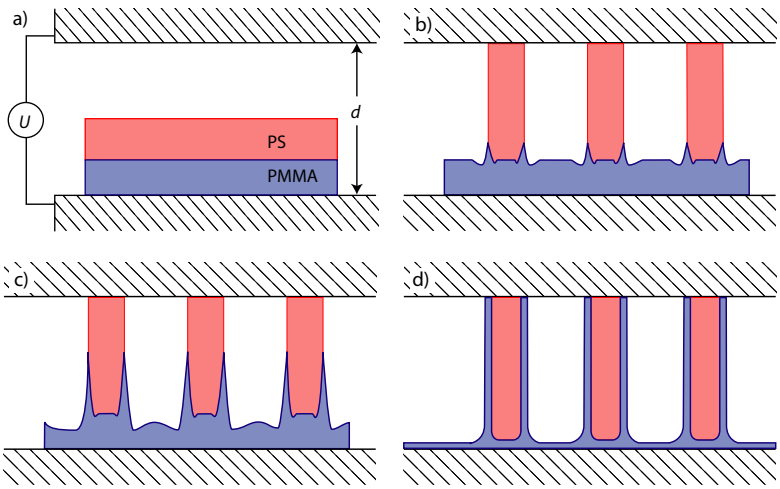

Figure 6.3: Model of the hierarchic structure formation process. a) Starting from a polymer bilayer, the polymer—air surface is first destabilized by an electric field generated by the applied voltage, U. The initial instability results in the formation of columns spanning from the surface of the lower layer to the top electrode. b) During the column–formation process, the bottom polymer layer is deformed at the polymer–polymer—air contact line. c) In a secondary instability, the deformation of the lower layer is enhanced by the electric field, driving the polymer upward on the outside of the columns. d) In the final configuration, the polymer of the lower layer has formed a mantle around the primary columns.

cedure, making the replication more complex and less reliable. To overcome such disadvantages we developed a replication process that simultaneously structures multiple materials. By exposing a bilayer of two different polymers (polystyrene and polymethylmetacrylate) to an electric field perpendicular to the dielectric interfaces, electrohydrodynamic instabilities at both polymer surfaces produced a hierarchic lateral structure.

Instabilities at both polymer–air and polymer–polymer interfaces were also studied previously [2, 3, 4]. The structure formation stemming from a combination of dewetting and electrostatic forces was shown to yield a rich pattern

formation process [5]. The forces acting on the dielectric interfaces of the polymer–polymer–air trilayer generates instabilities at these interfaces with different characteristic time constants. Consequently, the interfaces are destabilised at different times, leading to a lateral redistribution of both materials. The resulting hierarchy of length scales in these structures can be harnessed in a novel lithographic technique. The formed structures exhibited two independent characteristic dimensions: one dictated by the master electrode and a second one dictated by the instability of the bottom polymer layer.

Our approach is schematically shown in Fig.(6.3). Thin films of poly methyl methacrylate (PMMA) ($M_w = 90\,\mathrm{kg/mol}$, $M_\mathrm{w}/M_\mathrm{n} = 1.07$) and polystyrene (PS) ($M_w = 100\,\mathrm{kg/mol}$, $M_\mathrm{w}/M_\mathrm{n} = 1.06$) with thicknesses of 150 nm and 100 nm, respectively, were spin–coated from 3% solutions in toluene onto highly polished silicon wafers. The substrates were cleaned prior film deposition with "Snow–jet" and then immersed for 30 minutes in "Piranha" solution, followed by a thorough wash in Millipore water.

The PS film was floated onto a pool of deionized water and then transferred onto the PMMA layer to form a PS/PMMA bilayer. The sample was subsequently placed into an oven at 70° C for two hours to remove the residual water. A silicon wafer (planar – as in Fig.(6.3a) – or with a design topography) was mounted facing the polymer bilayer, leaving an air–gap. To facilitate the disassembly of the device, a self–assembled organic monolayer was deposited onto this wafer prior to the experiment. It also ensured that no polymer remained on this electrode after disassembly. The distance d between the electrodes typically varied by a few micrometers over a lateral distance of 1 cm, giving rise to a wedge geometry. The assembly was placed between two pieces of copper, which were connected to a voltage–stabilized power supply. To facilitate good electrical contact between the copper electrodes and the silicon plates, the backside of the wafers were coated with a thin gold layer ($\approx 100\,\mathrm{nm}$) and then covered with electrically conducting paste.

The capacitor assembly was placed into an oven set to a temperature of 170° C for approximatively 24 h at an applied voltage of 50 V, corresponding to an electric field of $\sim 1 \times 10^8\,\mathrm{V/m}$. To obtain a snap–shot of the formed structure, the sample was rapidly quenched to room temperature before removing the electric field. The sample was analyzed by optical microscopy (Olympus optical microscope BX60) and tapping mode atomic force microscopy (AFM) (Digital Instruments D3100) directly after device disassembly. These images

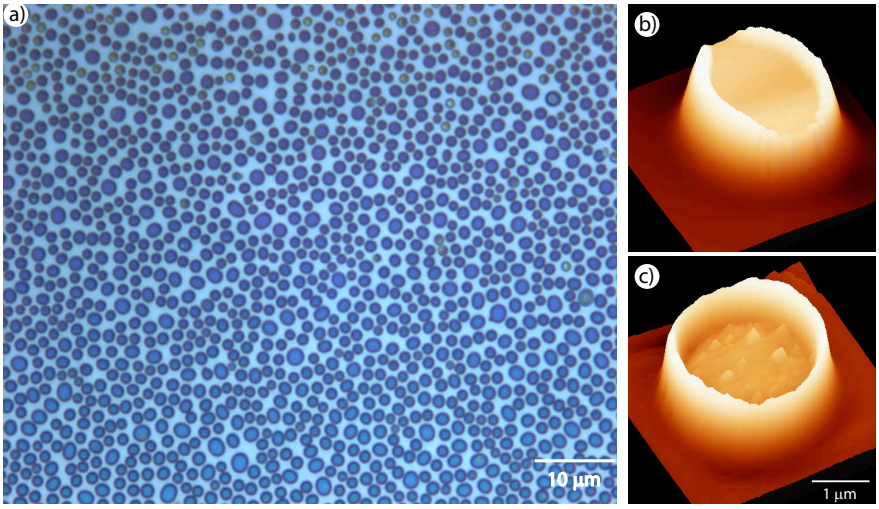

Figure 6.4: Instabilities of a PMMA–PS–air trilayer in an electric field. a) Low-resolution optical micrograph showing an overall columnar morphology. The AFM images in b) and c) show a single column before and after removing the PS phase by washing the sample in cyclohexane. The PMMA phase in b) forms a mantle around the PS column with a height of $\sim 170\,nm$ *and a width of* $\sim 200\,nm$.

reflected the lateral distribution of both PS and PMMA on the substrate. Subsequently, the PS was removed by washing the sample in cyclohexane (good solvent for PS, but not for PMMA) for $\sim 3\,h$ at 35° C. The distribution of the remaining PMMA structure could then be determined independently. A typical image of a polymer bilayer that was heated between planar electrodes is shown in Fig.(6.4a).

When using a planar electrode, the lateral distribution of the polymers was similar to Fig.(6.1). Fig.(6.4a) represents a low magnification optical micrograph of the electric field "molded" columns that span the two electrodes. The AFM scan of a single column in Fig.(6.4b) shows a distinct rim which does not exist when using a single–layer film. Washing the sample in cyclohexane significantly enhances the rim and reveals that the composition of the columns consist of a cylindrical PS core surrounded by PMMA. Fig.(6.4c) shows the

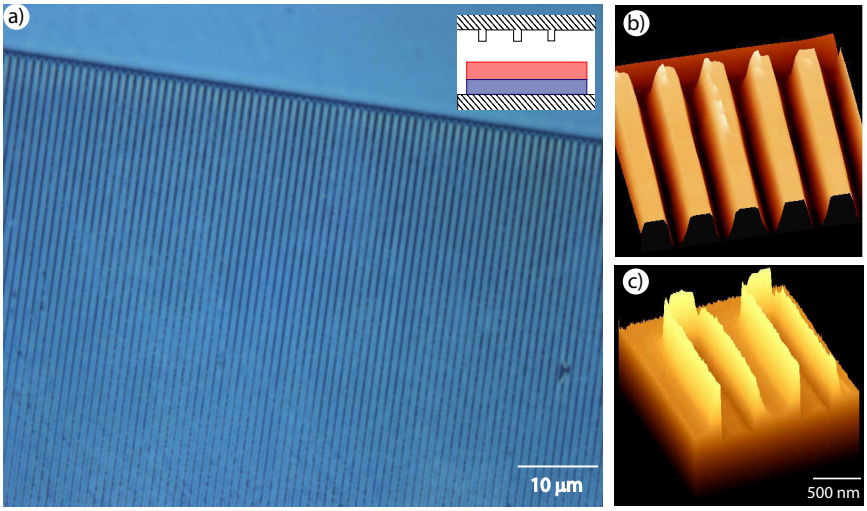

Figure 6.5: Pattern replication by a hierarchical instability. By using a topographically structured electrode (inset in a), the structure-formation process shown in Fig.(6.4) can be controlled to laterally replicate the structure of the electrode. The optical micrograph in a) shows an overview of a line pattern replicated by the electrohydrodynamic instability. The AFM image in b) shows five replicated lines. After removing the PS phase by washing the sample in cyclohexane, the secondary PMMA structure is revealed in the scanning electron micrograph in c) (height: 160 nm, width: ∼ 100 nm).

column after PS removal. The width of the PMMA shell (∼ 200 nm) was significantly smaller than the overall column diameter of ∼ 3.4 μm.

The structure formation of the columns in Fig.(6.4a), can be understood in terms of a sequential electrostatic destabilization of the polymer bilayer. The process is schematically depicted in Fig.(6.3a–d). The upper PS layer destabilizes initially, forming columns that span from the surface of the lower layer to the upper electrode. As the PS retracts into the columns, the PMMA layer is exposed to air. At the polymer–polymer–air contact line the PMMA film is deformed. These deformations nucleate a secondary instability causing the material of the lower layer to "climb–up" along the primary PS columns.

To determine which layer is destabilized first, the force balance at both

interfaces and the hydrodynamic flow in both films have to be considered. Both the PMMA–PS interface and the PS–Air surface are destabilized by the applied electric field. According to Eqn.(2.48) in Section 2.3.3 of this thesis, the characteristic time constants τ for the PS–PMMA and PS–air interfaces determine which interface is destabilized first. τ depends on two factors: (i) the force balance at the interface and (ii) the flow of material in the polymer layers, characterized by the polymer viscosities.

From Eqn.(2.35) in Section 2.3.2, the destabilizing electrostatic pressure at the PS–air surface is larger than at the PS–PMMA interface. This difference in the destabilizing force is compensated by a larger restoring force at PS–air surface. The stronger stabilizing force is due to the larger surface tension at polymer–air interface compared to the polymer–polymer interface. The hydrodynamic response of the two layers is also different. To destabilize the PS–air interface, the viscous flow is required only in the PS layer. A deformation of the PS–PMMA interface implies however a hydrodynamic response in both polymer layers. Therefore, the PS–PMMA instability has a much larger value of τ (several days for our experimental parameters) compared to the free surface, which destabilizes after a few hours [4]. Consequently, during the initial phase of the film instability, the PS layer is destabilized by the electric field, whereas the instabilities at polymer–polymer interfaces are strongly damped and the PMMA film remains essentially flat.

The initial undulations of the PS–air surface grow to form columns that span the two electrodes. During the PS column formation process, a PS/PMMA/Air contact line is formed, which moves laterally during the transition from the undulatory to the columnar phase. Because the lateral movement of the contact line generates high viscous stresses, the column formation process is accompanied by a local deformation of the lower PMMA layer at the contact line. This situation, illustrated in Fig.(6.3b) is similar to the dewetting of PS on PMMA [6, 7]. The local deformation of PMMA should, however, be larger in our case, due to an increased acceleration of the PS by the electric field.

Once the PS columns are formed and the PMMA substrate was exposed to air, a less damped instability (with a much lower time constant) of the PMMA surface is possible. The instability is nucleated at the locations where the electrostatic pressure is highest. This is the case at the peaks of the PMMA cusps which are adjacent to the PS columns, where the destabilizing driving

force is largest. As a consequence, the electrostatic force leads to an increase in PMMA cusp height, that is, the PMMA is drawn upward along the perimeter of the PS columns. The final morphology consists of PS columns coated by a layer of PMMA (Fig. 6.3d). We expect a thin layer of PMMA to cover the entire substrate, because PMMA wets the silicon substrate better than PS. However, this film is not favorable in terms of its electrostatic energy and its equilibrium thickness is dictated by the balance of the free energy that favors wetting and the electrostatic energy.

The reduction in structure size is given in terms of a volume conservation argument. Per unit area λ^2 the volumes of the primary and secondary structures are given by $\lambda^2 h = CV_{\mathrm{PS}}$ and $\lambda^2 H = CV_{\mathrm{PMMA}}$, respectively, where h and H are the initial layer thicknesses (see Fig. 6.3), V_{PS} and V_{PMMA} are the volumes of the final structures (columns) and C is a numerical constant corresponding to the number of columns per unit area λ^2. For the cylindrical morphology in Fig.(6.4), $V_{PS} = \pi r^2 d$ and $V_{\mathrm{PMMA}} = \pi(R^2 - r^2)d$ with r and R the radii of the PS and the composite (PS+PMMA) columns, respectively. From these simple equations, the reduction in lateral structure size is readily calculated:

$$\frac{R-r}{r} = \sqrt{1 + \frac{H}{h}} - 1 \tag{6.1}$$

This argument is valid only in the absence of the PMMA layer between the columns. In our case, because the system did not reach its equilibrium, not all PMMA was drawn into the structures. Therefore, because of the presence of a laterally homogeneous PMMA layer (Fig. 6.4), H must be replaced by $H_{\mathrm{i}} - H_{\mathrm{f}}$ where i and f refer to the initial and the final averaged PMMA film thickness, respectively. The reduction factor of $(R-r)/r \approx 0.12$, derived from Fig.(6.4) corresponds to a remaining PMMA film thickness of $H_f \approx 12.5\,\mathrm{nm}$.

The sample morphology formed in an electric field is far from its field–free thermodynamic equilibrium. This applies both to the PS columns and the PMMA surrounding structures. Except for very small aspect ratios, columns are not thermodynamically stable and are expected to decay via a Rayleigh instability in the absence of an applied electric field. Once formed, the columns continue growing by drawing material from the surrounding polymer layer. However, the lateral coarsening of the columnar morphology is suppressed if the columns are not connected by the laterally homogeneous film [2]. In

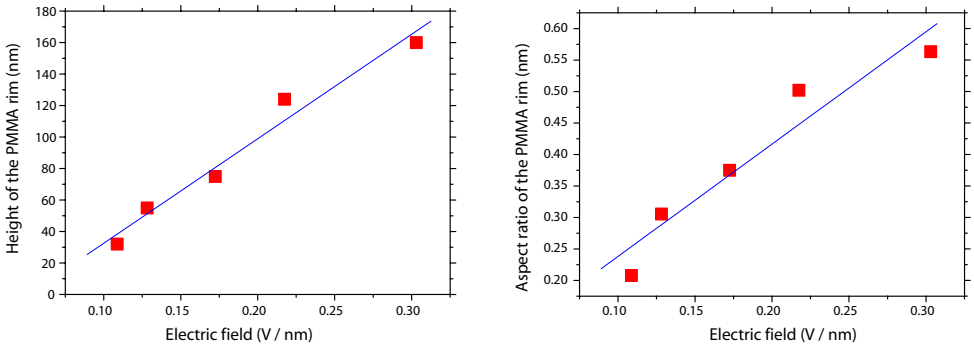

Figure 6.6: Dependence of the secondary instability on the electric field. a) Height of the PMMA rims as a function of the total applied electric field U/d (annealing time: 18 h). b) aspect ratio (height/width) of the PMMA rims as a function of the total electric field. The lines are linear fits.

addition, a PMMA layer that covers the PS–air interface is unfavorable, since PS has a slightly lower surface energy and is known to segregate to the air surface.

Once the destabilization mechanism is understood, the hierarchical structure formation can be tailored [2]. Fig.(6.5) shows results where the planar top electrode was replaced by a topographically patterned silicon wafer (schematically shown in the inset). Here, the variation in the plate spacing d causes a lateral variation in the electric field. Such an inhomogeneous field has two consequences. First, the capillary instability is focused toward the regions of highest electric field, i.e. toward regions where $d - (H + h)$ is smallest. The liquid polymer is drawn toward the downward extending protrusions of the top plate. Second, the characteristic time constant τ associated with the capillary instability is short in regions of small air–layer thickness. Eqn.(2.48) shows that τ decreases strongly with decreasing electrode spacing d ($\tau \approx d^{-6}$ corresponding to an increase in the electric field $\tau \approx E^6$), causing a significantly earlier onset of the instability beneath the protrusions of the patterned electrode. This leads to a replication of the 1 μm–wide lines in Fig.(6.5).

In Fig.(6.5b), a higher magnification AFM image of the transferred line pattern is shown. After disassembly of the capacitor device, a perfect replica-

tion of the master electrode is revealed, similar to the case of a single polymer layer [2]. After removing the PS by washing the sample in cyclohexane, the PMMA structures are revealed. The secondary instability generated 100 nm wide and 160 nm high structures at the edges of the replicated lines (Fig. 6.5c). The hierarchic structuring process can be explained in a similar way as the planar electrode case. The PS–air surface is destabilized initially and the PS is drawn toward the downward protruding lines, thereby replicating the master electrode. The PS line formation (*i*) produces free PMMA surface areas and (*ii*) causes a viscous deformation of the PS/PMMA/air contact line. The secondary instability of the PMMA–air interfaces causes a flow of PMMA to cover the PS lines.

The height and width of the PMMA structures (and therefore their aspect ratio: height/width) are determined by the electrode spacing d, the lateral density of topographic features on the master wafer, and the initial film thickness of the PMMA layer. Because the PMMA is redistributed from a film into lateral structures spanning the electrodes, the width of these structures is determined by a volume conservation argument. Similar to the discussion above, $(R-r)/r = (H_i - H_f)/h \approx 0.1$, where r and R correspond to the half–width of the PS and PS–PMMA composite lines, respectively. Both our experimental results and the volume–conservation argument imply that the aspect ratio of the PMMA lines can be adjusted by varying either the thickness of the initial PMMA layer or the annealing time.

In practice, we found that achieving the final state (Fig. 6.3d) occurred only after very long times (for our experimental system, equilibration was not achieved even after several days). The time needed for the structures to develop can be significantly reduced by decreasing the molecular weight (and thereby the viscosity) of the PMMA layer. A second approach is to increase the electric field, with the occurrence of dielectric break–down of the polymer as a limiting factor. Fig.(6.6) shows a linear vertical growth of PMMA structures (all annealed at an applied voltage of 50 V for 18 h at 170° C) as a function of the electric field. A third approach to achieve the final state shown in Fig.(6.3d) would be to increase the temperature. However, the working temperature (170° C) is already close to the degradation temperature of the polymers in air ($\approx 210°$ C) therefore, vacuum should be applied.

Finally, the reliability of this structure replication technique must be emphasized. A structured $200 \times 200\,\mu m^2$ area is shown in Fig.(6.7). Apart from

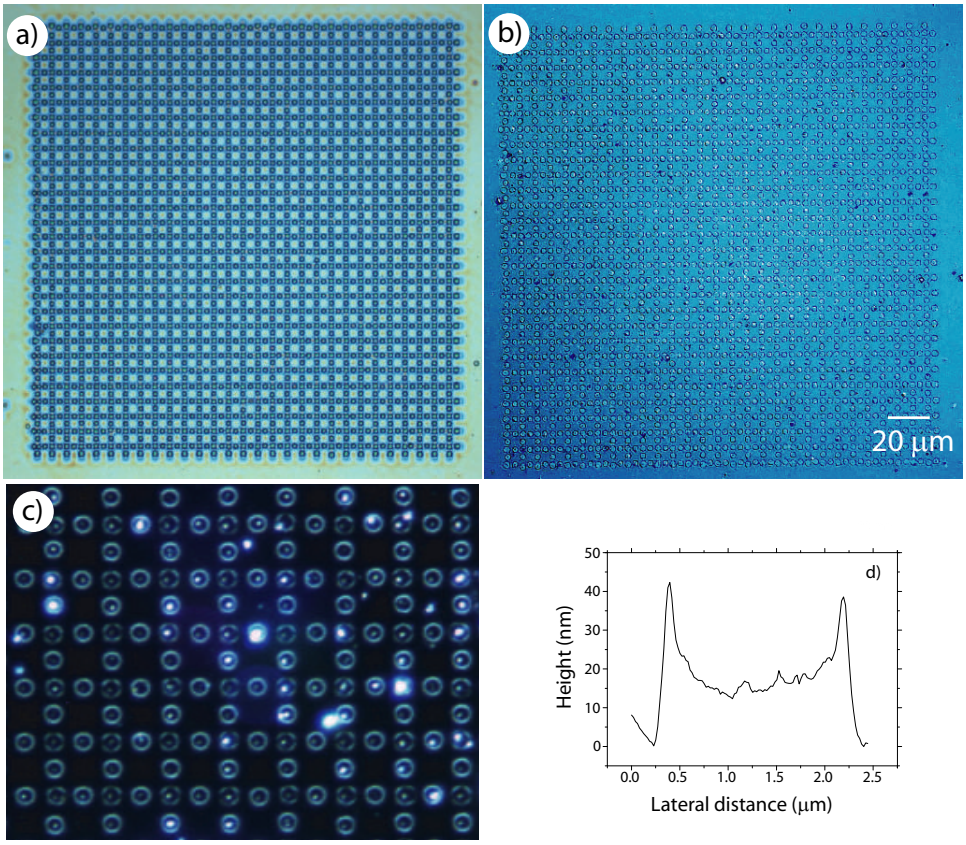

Figure 6.7: Large-area images of replicated patterns. To illustrate the fidelity of the replication process, optical micrographs of a $200 \times 200\,\mu m^2$ replicated area are shown. The area consists of spherical cylinders arranged on a square lattice, with cylinders at each vertex and in the middle of the lines connecting the vertices. The image in a) taken immediately after the disassembly of the capacitor, shows a replicated film containing both PS and PMMA. After the removal of PS, an ordered array of PMMA rings remains on the substrate b). The magnified image in c) was obtained using dark-field illumination to enhance the optical contrast. In d) an AFM cross-section of one of the PMMA rims is shown.

isolated defects (caused by dust), the pattern of the master electrode was reproduced with high fidelity. Washing away the PS, a similar quality of the PMMA secondary structure was found. With properly aligned electrodes, structure replication can therefore be extended to very large areas.

6.4 Conclusion

In summary, a novel electric field–induced structure formation process in polymer bilayers is described. Structure formation occurs by the sequential growth of electrohydrodynamic instabilities that result in the formation of hierarchal patterns with two independent characteristic lateral dimensions. In particular, the secondary instability leads to structure widths that can be significantly smaller (by about a factor of 10) than the primary structure size. When combined with a topographically patterned electrode, this strategy can be used to replicate $\sim 100\,\mathrm{nm}$ size structures, much smaller than the pattern size of the master. Two materials can be patterned in a one-step procedure, instead of a multi-step process used by other lithographic techniques. This approach can be extended to lateral hierarchical structures consisting of a larger number of different materials and more than two independent lateral length scales.

Bibliography

[1] Presented in the chapter regarding "Capillary Instabilities by Thermal Fluctuations"

[2] E. Schäffer, T. Thurn–Albrecht, T.P. Russell, U. Steiner; *Nature* **403**, 2000

[3] E. Schäffer, S. Harkema, M. Roerdink, R. Blossey, U. Steiner; *Adv. Mater.* **15**, 2003

[4] Z. Lin, T. Kerle, S. M. Baker, D. A. Hoagland, E. Schäffer, U. Steiner, T. P. Russell; *J. Chem. Phys.* **114**, 2001.

[5] Z. Lin, T. Kerle, T. P. Russell, E. Schäffer, U. Steiner; *Macromolecules* **35**, 2002

[6] P. Lambooy, K.C. Phelan, O. Haugg, G. Krausch; *Phys. Rev. Lett.* **76**, 1996

[7] C. Wang, G. Krausch, M. Geoghegan; *Langmuir* **17**, 2001

Chapter 7

Capillary Instabilities in a Polymer Blend Film Driven by Surface Tension Gradients

7.1 Introduction

The influences of surface tension gradients on the hydrodynamics and mass transfer in fluid systems are often termed as the "Marangoni Effect". Thin liquid films, are easily deformed by material heterogeneities and thermal fluctuations. Because these perturbations influence the long term stability and the qualitative structure of the film, a better understanding of these effects is required. The study of the surface–tension–gradient induced flow is pertinent to various applications where interfacial flows are encountered, such as in lubrication and coating processes. Moreover, surface–tension–driven flow is an interesting and important fundamental problem of fluid dynamics.

The physical basis for the deformation of a liquid surface by surface tension

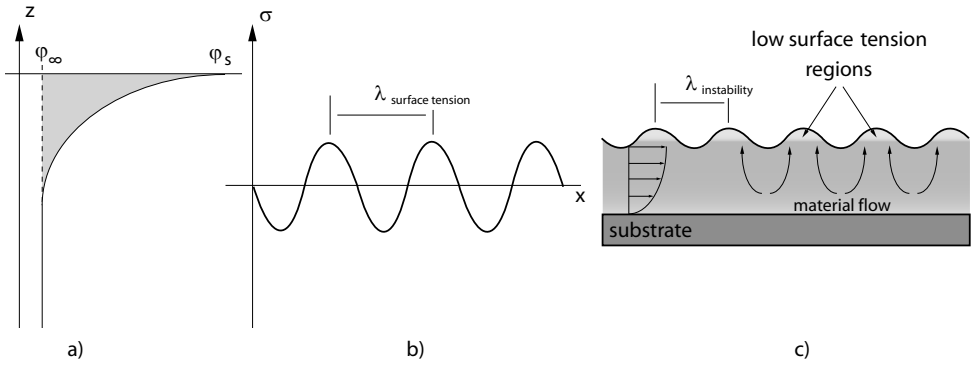

Figure 7.1: a) Variation of the average composition normal to the film surface. Due to the surfactant behavior of PVME, φ varies from φ_s at the surface to φ_∞ in the bulk. The gray area represents the enrichment of PVME at the surface. b) Model for the composition fluctuations of the surface tension in lateral direction. One mode with a $\lambda_{\text{surface tension}}$ is shown. c) The effect of the surface tension heterogeneity on the stability of a polymer film. The stresses induced at the interface by surface tension gradients give rise to material flow towards regions of high surface tension.

gradients was first developed by Gibbs [1]. Heat or mass transfer in liquids are nonequilibrium phenomena, often giving rise to instabilities, which lead to the formation of dissipative structures [2, 3]. This type of instabilities was investigated in many papers and monographs [4] especially at the liquid surface where these instabilities manifest themselves as a flow induced by surface tension gradients. An important precondition for the occurrence of such unstable modes is the existence of heat or mass transfer in the liquid layer, which results in temperature or concentration gradients in the region close to its surface. In this case, a surface tension gradient can arise due to this temperature or concentration dependence. The liquid layer becomes unstable due to normal [5, 6] as well as lateral [7, 8, 9] flows and gradients.

In thin films made of polymer blends, lateral phase separation often results in composition–dependent surface morphologies [10]. When a polymer blend is in one phase region close to its critical temperature, composition fluctuations are significant. In addition, thermally–excited surface undulations affect the

morphology of thin polymer films (see Chapter 5 of this thesis). In our case, composition fluctuations that give rise to surface tension gradients ($\Delta\sigma$), are mainly due to the mass transfer from the bulk to the film surface. Due to the small film thicknesses, temperature gradients across the film and surface elasticity influence on the surface tension can be ignored.

To study surface instabilities of polymer blend films, mixtures of polystyrene (PS) and poly(vinyl methyl ether) PVME were deposited onto chemically homogeneous silicon wafers. PS/PVME blends are known to be homogeneous at room temperature but to demix at higher temperatures, exhibiting a lower critical solution temperature (LCST). Kim et al. [11] found that the critical composition of the blend exhibits concentration fluctuations in the homogeneous regime close to the LCST. The extent of these fluctuations is inversely proportional to the absolute value of the temperature coefficient B in the Flory interaction parameter

$$\chi = A + \frac{B}{T}$$

Several authors have studied the properties of the polymer/air interface of miscible PS/PVME blends. The parameters considered were blend composition, molecular weights and temperature. They demonstrated that PVME is enriched at the free surface, exhibiting a strong surfactant behavior that reduces the surface tension. Schmidt–Rohr et al. reported that on the scale of polymer segments, the PS/PVME blends are not completely mixed. The blend is neither homogeneous nor strictly phase separated but nano–heterogeneous. This was shown experimentally by performing a two–dimensional NMR spectroscopic study. Shimizu et al. investigated these domains for high molecular weight PS ($M_n \sim 50\,\mathrm{Kg/mol}$). Their experiments indicated that the blend structure has a percolation–like morphology similar to typical structures observed in spinodal decomposition. Additionally, they demonstrated that the domain size depends strongly on the molecular weight of the blend components.

This chapter focuses on a new type of instability that develops spontaneously in a PS/PVME polymer blend film. From an experimentally point of view, we observed the instability and measured its wavelength versus film thickness and blend composition. Furthermore, we were able to direct and manipulate the instability in a lithographic process.

Table 7.1: *Critical and annealing temperatures of different blend compositions.*

Blend composition	T_d ° C	T_g ° C	T_w ° C
10%PS – 90%PVME	45 ± 2	-28.53	35
20%PS – 80%PVME	40 ± 1.5	-23.39	28
40%PS – 60%PVME	45 ± 2	-10	30
50%PS – 50%PVME	50 ± 2.5	-2.24	35
60%PS – 40%PVME	55 ± 2	4	40
80%PS – 20%PVME	70 ± 2.5	13.41	65

T_d Demixing temperature.
T_g Glass transition temperature of the blend.
T_w Working temperature.

7.2 Experimental Section

A schematic description of our experimental setup is shown in Fig.(7.1c). PS ($M_w = 32\,\mathrm{kg/mol}$, polydispersity $M_w/M_n = 1.02$) and PVME ($M_w = 52\,\mathrm{kg/mol}$, $M_w/M_n = 1.04$) were used as received. Films of mixtures with volume fractions φ ranging from $\varphi_{PVME} = 0.2$ to $\varphi_{PVME} = 0.8$ were spin–coated from a toluene solution onto silicon wafers. Prior to deposition, the substrates were cleaned in a jet of CO_2 crystals ("snow–jet"). Subsequently, the substrates were immersed in a hot (∼80° C) Piranha solution[1]. The samples were annealed at $T - T_g(\varphi)$=const., the condition of constant chain mobility. The annealing temperatures were below the binodal curve of the blend to prevent the demixing of the two components. Their values are given in Table 7.1 together with the demixing (T_d) and glass transition temperatures (T_g) of the blends for the range of compositions used in this study.

Our blend exhibited a lower critical solution temperature of 40° C at a

[1]The "Piranha" solution consists of a mixture of hydrogen peroxide and sulphuric acid in a ratio of 1/3 w/w.

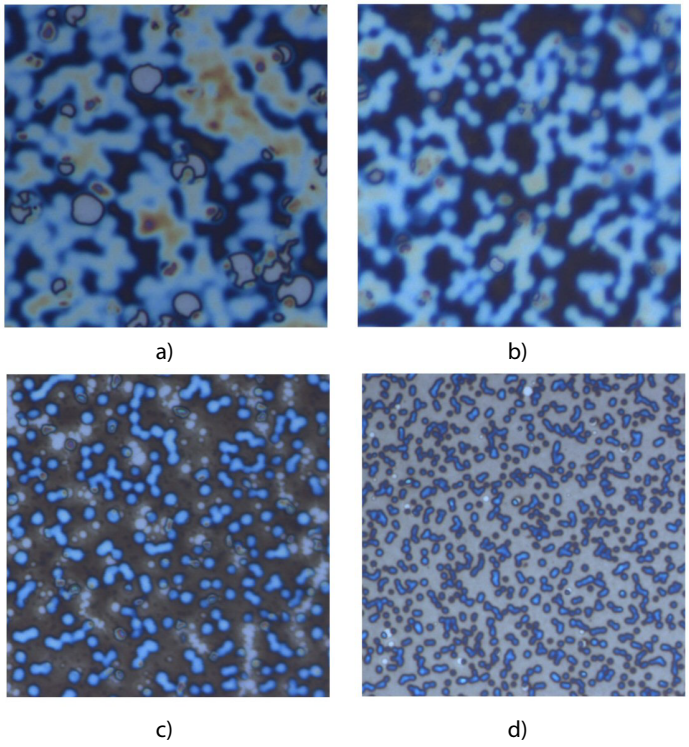

Figure 7.2: Optical micrographs ($50 \times 50\,\mu m^2$) showing unstable morphologies of a 40%PS–60%PVME blend annealed at 40° C for four film thicknesses. (a) 310 nm; (b) 270 nm; (c) 135 nm; (d) 80 nm;

critical composition of $\varphi_{\mathrm{PVME}} = 0.8$. The experiments were performed in a glove box with a water vapor concentration of less than 1 ppm. This was necessary because PVME is highly hygroscopic. Thin films with thicknesses ranging between 60 nm and 310 nm were prepared by spin coating. The sample morphology was followed during heating using a Mitutoyo WF reflection microscope and the images were recorded with a Carl–Zeiss digital camera. A DI Dimension 3100 AFM was used in tapping mode to acquire topographic and phase micrographs after cooling the sample to room temperature.

We studied the film instability when the blend was in a mixed state, bellow

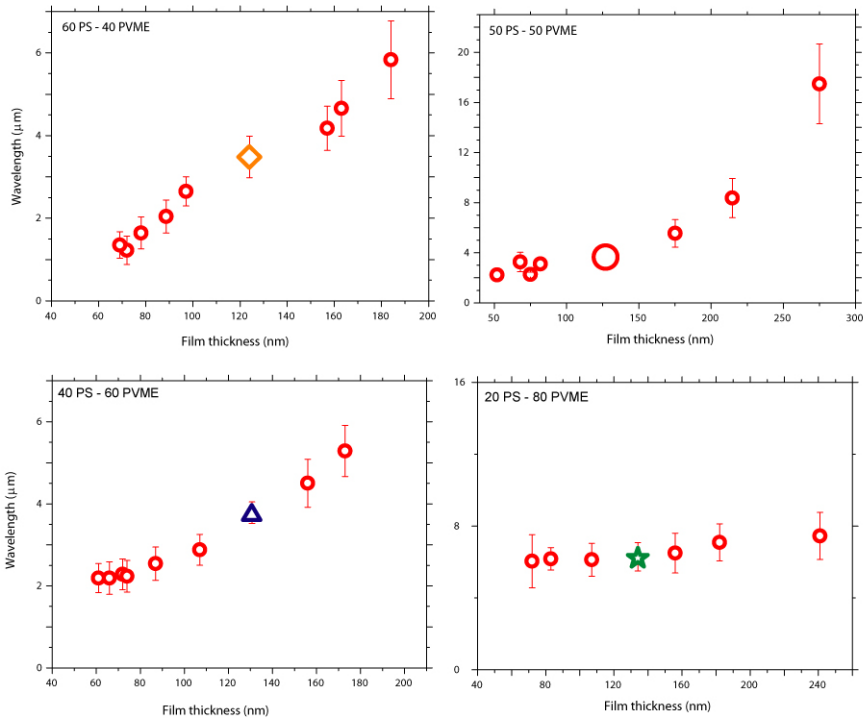

Figure 7.3: Wavelength vs. film thickness for four blend compositions.

its critical temperature. Because the blend was above its glass transition temperature (T_g), its composition fluctuates with time. These fluctuations occur in the bulk as well as at the surface. In the bulk, the fluctuations relax by diffusion while at the surface, they induce surface tension gradients. Short wavelength composition fluctuations are unlikely to destabilize the free interface because can easily decay by diffusion processes. On the other hand, long wavelength fluctuations build up surface stresses causing flow of bulk material towards regions of high surface tension. If the hydrodynamic response is faster than diffusion, a capillary instability sets–in and breaks–up the thin polymer film.

First, the influence of the film thickness on the morphology of the blend was studied, keeping the composition of the mixture constant. In Fig.(7.2) the

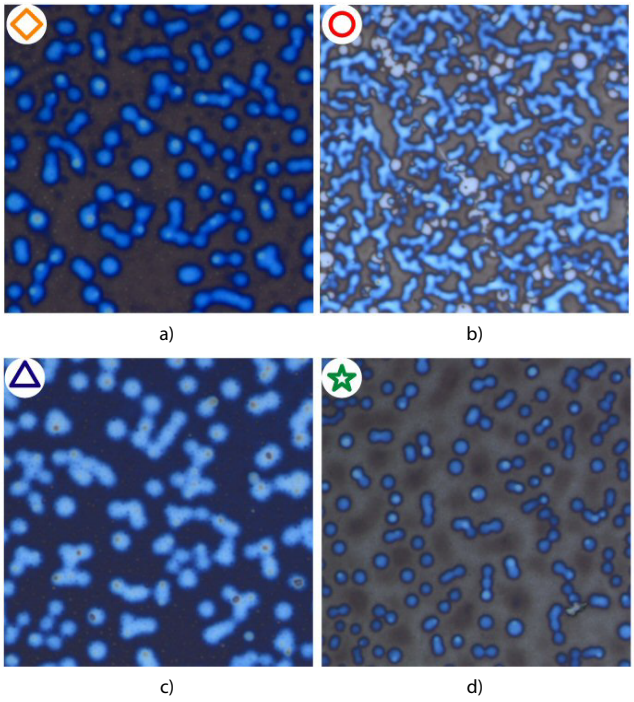

Figure 7.4: Optical micrographs ($50 \times 50\,\mu m^2$) *showing unstable morphologies of a* $\sim$*130 nm thick polymer film for different composition of the polymer blend (a) 60PS/40PVME; (b) 50PS/50PVME; (c) 40PS/60PVME; (d) 20PS/80PVME*

topography of a 40%PS–60%PVME blend is shown as a function of film thickness. The optical images show the spontaneous deformation of the polymer–air interface upon annealing the samples at 30° C. Morphologies similar to those in Fig.(7.2) were observed for the range of blend compositions given in Table 7.1. The wavelength of the instability (λ) was determined by Fourier transformations of such images and plotted versus film thickness (Fig. 7.3). These measurements show that the wavelength increases with increasing the film thickness. Because all the samples were annealed for the same time, an increase in λ due to coarsening is unlikely.

The results may be explained in terms of hydrodynamic arguments. The

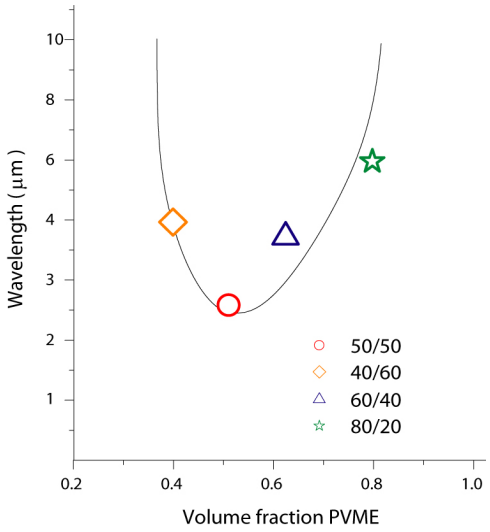

Figure 7.5: Wavelength of the instability vs. blend composition. The continuous line is a guide for the eye.

most amplified wavelength is determined by the coupling between the composition fluctuations and the rheological behavior of the polymer blend. The surface tension gradients caused by composition fluctuations should be independent by the film thickness for all films of identical blend composition. Therefore, we assume that only the rheological behavior influences the wavelength of destabilization. Short wavelength instabilities are strongly damped by the surface tension, while building–up long wavelength oscillations is opposed by the viscous drag of the hydrodynamic flow. Therefore, the characteristic wavelength is dictated by the interplay between the surface tension and the energy dissipation in the polymer film. For thinner films the viscous drag is higher in comparison to thicker films when assuming a non–slip Poiseuille type of flow inside the layer (Fig. 7.1c). Therefore, smaller wavelengths are favored. For thicker films, the hydrodynamic drag decreases and therefore the instability wavelength increases.

In a second class of experiments, we analyzed the influence of the blend composition on the surface morphology. We measured the instability wave-

length for four different compositions (40–60, 50–50, 60–40 and 80–20 PVME–PS), keeping the film thickness constant (∼130 nm). The results are shown in Fig.(7.4).

Analyzing the data from Fig.(7.4), we observed that the wavelength shows a minimum for the symmetric composition 50%PS–50%PVME (Fig. 7.5). Shifting the composition either to smaller or larger volume fractions of PVME resulted in an increase in λ.

This effect may be explained in terms of composition fluctuation arguments. The volume fraction of the PVME varies from φ_s at surface to φ_∞ in the bulk (Fig. 7.1a). Furthermore, the composition fluctuations at the surface induce lateral variations in the surface tension (Fig. 7.1b) which depend by the volume fraction of the PVME at the surface and in the bulk. The largest surface tension gradients are expected for a symmetric mixture, because of the strongest enrichment of PVME at the interface. For other compositions, the enrichment is lower, resulting in weaker lateral surface tension gradients. A smaller gradient implies a weaker stress at the film surface, therefore, larger instability wavelengths. The behavior described above is summarized in Fig.(7.5), where the instability wavelength is plotted versus the volume fraction of PVME.

Theoretically, film instabilities are usually computed by a linear stability analysis. We present here a possible route to compute the instability wavelength. Most film instabilities reported so far, have been predicted essentially by this method. Examples include the Mullins–Sekerka instability in solidification [12], the Saffman–Taylor instability in the viscous fingering problem [13] and the convective Bénard instability [14]. Even though all these instabilities give rise to complex patterns, they are all triggered by infinitesimal perturbations [15]. We refer to these as linear instabilities because they can be explained by a linear analysis. In our case we postulate a coupling of the composition fluctuations with the material flow. To model the system, the Navier–Stokes equation describing the rheological behavior of the system must be used, while a Cahn–Hilliard type equation [16, 17] describes the composition fluctuations in the polymer blend. By solving the resulting system of partial differential equations, the most probable mode has to be computed. However, the solution is impossible to be computed analytically. Due to its great complexity, the system of coupled partial differential equations can be solved only numerically. We are currently performing these calculations, their

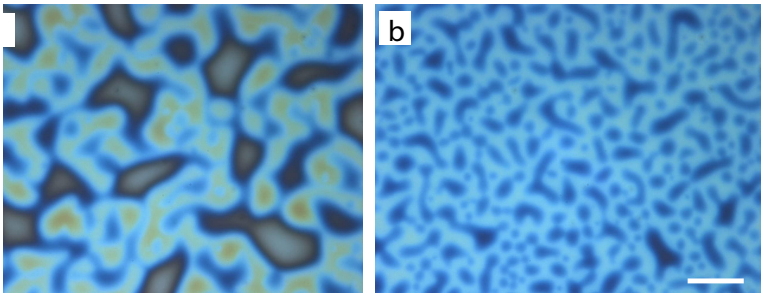

Figure 7.6: Onset of film instabilities of a 110 nm thick PS/ PVME film that was heated to 170 °C for 60 s, (a): confined between two silicon wafers spaced at $d = 308$ nm; (b) no confinement. The undulatory character of the structures is due to a spontaneous surface instability in both cases. The larger amplitude of the surface undulation in (a) indicates an earlier onset of the instability compared to (b), presumably do to differing initial heating rates when placing the sample in the oven. This accounts also for the more coarse grained appearance of the structure in (a) due to a longer coalescence time.

result being the subject of a future publication

7.3 Surface Tension Driven Lithography

By understanding the destabilization process, we were able to harness and use the instabilities in a pattern-replication process. The lithography using electric fields and temperature gradients is robust and versatile but the external interaction with the structure formation process may be a limitation. This disadvantage can be circumvented by making use of film instabilities that are intrinsic to the system. If confined by a topographically structured surface, any undulatory mode of a film instability can be harnessed to induce structure into the film.

A liquid film has a peculiar behavior in a confined environment. Its morphology in the capillary regime is dominated by a minimization of the overall surface free energy. This regime is defined by a characteristic parameter, the

so–called capillary length a

$$a = \sqrt{2\frac{\gamma}{\rho g}} \tag{7.1}$$

quantifying the balance between the surface energy γ and the gravitational acceleration g. In Eqn.(7.1), ρ is the density of the liquid. On a flat, solid surface that is smooth and chemically homogeneous, the shape of the liquid is dictated by the balance of the liquid–vapor, liquid–substrate and substrate–vapor surface free energies [18]. In case of a liquified polymer, the vapor pressure is zero. When the interface between the liquid and a confining solid has a lower energy per unit area compared to the liquid–air and the solid–air surfaces, this leads to liquid morphologies that are not observed for large volumes of liquids. Examples include the capillary rise of a liquid in a narrow tube, the formation a liquid bridge spanning two opposing finger tips, or the fact that large amounts of water are drawn into a granular material (e.g. sand), overcoming the gravitational counterforce.

In the first part of this chapter, we showed that a liquid polymer blend becomes spontaneously unstable due to surface tension gradients. Coupling the effect of capillarity with liquid instabilities (Fig. 7.7) in a confined geometry, the liquid forms capillary bridges. Quenching the liquid polymer film to temperatures below its solidification temperature, the structures can be frozen for further analysis.

7.3.1 The Experimental Situation. Results and Discussions.

The following work was performed by Harkema et al. [19] and is presented here for the sake of completion. Spontaneous surface instabilities in thin PS/PVME polymer blend films were used to create surface patterns. The unstable film was observed in two conditions (Fig. 7.6): in the presence and in the absence of a confinement. Fig.(7.6a) shows an unstable 110 nm thick PS/ PVME film heated to 170 °C, (a) confined to a 308 nm wide slit and (b) in the absence of confinement. The film instability was explained in Section 7.2.

The behavior of the liquid polymer in a confined geometry is schematically depicted in Fig.(7.7). Depending by the initial film thickness h and by the maximal confinement d (i.e. the lowest value of the inter–plate spacing) the final structures of the polymer film can be divided into three regimes [19]. This section focuses only on the case when $d \gtrsim h$ (Fig. 7.7e).

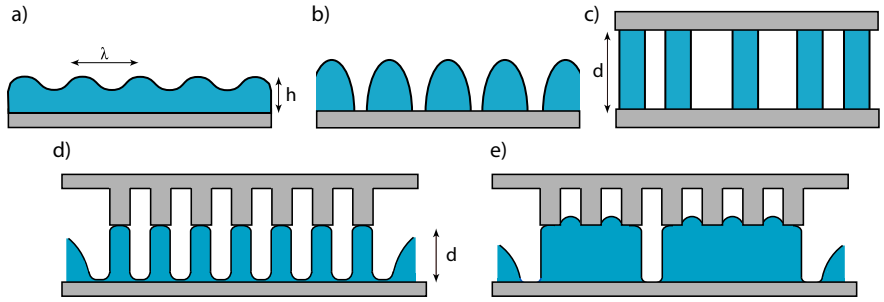

Figure 7.7: Schematic representation of the setup in an (a) unconfined and (c) confined geometry. In the unconfined geometry (b) the film breaks–up into droplets which get pinned by the upper plate (c) forming columns. In the presence of the laterally varying confinement in d), capillary bridging occurs at locations of maximal confinement. This situation does, however, not represent the lowest free energy situation shown in e). In this situation the coalescence of the replicated features in e) is due to the surface tension that tries to minimize the amount of surfaces created.

For $d \gtrsim h$, the initial undulations of the film (Fig. 7.7a) lead to a bridging of the liquid between the two plates (Fig. 7.7c). If the confining plate is patterned (Fig. 7.7d), these bridges form in the regions of greatest confinement, i.e. at the locations where the topographic pattern of the top plate extends down towards the polymer film.

In Fig.(7.8), the replication of a line pattern is shown. The 24 lines of the master are replicated by the formation of capillary bridges – the polymer spans from the substrate to the confining surface. The obtained structure (Fig. 7.8b) is a positive replica of the master (Fig. 7.8a)

A second replicated structure is shown in the AFM images of Fig.(7.9). They correspond to the replicated polymer pattern (Fig. 7.9d) and the confining plate (Fig. 7.9e). The two micrographs clearly show the nature of the replication process as opposed to the cases of imprinting and replication by capillary filling [19], which produce a negative replica of the master electrode. The positive replication of the of hexagon–shaped holes on a triangular lattice clearly shows the novel nature of the replication process.

Replication occurs for two conditions.

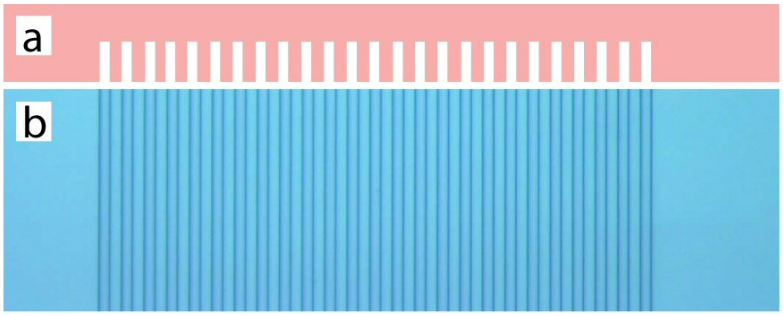

Figure 7.8: The dewetting in a confined geometry. The 24 replicated lines in a) correspond to the 24 downward protruding lines of the master schematically shown in part a). These lines were replicated into the polymer film by capillary bridging ($d/h = 1.4$, $h = 84\,nm$.

- for capillary bridging to take place in a more or less homogeneous fashion, there has to be an approximate matching of the instability wavelength λ and the periodicity of the confining pattern
- per unit area A_0, the volume of the initial film must be laterally accommodated in the replicated structure.

The second condition can be written as

$$\frac{d}{h} \approx \frac{A_0}{A_p}, \tag{7.2}$$

where A_p is the lateral area of the protrusions of the confining surface extending down towards the polymer film (Fig. 7.7c). The first condition has to be fulfilled within an order of magnitude, but also the second condition allows some variation, since a certain degree of lateral under- or overfilling of the pattern is permissible.

To successfully replicate the master pattern, its surface has to be apolar. Highly apolar surfaces are typically not wetted by any liquid, since the coating of the surface by the liquid does not reduce its effective surface energy. In Fig.(7.8) and (7.9), capillary forces that drive the polymeric liquid to completely fill the surface pattern are absent. This enables the formation of the metastable morphologies corresponding to Fig.(7.7e).

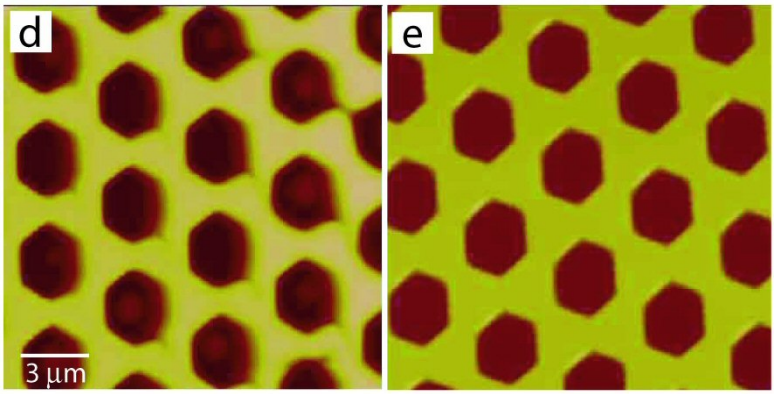

Figure 7.9: Dewetting in a confined geometry. An AFM image of a replicated polymer film, made with the confining surface shown in (e). The positive replica is indicative of replication by capillary bridging.

7.4 Conclusions

In summary, our observations indicate a coupling of the composition fluctuations to the rheological behavior of the polymer film. The two effects strongly influence the resulting morphology. Stresses at the interface generated by composition fluctuations induced surface tension gradients, give rise to a capillary instability. The liquid film responds to these stresses by moving material towards regions of high surface tension. Therefore, the film buckles at a well defined wave number. Eventually, the process causes complete dewetting of the film from the substrate.

In a confined geometry, by suitably choosing the experimental parameters, the undulatory mode of the PS/PVME blend can used to produce positive replicas of a master pattern. While the well-known embossing and capillary filling techniques result in a negative replica of a surface pattern, a novel phenomenon was observed for a confinement with $d \gtrsim h$. In this case, metastable liquid morphologies are formed by the interplay of dewetting and capillary bridging. This lithographic method can prove useful when external interactions with the polymeric material have to be avoided. For example, by using the process of dewetting in a confined geometry, an electrically active polymer

film can be patterned without the use of an external electric field that could damage the polymer.

Bibliography

[1] J.W. Gibbs; *Collected Works* Yale University Press, New York, CT, 1948, Vol.1

[2] P. Glansdorff, I. Prigogine; *Thermodynamic Theory of Structure, Stability and Fluctuations* Wiley, London, 1971

[3] V.I. Kovalchuk, H. Kamusewitz, D. Vollhardt, N.M. Kovalchuk; *Phys. Rev. E* **60**, 1999

[4] S.S. Dukhin, G. Kretzschmar, R. Miller; *Studies of Interface Science* edited by D. Möbius and R. Miller, Elsevier, Amsterdam, 1995

[5] J.R.A. Pearson; *J. Fluid Mech.* **132**, 1958

[6] C.V. Sternling, L.E. Schriven; *AIChE J.* **5**, 1959

[7] M.K. Smith, S.H. Davis; *J. Fluid Mech.* **132**, 1983

[8] D. Schwabe, U. Möller, J. Scheinde, A. Scharmann; *Phys. Fluids A* **4**, 1992

[9] W. Schöpf, J.C. Patterson; *J. Fluid Mech.* **295**, 1995

[10] S. Walheim, M. Böltau, J. Mlynek, G. Krausch, U. Steiner; *Macromolecules* **30**, 1997

[11] J.K. Kim, H.W. Son; *Polymer* **40**, 1999

[12] W.W. Mullins, R.F. Sekerka; *J. Appl. Phys.* **3**, 1964

[13] P.G. Saffman, G.I. Taylor; *Proc. R. Soc. London A* **245**, 1958

[14] S. Chandrasekhar; *Hydrodynamics and Hydromagnetic Stability*; Dover, New York, 1961

[15] H. Guo, D.C. Hong, D.A. Kurtze; *Phys. Rev. Lett.* **69**, 1992

[16] J.W. Cahn, J.E. Hilliard; *J. Chem. Phys.* **28**, 1958

[17] J.W. Cahn, J.E. Hilliard; *J. Chem. Phys.* **31**, 1959

[18] T. Young; *Phil. Trans. Roy. Soc.* **15**, 1805

[19] S. Harkema, E. Schäffer, M.D. Morariu, U. Steiner; *Langmuir* **19**, 2003

Chapter 8

Conclusions

The subjects investigated in this thesis center on the pattern formation in thin polymer films. A multitude of surface morphologies can be generated by the amplification of capillary waves in external fields or by the spontaneous destabilization of the liquid surface due to surface tension gradients. We were interested in both applied and fundamental aspects of structure formation on micrometer and nanometer length scales.

The spontaneous break–up of polymer films of thicknesses less than 10 nm is commonly attributed to the destabilizing effect of van der Waals forces. These forces can be considered in terms of the confinement of the electromagnetic fluctuation spectrum. The consideration of the confinement of thermal fluctuations (phonons) leads to an acoustic analogy of the van der Waals pressure. We showed that forces stemming from thermally excited acoustic fluctuations (thermal noise) in thin films, give rise to a disjoining pressure that is comparable to van der Waals forces. Under certain conditions, the acoustic effect is the dominating destabilizing force.

To demonstrate the presence of the thermo–acoustic destabilizing pressure we investigated the characteristic patterns in thin liquified polymer films. Because the spectrum of spontaneously amplified waves is very sensitive to

the detailed force balance acting at the surface of the film, we were able to quantify the magnitude of the destabilizing force by measuring the instability wavelength. We performed three sets of experiments that used polymer films bounded between a substrate and air, in a manner that unambiguously pointed out the presence of the acoustic pressure.

In the first class of experiments, we found a variation of the film destabilization with temperature, in contradiction to predictions based exclusively on a van der Waals theory. In the second approach, we chose a system in which p_{ac} and p_{vdW} pressures had opposing signs. The experiments showed the distinct signature of a capillary instability even though the van der Waals forces were stabilizing the polymer films. The third experiment involved the variation of the acoustic boundary conditions. By suitable choosing the substrates and films we demonstrated that the acoustic pressure could be switched on and off as a function of the acoustic boundary conditions. As a consequence we were able to destabilize films that should otherwise be stable.

For hundreds of nanometers thick films, van der Waals forces are to weak to influence the film stability. In the absence of any other external force, polymer films can become spontaneously unstable and break–up by other mechanisms. We demonstrated that a polymer film containing a macromolecular surfactant shows a surface instability when heated above its glass transition temperature. Our model system was a binary blend of polystyrene and poly(vinyl methyl ether). PVME has a much lower surface tension than PS and forms an enrichment layer at the surface. Composition fluctuations at the surface led to a variation of the surface tension. The response to the lateral gradient in the surface tension was the flow of material towards regions with highest surface tension (Marangoni flow). Analyzing the instability wavelength versus the film thickness and composition, we demonstrated the interplay between the surface tension gradients and the hydrodynamic response of the thin film.

A further way to induce and control the structure formation process is to use externally applied electric fields. The destabilization is caused by the much stronger electrostatic force. Opposed by the surface tension, the instability shows a characteristic wavelength. Using a polymer bilayer, the polymer–polymer and polymer–air interfaces are destabilized at different times. We used the sequential destabilization of a polymer bilayer to induce a hierarchical structure formation in a process. By using a topographically structured electrode, we imposed a lateral force modulation, thereby focusing the insta-

bilities towards regions of high electric fields. The field modulation resulted in the formation of hierarchical patterns with primary and secondary independent lateral dimensions. The secondary instability led to structure widths significantly smaller (by about a factor of 10) than the primary polymer–air instability. Washing away the upper polymer layer, the remaining structures were in the range of ∼100 nm, much smaller than the pattern size of the master electrode. The advantage over the simple EHD technique is that two materials can be patterned in a single–step procedure instead of several steps used in other lithographic techniques. Our approach could be in principle extended to lateral hierarchical structures consisting of a larger number of different materials and more than two independent lateral length scales.

Harnessing the demixing process of a polymer blend opens new routes to produce nanostructured materials. We developed a method to manufacture nanoporous hard films with improved optical properties. The technique we applied was based on the demixing of a binary polymer blend during spin-coating. One of the polymers was replaced by an inorganic phase produced by a sol–gel approach. After film deposition, the organic phase was removed by washing the sample in a good solvent for the polymer. The resulting nanoporous film had broad–band antireflective properties and improved mechanical strength. We were also able to coat plastic substrates with these hard AR coatings. A homogeneous SiO_x film was used to increase the adhesion of the nanoporous film to the plastic substrate. By fluorinating the surface of our coatings, an improved cleanability was obtained. Surfaces coated with these films exhibited an outstanding optical transmission ($T > 99\%$ averaged from 400 to 680 nm). In particular, for the reference wavelength ($\lambda = 600$ nm), a transmission $> 99.8\%$ was achieved.

The investigated subjects still pose fundamental problems or experimental challenges. Our predictions regarding the thermo–acoustic instability were based on a theory that considers the densities of states of longitudinal modes perpendicular to the film surfaces. The imbalance in radiation pressures exerted onto the film boundaries leads to a destabilizing pressure. While this theory should accurately predict the correct order of magnitude of the acoustic effect, a more accurate model should include transverse modes, non–perpendicular modes and the elastic coupling of the film with the surrounding media.

Other possible experimental approaches include the investigations of in-

stabilities of a free standing polymer film. The disintegration of a liquid polystyrene film may be prevented by capping it with two cross–linked polystyrene layers. Because of the conceptional simplicity of the experimental system, any deviation from a model based on the predictions of a van der Waals driven instability would be a clear indication for other destabilizing effects. Due to the different scaling behavior of acoustic and retarded van der Waals pressures with distance, by increasing the thickness of the film, the retarded van der Waals pressure decreases more rapidly with the film thickness than the acoustic pressure. For films thicker than 100 nm, the acoustic pressure dominates over the much weaker van der Waals pressure leading to a reentrant instability. Analyzing this instability would be a further demonstration of the presence of the thermo–acoustic pressure. The high viscosity of polymer melts leads, however to very long times that are needed for the instability to develop. One solution to this problem would be the use of very low molecular liquids such as PDMS together with a careful chosen substrate–film–environment combination.

Regarding the surface tension induced instability, it would be instructive to build a theoretical model that attempts to explain our experimental results. Using the Navier–Stokes equation to describe the hydrodynamics of the unstable liquid film coupled with a diffusion–type of equation, it should be possible to develop a theoretical model that describes composition–gradient driven instabilities. Numerically solving the system of the two coupled differential equations, should yield the most amplified wavelength.

In conclusion, we have analyzed several mechanisms that destabilize thin polymer films. These new ideas bring us a step closer in understanding the multitude of effects that affect the stability of polymer coatings. We have developed new methods to obtain porous materials with enhanced optical properties and patterned surfaces with 100 nm sized structures. However, all the bits and pieces that we know today have yet to come together to complete the great puzzle of film instabilities. Once we understand the main picture, the science of thin polymer films will start revealing its true beauty.

Chapter 9

Samenvatting

Dit proefschrift draait om het patroon formatie proces in polymere films. We waren geïnteresseerd in zowel toegepaste als fundamentele aspecten van de vorming van een structuur op micrometer en nanometer schaal. De kennis van de oorsprong van structuurvorming heeft ons in staat gesteld om de instabiliteiten van dunne films te gebruiken voor mogelijke toepassingen, bijvoorbeeld nieuwe lithografische technieken, die van aanzienlijke technologische interesse kunnen zijn. De snelle ontwikkelingen in de halfgeleiderindustrie eist een continue verkleining van de onderdelen op microchips.

In onze experimentele aanpak hebben we gebruik gemaakt van elektrische krachten in een plaatcondensator geometrie om dunne vloeibare lagen te destabiliseren. De druk, afkomstig van een sterk elektrisch veld op het film oppervlak, overwint de oppervlaktespanning dat een instabiliteit induceerd welke resulteerd in de formatie van kolommen tussen de twee elektrodes. De patroonformatie vond plaats bij verhoogde temperaturen, en werd bevroren door het monster snel af te koelen tot kamertemperatuur. Wanneer een lateraal gevariëerd elektrisch veld werd gebruikt, focuseerde de instabiliteit in de regionen met het hoogste elektrische veld. Dit proces resulteerde in de replicatie van een topografisch gestructureerde elektrode. Door een dubbellaag van

twee verschillende polymeren (polystyreen en polymethylmethacrylaat) te gebruiken, vormden electrodynamische instabiliteiten op beide polymeeroppervlakten een hiërarchische laterale structuur. De gevormde structuren vertoonden twee onafhankelijke karakteristieke dimensies: de eerste veroorzaakt door de gestructureerde elektrode, de tweede door de instabiliteit op de onderste polymeerlaag. Deze nieuwe aanpak stelde ons in staat om structuren te produceren op een sub–100 nm schaal. De twee materialen werden gestructureerd in een éénstaps procedure, in plaats van meerdere stappen zoals gebruikelijk bij andere lithografische technieken. Onze aanpak kan worden uitgebreid tot laterale hierarchische structuren bestaande uit een groot aantal verschillende materialen, en meer dan twee onafhankelijke laterale lengteschalen.

Op een fundamenteel niveau, laat het patroon formatie proces in dunne polymere films, de krachtbalans aan het filmoppervlak zien. Door de filminstabiliteiten te observeren en te analyseren, waren we in staat om de krachten te bestuderen die over een zeer korte (nanometer) afstand werkten. Ons experimentele werk liet een nieuw fundamenteel effect zien, afkomstig van de beperking van de thermische fluctuaties binnen een dunne polymere film. We hebben laten zien dat krachten, die afkomstig zijn van thermisch opgewekte akoestische fluctuaties in dunne lagen, vergelijkbaar zijn met van der Waals krachten. Een elegante methode om de korte afstands krachten te meten die afkomstig zijn van een veld begrenzing, is het bestuderen van de instabiliteiten die zich ontwikkelen in een polymere film op een substraat. Een belangrijk aspect van deze benadering is dat de patronen, welke gecreëerd zijn door capillaire instabiliteiten, karakteristiek zijn voor de drijvende kracht achter de instabiliteit. In de aanwezigheid van een destabiliserende kracht, veroorzaakt de wedstrijd met de stabiliserende oppervlaktespanning de versterking van een smalle band van capillaire golven. Het patroon van de instabiliteit is daarom een karakteristieke handtekening van de betrokken krachten.

Polymere mengsels anderzijds, zijn decennia lang gebruikt als redelijk goedkope materialen met de gewenste structurelen en functionele eigenschappen. We optimaliseerden het ontmengingsproces van polymere mengsels om composiet coatings te produceren die als ontspiegelende coating van hoge kwaliteit kunnen worden gebruikt.

Het werk gepresenteerd in dit proefschrift levert een bijdrage zowel een experimentele als theoretische bijdrage aan bovengenoemde onderwerpen. Het variëerde van het gebruik maken van nanofase-gescheiden polymeerfilms als

ontspiegelende coatings van hoge kwaliteit tot de invloed van elektrische velden, temperatuur gradiënten en oppervlaktespannings gradiënten op dunne polymere films.

Het inleidende hoofdstuk plaatst het proefschrift in de actuele wetenschappelijke context, en stimuleert de noodzaak van onderzoek in de gepresenteerde velden.

Hoofdstuk 2 maakt de lezer vertrouwd met wat achtergrondinformatie over polymeerfysica. Dit fundamentele hoofdstuk helpt de experimentele resultaten beter te begrijpen alsmede de theoretische modellen in de volgende hoofdstukken. Het recenseerd de thermodynamica van faseschеiding in polymere mengsels, en verklaard de invloed van verscheidene externe factoren op de stabiliteit van dunne polymere lagen. In **hoofdstuk 3** worden de experimentele details van de monsterbereiding, samen met de fysische eigenschappen van sommige materialen uit de experimenten, gepresenteerd. Dit hoofdstuk legt ook het principe van sommige analyse instrumenten, die gebruikt zijn voor de karakterisatie van de monsters, uit. De meest gebruikte AFM methoden worden behandeld, zoals contact mode en tapping mode. Met behulp van de AFM was het mogelijk om de monsters met een hoge laterale resolutie te visualiseren. Door gebruik te maken van de tapping mode, kon de schade tijdens het scannen van zachte monsters tot het minimum worden beperkt. Een andere karakterisatie methode van dunne polymere films is ellipsometrie. Ellipsometrie is een zeer gevoelige meettechniek, welke gebruik maakt van gepolariseerd licht om dunne lagen, oppervlakten, en microstructuren van materialen te karakteriseren. Deze contactloze techniek helpt ons om de filmdikte te meten tot 1 nm, als mede de brekingsindex van de materialen die gebruikt zijn in het experimentele onderzoek.

Hoofdstuk 4 presenteert een nieuwe methode om onstpiegelende coatings (AntiReflection coating, AR) te produceren, welke gebaseerd is op nanoporeuze inorganische dunnen lagen. Een poreuze coating is een film met een zeer lage brekingsindex n. Wanneer de grootte van de poriën veel kleiner is dan de zichtbare golflengte, wordt de effectieve brekingsindex van het nanoporeuze medium bepaald door de gemiddelde brekingsindexen van het polymeer en het materiaal in de poriën (lucht). Daarom konden waarden van slechts 1,2 voor n worden bereikt door het aanpassen van de filmporositeit. De techniek die wij gebruikt hebben om dergelijke poreuze materialen te produceren was gebaseerd op het ontmengen van een binair polymeermengsel tijdens spin-

coaten. Om daarvan een poreuze film te maken, werd één van de polymeren verwijderd door de film in een selectief oplosmiddel te plaatsen. Een dunne laag van een dergelijke poreuze polymeermatrix kan als breedband AR coating worden gebruikt. Om de mechanische stabiliteit te verhogen, werd de polymeermatrix vervangen door een gemineraliseerde matrix uit een sol-gel proces. We hebben aangetoond dat optische componenten die gecoat zijn met een poreuze minerale laag, uitstekende optische transmissie hebben ($T > 99\%$ gemiddeld van 400 tot 680 nm). In het bijzonder bij de referentie golflengte ($\lambda = 550$ nm) werd een transmissie groter dan 99,95% bereikt.

Hoofdstuk 5 introduceert een nieuw effect welke de stabiliteit van dunne lagen beïnvloed. In het geval van een fluctuërend elektromagnetisch spectrum, leidt diens ruimtelijke beperking tot krachten aan de grensvlakken, het zogenoemde "Casimir effect". Deze krachten zijn veroorzaakt door het uitsluiten van de lange golflengtes tussen de grensvlakken. Over het algemeen kan worden gezegd dat dit effect leidt tot de theory van de van der Waals krachten. Hetzelfde principe geldt ook voor andere types van fluctuërende velden (ruis). De experimenten tonen aan dat naast de van der Waals krachten (p_{vdW}) het vrije oppervlakte van een superdunne vloeibare polymeerfilm ook onderworpen is aan een druk die afkomstig is van thermisch geëxiteerde fononen (p_{ac}). Om het bestaan van p_{ac} aan te tonen heben we drie verschillende experimenten uitgevoerd.

In de eerste serie experimenten vonden we een variatie in de film destabilisatie afhankelijk van de temperatuur, in tegenstelling tot de van der Waals theorie.

In de tweede serie experimenten hebben we een systeem gekozen waarin p_{ac} en p_{vdW} drukken tegenovergestelde voortekens hadden. De experimenten vertoonden de aanwezigheid van capillaire instabiliteiten, ondanks dat de van der Waals krachten de film stabiliseerden. De enige mogelijkheid om rekening te houden met de opkomende instabiliteit was door het destabiliserende effect van p_{ac} mee te nemen.

Het derde experiment behandelde de variatie van de akoestische grensvoorwaarden. Eén voorwaarde voor de begrenzing van lange (thermische) golflengtes is de akoestische afscherming van de film tegen de omgeving, wat een groot genoeg verschil inhield van dichtheden en elastische eigenschappen van film en substraat. Door een geschikt substraat en geschikte films te kiezen, hebben we laten zien dat de akoestische druk aan en uit geschakeld kan worden. Als

gevolg daarvan konden we films destabiliseren die anders stabiel zijn.

Dankzij de kwalitatieve aard van deze drie aanvullende experimentele aanpakken konden wij krachten identificeren die afkomstig zijn uit thermische ruis. Onze experimenten bevestigen onze kwalitieve voorspellingen betreffende de temperatuursafhankelijkheid, grootte en relevante grensvoorwaarden, zoals ze voorspeld zijn voor het destabiliserend effect van de akoestische druk. We hebben de hoge gevoeligheid van de filminstabiliteiten aangetoond voor krachten die over kleine afstanden werkzaam zijn, en we hebben het bestaan van het akoestische Casimir effect aangetoond.

Een nieuwe lithografische methode welke gebruik maakte van de instabiliteiten uit hoofdstuk 5 is beschreven in **hoofdstuk 6**. Deze methode stelde ons in staat om structuren te reproduceren met een laterale grootte van slechts ongeveer 100 nm, door versterking en focusering van de capillaire instabiliteiten in een lateraal inhomogeen elektrisch veld. Onze lithografische aanpak leidde tot de vorming van hiërarchische patronen met primaire en secondaire onafhankelijke dimensies. De tweede instabiliteit leidde tot structuren met een significant kleinere breedte (met een factor 10) dan de primaire structuurgrootte. Tezamen met een topografisch gestructureerde elektrode werd deze strategie gebruikt om patronen te reproduceren van ongeveer 100 nm, veel kleiner dan de patroongrootte van de master.

Lithografie, welke gebruik maakt van elektrische velden, is robuust en veelzijdig, maar de externe interactie met het formatie proces van de structuur zou een beperking kunnen zijn. Dit nadeel kon worden omzeild door gebruik te maken van filminstabiliteiten die karakteristiek voor het systeem zijn.

Onze aanpak, zoals gepresenteerd in **hoofdstuk 7**, gebruikte een polymeerfilm die een macromoleculaire surfactant bevatte. Het modelsysteem was een binair mengsel van polystyreen en polyvinylmethylether. PVME had een veel lagere oppervlaktespanning dan PS, en vormt een verrijkte laag aan het oppervlak. Fluctuaties in de compositie aan het oppervlak leiden tot een variatie van de oppervlaktespanning. Het gevolg van deze laterale gradiënt in de oppervlaktespanning was een stroom van materiaal naar de regionen met de hoogste oppervlaktespanning (Marangoni stroom). Een groot voordeel van dit proces is dat de instabiliteit inherent is aan het systeem. Er is geen noodzaak voor een exterene ingreep, zoals het het geval is bij elektrodynamische lithografie. Dit voordeel bleekt nuttig te zijn wanneer getracht werd geleidende polymeren te structurenen, die zeer gevoelig zijn voor hoge elektrische

velden. Door de film met een topografisch gestructureerd oppervlak te begrenzen, hebben we gebruik gemaakt van de Marangoni instabiliteit om de film functioneel te maken. De instabiliteit of de ontvochtiging van PS/PVME films werd vastgehouden door de grensvlakken waardoor diens structuur gereproduceerd kon worden.

Ten slotte besluit **hoofdstuk 8** het werk van dit proefschrift. De toename aan kennis over oppervlakte interacties maakte het voor ons mogelijk om nieuwe technologiën te bedenken en te ontwikkelen. Er zijn echter een aantal aspecten van bulk en oppervlakte instabiliteiten die men moet leren te begrijpen. De controle over patronen van submicrometerschaal is niet alleen technologisch behoorlijk interessant, doordat het helpvol is bij het aanpassen van eigenschappen van functionele materialen, maar stelt ook een fundamentele uitdaging voor.

List of Symbols

a	capillary constant
c	speed of light ($3.00 \cdot 10^8$ m/s)
c_i	constants
e	phonon energy density
h	Planck's constant ($6.63 \cdot 10^{-34}$ Js)
i	index used for different media or directions
j	mass flux in a thin film
j_e	energy flux e.g. of phonons
e	phonon energy density
k	Boltzmann's constant ($1.38 \cdot 10^{-23}$ J/K)
h	film thickness
h_{abs}	phonon absorption length
$h_{\mathrm{SiO_x}}$	oxide layer thickness on a silicon waver
g	gravitational acceleration
n	integer, e.g. degree of polymerization
p	surface pressure
p_0	constant pressure independent of film thickness h (e.g. atmospheric)
p_{ac}	pressure due to acoustic fluctuations
p_{atm}	atmospheric pressure
p_{el}	pressure due to electrostatic interactions
p_{ex}	excess surface pressure
p_L	Laplace or capillary pressure
p_{sr}	pressure due to short-range interactions
p_{vdW}	van der Waals pressure
q	wave vector
s	arc length
u	sound velocity
x	lateral coordinate
z	perpendicular coordinate
A	nonretarded Hamaker constant
B	retarded Hamaker constant

M_w	molecular weight of a polymer
PD	polydispersity
T_g	glass transition temperature
Z	acoustic impedance
Φ	free energy of interaction
$\mathcal{A}$	surface area
$\mathcal{F}$	free energy
$\mathcal{R}$	radius of curvature
$\mathcal{V}$	volume
ϵ	dielectric constant
ϵ_0	dielectric vacuum permitivity ($8.85 \cdot 10^{-12}$ As/Vm)
η	viscosity
γ	surface tension (surface free energy)
λ	wavelength
λ_a	atomic length
λ_c	critical or cut-off wavelength
λ_m	maximally amplified wavelength
$\tilde{\lambda}$	dimensionless relative wavelength (λ/λ_c)
ν	frequency
ν_c	cut-off frequency
ν_D	Debye frequency
ρ	density
τ	time constant
τ_m	smallest time constant (maximal growth rate τ_m^{-1})
$\tilde{\tau}$	dimensionless relative time constant (τ/τ_m)
υ	velocity profile
ζ	fluctuating surface
Θ_D	Debye temperature
∂_i	partial derivative with respect to variable i
∇	gradient
Δ	Laplace operator
δ_{ik}	Kronecker symbol (Delta tensor)

List of Figures

List of Tables